Integrated Ultrasonic-Photonic Devices

Barretto, Elaine Cristina Saraiva

Publication date:
2011

Document Version
Publisher's PDF, also known as Version of record

Integrated Ultrasonic-Photonic Devices

A dissertation
submitted to the Department of Photonics Engineering
at the Technical University of Denmark
in partial fulfillment of the requirements
for the degree of
philosophiae doctor

Elaine Cristina Saraiva Barretto
June 10, 2011

Integrated Ultrasonic-Photonic Devices

This thesis is dedicated to my family in Brazil. None of this work would have been possible if it wouldn't have been for all the education and love they provided me. They paid the highest price to make this work possible: my absence. We all suffered together in every single day of this journey, but we learned a lot from each other, and became stronger. Thank you all for always supporting my crazy ideas and letting me follow my dreams.

Preface

This thesis presents research carried out from September 2007 to February 2010 in the Department of Photonics Engineering, at the Technical University of Denmark. This PhD study has been supervised by Prof. Jørn M. Hvam, Assoc. Prof. Kresten Yvind and Mike van der Poel.

I would like to start thanking them for all the support provided and for the patience in bearing with my brazilian temper. Mike, in special, for hiring me and giving me the chance to work in this interesting project, and for all the nice dinners that he offered us at his place. Jørn, not only for the physics lessons but also for the life lessons. Kresten for all the help with the experimental aspects of the work – help much needed, due to my lack of previous experience. I would also like to thank Prof. Jesper Mørk, leader of the Nanophotonics Theory and Signal Processing Group, which I belonged to and where I could share my achievements with my colleagues and also learn a lot from all of them. And Prof. Beata Kardynal, for the guidance and advices, and also for the friendship.

This research involved a lot of cleanroom processing and I want to thank all the people that helped me on getting through the experimental obstacles: Lars H. Frandsen, for teaching me the first (and probably most important) steps; Elizaveta Semenova, for growing the nice GaAs wafers; Luisa Ottaviano, for helping me out with many processes, especially the metal deposition and lift-off; Martin Schubert for sharing all his precious expertise in III-V processing; Peixiong Shi, from Danchip, for the amazing job with the e-beam lithography, for all the late hours spent on helping us and for the nice chinese tea I had the chance to sip when at his office; all the Danchip personnel for the training in the machines and help with the technical issues; Radu Malureanu for the help in many processes; Liu Liu for the help with the SOI processing; and finally

Roza Shirazi and Oleksii Kopylov for the help with the GaN processing.

I would also like to thank the people that helped me with the characterization setup: Weiqi Xue, for sharing the Network Analyzer; Minhao Pu, for lending fibers and samples, and for helping me with my doubts; Kamau Prince and Prof. Christophe Peucheret, for borrowing several equipments and helping me on setting them up; and all the people that eventually assisted me.

A special thanks to Alexander Huck and Stephan Smolka for reading some of my manuscripts and helping me to improve them, and to Henri Thyrrestrup Nielsen for the long and interesting discussions about physics.

The collaborations were also very important during the project. I would like to thank the people in the Department of Mechanical Engineering at DTU, especially Maria B. Dühring and Prof. Ole Sigmund, for the fruitful discussions related to the surface acoustic waves theory. Dr. Paulo Santos, from the Paul Drude Institute in Berlin, for providing the ZnO and IDTs deposition, for providing samples for measurement, and most of all for sharing his profound knowledge in the field of surface acoustic waves devices.

The help in the technical aspects of the project was very much appreciated, but if it wouldn't have been for the personal support, I wouldn't have reached the end of this journey. Denmark will always have a special place in my memories as the country where I made some of my most precious friendships. And they are so many, and so important... Vita, Alex, Liza, Stephan, Lena, Kamau, Henri, Roza, Denise, Henrique, Luisa, Kathrin, Radu, Minhao, Yuntian, Lirong, Brian, Michael,... You are so many that I can't fit all of you here, but be sure that you are all in my heart and became my family. Thanks for all the fun moments and for the support in the moments of despair. And for listening to my never-ending complaints. Last, but definitely not least, my best friend of all, my best part, the man of my life: Martin. Having met him already made everything worth it. Thanks for all the patience and love.

Abstract

This thesis deals with the modeling, design, fabrication and characterization of integrated ultrasonic-photonic devices, with particular focus on the use of standard semiconductor materials such as GaAs and silicon. The devices are based on the use of guided acoustic waves to modulate the light in channel waveguides and Mach-Zehnder interferometers.

Numerical models are developed based on the finite element method, and applied to several scenarios, such as optimization of the geometrical parameters of waveguides, use of slow light in photonic crystal waveguides and use of Lamb waves in membranized systems, all in search for paths to improve acousto-optic interaction. Some of the solutions proposed lead to enhancements of up to two orders of magnitude in the efficiency of the device.

The main aspects related to the design of the devices are discussed, including single-mode guidance, optical coupling to the fiber, bending losses, power splitting, phase delays and coupling between adjacent waveguides. The use of different numerical methods for the design of the different components are also discussed in terms of accuracy and speed.

The devices are fabricated and characterized. Three material platforms were investigated. Comparisons are made with the numerical and experimental results, and they validate the obtained response of the acoustic and photonic components of the device.

Finally, a new design for an optical frequency shifter is proposed, posing several advantages over existing devices in terms of size, integration and cost. The design proves to be robust towards fabrication and design tolerances. Several uses for this device are proposed, opening up a whole new group of applications for this class of integrated ultrasonic-photonic devices.

Resumé (in Danish)

Denne afhandling handler om modellering, design, fabrikation og karakterisering af integrerede ultralyds-fotoniske komponenter, med særlig vægt på brugen af standard halvledermaterialer som GaAs og silicium. Enhederne er baseret på anvendelsen af guidede akustiske bølger til at modulere lyset i enkelte fotoniske bølgeledere og i fotoniske bølgeledere arrangeret i Mach-Zehnder interferometre. Numeriske modeller er udviklet på baggrund af finite element metoden, og anvendes med henblik på forbedring af den akusto-optiske interaktion. De optimale geometriske parametre af flere forskellige typer optiske bølgeledere såsom ridge bølgeledere og fotonisk krystal bølgeledere med langsomt lys er undersøgt. Desuden er interaktionen mellem lys og akustiske Lambbølger i membraner undersøgt. Nogle af de foreslåede løsninger fører til forbedringer på op til to størrelsesordener i effektiviteten af enheden.

De væsentligste aspekter i forbindelse med udformningen af komponenterne diskuteres, herunder single-mode bølgeledning, optisk kobling til fiber, bøjningstab, opsplitning af den optiske intensitet fra en til flere bølgeledere, fase forsinkelser og kobling mellem nærtliggende bølgeledere. Brugen af forskellige numeriske metoder til design af de forskellige komponenter er også drøftet med henblik på nøjagtighed og hurtighed. Enhederne er fabrikeret og karakteriseret. Tre materielle platforme blev undersøgt. Sammenligninger er lavet mellem de numeriske modeller og de eksperimentelle resultater, og viser god overensstemmelse.Endelig er en ny konstruktion af en optisk frekvens skifter foreslået. Den foreslåede komponent udviser flere fordele i forhold til eksisterende komponenter med hensyn til størrelse, integration og pris. Det nye design er vist at være robust over for fabrikation og design tolerancer. En helt ny gruppe af applikationer for denne type af af integrerede ultralyds-fotoniske komponenter diskuteres og flere konkrete anvendelser foreslås.

Contents

Chapter 1

Introduction

1.1 Motivation

Ultrasonics is defined as the band of sound waves above 20 kHz, i.e., above human hearing. It continues up to the GHz range, where the hypersonic regime starts. Ultrasonic waves, or more specifically surface acoustic waves, have been extensively used in the electronic industry in the construction of many devices such as filters, oscillators and transformers. They are also used in sensors for many different areas, from chemical and pressure sensors to biological applications. Another actual strong application is on the fabrication of touchscreen displays.

Photonics is the science of manipulation of light, including generation, emission, transmission, modulation, signal processing, switching, amplification, detection and sensing. The tendency is to integrate as much of these functionalities as possible in the same photonic circuit, leading to more compact optical systems and with better performance.

Optics and acoustics have followed parallel paths of development from the beginning. Most phenomena that are observed in optics also occur in acoustics. As in electromagnetism, the same theory of acoustics applies for the whole frequency range, but what counts is the length scale, meaning that quite different technologies must be used to generate and detect acoustic waves in the various frequency ranges.

Only very recently, ultrasonic waves have been introduced in the world of

integrated photonics, leading to a range of new devices and to some new interesting physics [1, 2]. An appealing novel research area is the design of periodic structures that can control and localize both light and sound in the same spatial region at the same time [3, 4]. This could enhance the interaction between phonons and photons and can thus create non-conventional acousto-optical devices for the simultaneous control of electromagnetic and elastic waves.

1.2 Integrated Optics

Integrated optics is the technology of integrating various optical devices and components for the generation, focusing, splitting, combining, isolation, polarization, coupling, switching, modulation and detection of light, all on a single substrate (chip) [5]. Optical waveguides provide the connections between these components. An optical waveguide is a light conduit consisting of a slab, strip, or cylinder of dielectric material surrounded by another dielectric material of lower refractive index, such as the ones shown in Fig. 1.1. The planar waveguides, like the slab shown in Fig. 1.1, are useful in many integrated optic applications in spite of the fact that they provide optical confinement in only one dimension. However, the applications to be discussed in this work require optical confinement in two dimensions, and for that the so-called *channel waveguides* or 3D waveguides are used.

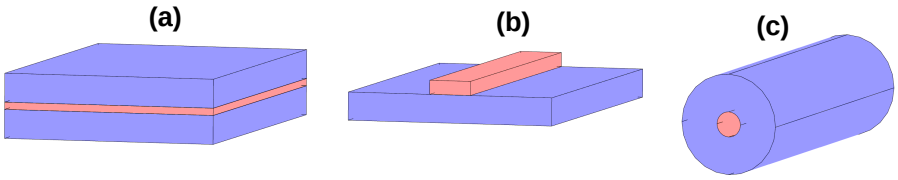

Figure 1.1: Optical waveguides: (a) slab, (b) strip, (c) fiber.

Useful geometries for channel waveguides include the ridge, the embedded-strip, the rib, and the strip-loaded waveguides illustrated in Fig. 1.2 [5]. The exact wave equation solution for these geometries hasn't been obtained yet, and therefore approximations are usually used on their calculations.

The waveguide may be fabricated in different configurations, as illustrated in Fig. 1.3. S-bends are used to offset the propagation axis. The Y-branch

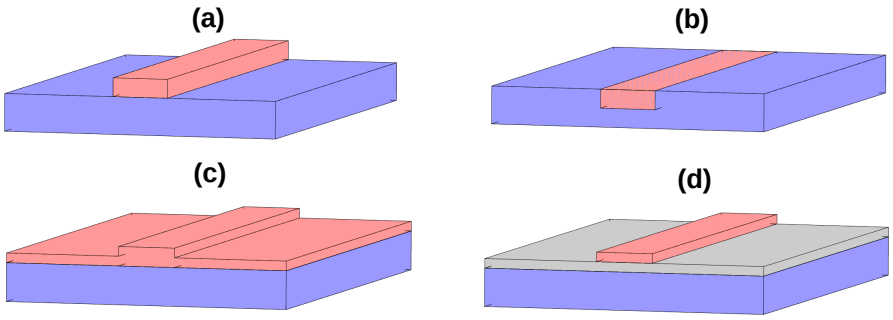

Figure 1.2: Geometry configurations of channel waveguides: (a) ridge, (b) embedded strip, (c) rib, (d) strip-loaded. The different colors represent different refractive indices.

plays the role of a beam splitter or combiner. Two Y-branches may be used to make a Mach-Zehnder interferometer.

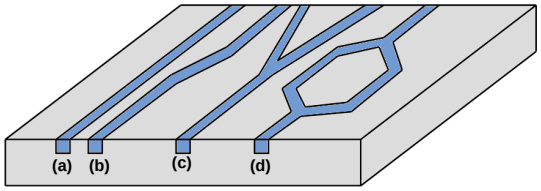

Figure 1.3: Some examples of different configurations for waveguides: (a) straight, (b) S-bend, (c) Y-branch, (d) Mach-Zehnder interferometer.

An advantage of rib waveguides is the relaxing of the stringent requirements for resolution and edge smoothness in the circuit fabrication process. Since only a portion of the energy impinges on the etched sides of the guide, it is anticipated that scattering losses will be lower than for ridge waveguides [6].

1.3 Acoustic waves and acousto-optic devices

The acousto-optic effect is the change in the index of refraction caused by the mechanical strain which is introduced by the passage of an acoustic-strain wave. The resulting index variation is periodic, with a wavelength equal to that of the

acoustic wave. Optical wave diffraction can be produced by interaction with either bulk acoustic waves (BAW) traveling in the volume of the medium, or with surface acoustic waves (SAW), traveling within roughly an acoustic wavelength of the surface. Since optical waveguides are typically only from a few hundred nanometers to a few micrometers thick, SAW devices are compatible with most optical integrated circuits applications.

In practical applications, acousto-optic (AO) devices have to compete with mechanical and electro-optic devices. The actual choice of the approach depends on the specific requirements for the application. In general, the parameters of performance to be considered are efficiency, speed, and resolution. AO devices usually cannot accomplish the ultrafast response that is feasible with electro-optic devices. This is evident because the acoustic wave velocities in solids are on the order of kilometers per second. AO devices, however, perform several functions that are difficult or impossible to accomplish in other devices.

Regardless of whether bulk or surface acoustic waves are used, two fundamentally different types of acousto-optic modulation are possible, and they are shown in Fig. 1.4 [7]. In the *Bragg-type* acousto-optic modulators, the optical beam is incident at a specific angle (the Bragg angle) with respect to the sound direction, and only one diffraction lobe is observed in the far-field pattern. In the *Raman-Nath* type of modulator, the optical beam is incident transversely to the acoustic beam. The interaction length of the optical path is relatively short, so that the optical waves undergo only a simple phase grating diffraction, thus producing a set of many interference peaks in the far field pattern.

1.3.1 Bulk acoustic waves

The bulk acousto-optic diffraction phenomenon has led to various optical devices, including deflectors, modulators, filters, etc [8].

The basic theory of acousto-optic interaction in isotropic media was well understood before the advent of the laser. It was laser development that stimulated extensive research on the device applications of acousto-optic interactions. Theory and techniques of acousto-optic devices were developed for the purpose of modulating and deflecting laser beams. By 1967 several important results on acousto-optic devices had been reported. These include the works of Gordon [9] on the efficiency and bandwidth of acousto-optic deflectors and modulators, by Korpel *et al.* [10] on acoustic beam steering, and by Dixon [11]

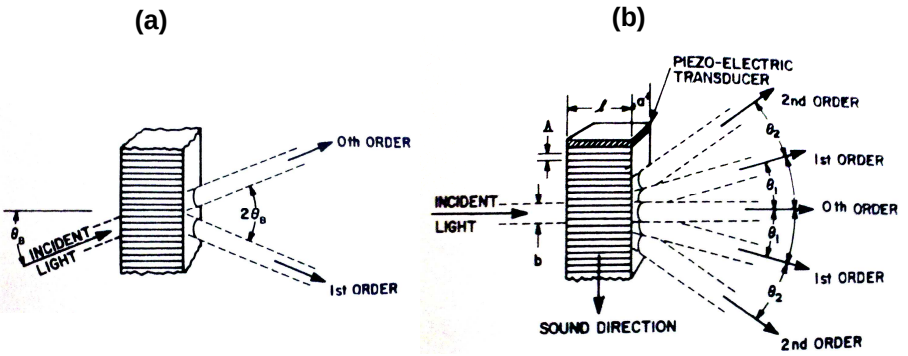

Figure 1.4: Basic structures of the two types of acousto-optic modulator [7]: (a) a Bragg-type, (b) a Raman-Nath type.

on acousto-optic interaction in anisotropic media.

1.3.2 Guided acoustic waves

The successful demonstration of the propagation of optical guided waves in thin dielectric films has led to the possibility of signal processing by means of miniaturized optical integrated circuits (IOC). These IOCs have been envisioned by many as playing a role similar to that played by electrical integrated circuits and have therefore generated much current interest in their development. Active electro-optic and acousto-optic components such as spectral and amplitude modulators, switches, and beam deflectors lie at the heart of any IOC that can be used for signal processing.

In 1885, J. Strutt (Lord Rayleigh) made the theoretical prediciton [12] that acoustic waves can propagate over a plane boundary between a semi-infinite solid and a vacuum or a sufficiently rarefied medium such as air, where the amplitude of the waves decays rapidly in the vertical direction. Since then, these waves have been found to exist in many circumstances and are now called *Rayleigh waves* or *surface acoustic waves*. SAW are of considerable technical importance, and their applications range from detection of surface crack in nondestructive tesing [13] to sophisticated optical signal processing [14].

Surface guided acoustic waves have many properties in common with optical guided waves, and this similarity between the two types of waves enables the

efficient use of both types of waves in IOC. In particular, both types of guided waves (in layered media) have most of their energy concentrated near the surface, i.e., in the waveguide vicinity. Both waves may be guided simultaneously using appropriate waveguide structures, and because of the layered nature of the waveguides of interest, both waves are dispersive with higher-order modes exhibiting cutoff behavior.

In 1970, Kuhn *et al.* [15, 16] have demonstrated, in two-dimensional waveguides, both Bragg deflection in the waveguide plane and mode conversion of optical guided waves by means of surface acoustic waves. These experiments clearly indicate the usefulness of the acousto-optic interaction in the construction of modulators, switches, and beam deflectors. This same group [17] has also demonstrated efficient excitation of optical guided waves using a periodic structure overlayed on the waveguide. Chang [18] has extended the periodic structure concept for waveguide coupling, by proposing the periodic structure required for coupling to be the periodic index change caused by a surface acoustic wave. This periodic index change scatters the optical energy into a specific direction that is determined by phase-matching constraints. By varying the acoustic wavelength or equivalently the periodicity of the index change, one can electrically scan the output, a capability not available in periodic structure output/input couplers of fixed periodicity.

Acousto-optic (AO) interactions in planar optical waveguides were studied extensively in the 1970s, and the resultant wideband Bragg cells have been used for realization of integrated optic modules such as RF spectrum analyzers, time-integrating correlators and light beam scanners. In contrast, AO interactions in channel optical waveguides only started to arouse interest in the 1980s [19], due to the fact that comparable cross sections of the channel waveguide and the optical fiber would greatly facilitate the interfacing of the resultant A0 channel devices with fiber optic systems.

The idea of using SAW on the modulation of waveguide-based Mach-Zehnder interferometers, first proposed by Gorecki *et al.* [20], ignited the research on the use of SAW in integrated optics leading to a new class of integrated photonic devices [21, 22], which will be explored in this work.

1.4 Objectives

The ability to change the refractive index of the light is a key feature in photonic circuits. Several methods have been used for this purpose, including the electro-optic, the thermo-optic and the acousto-optic effects.

Integrated ultrasonic-photonic devices are defined here as the use of guided ultrasonic waves (in surfaces or plates) interacting with confined light with the purpose of obtaining different photonic functionalities.

The objective of this work is to analyze several aspects related to the construction of ultrasonic-photonic devices, such as fabrication, modeling and design, seeking for ways to implement new functionalities, reduce dimensions and improve performance.

1.5 Outline of the thesis

This thesis is structured in six chapters. The first one is this brief introduction to the topic. In Chapter 2, the basic theory needed for the understanding of the physics involved in ultrasonic-photonic devices is introduced. First the acoustics part, with a brief description of the elasticity theory and of bulk and guided acoustic modes. Then interdigital transducers are introduced as means of exciting the ultrasonic waves, and the interaction between the optical and ultrasonic waves is described by means of the photoelastic effect. The semiconductor material platforms analyzed for the implementation of the devices are briefly discussed.

Chapter 3 is concerned with the modeling of the interaction between the strain fields induced by the ultrasonic waves and the optical waves. The numerical method used in the modeling is described, and applied in different configurations of acoustic and optic waveguides, with the purpose of optimizing the strain-optic overlap. Modeling of ultrasonic waves guided on the surface or in plates interacting with light guided in channel waveguides and photonic crystal waveguides is performed. The results bring insights on the best configurations to be used for increasing the performance of the devices.

In Chapter 4, the many aspects involved on the design of these devices are investigated. The design is the step related to the preparation of the lithographic mask used for the fabrication, and therefore the fabrication tolerances

also have to be taken into account. The influence of several parameters such as optical confinement, bending losses, power splitting, among others are discussed.

The fabrication processes applied for manufacturing ultrasonic-photonic devices are described in Chapter 5. Different material platforms were used, and the different results obtained are discussed. The samples were also characterized, for both the optical and acoustic excitations, and the characterization methods utilized and the results obtained are also presented.

Chapter 6 presents the case study of an application of all the concepts previously investigated, by exploring the design of an optical single-sideband modulator/ frequency shifter based on surface acoustic waves. Finally, in the last chapter the conclusions of the work are presented.

Chapter 2

Sound and Light

This chapter will introduce the theoretical fundamentals used to describe the physical processes of ultrasonic-photonic devices. First, the elasticity theory is presented, introducing the main principles of mechanics and elasticity. Then the solutions for bulk acoustic waves in isotropic solids are shown, serving as base for understanding the propagation of guided acoustic waves in plates. Two cases of guided waves are then analyzed: Rayleigh waves and Lamb waves. The excitation of acoustic waves by means of interdigital transducers is then discussed, completing the sections about sound waves. Next, the interaction between sound and light is introduced, considering the case where the propagation of the guided acoustic waves is perpendicular to the propagation of the guided optical waves. Finally, the material platforms to be used on the investigation of the acousto-optic interaction are briefly compared.

The coordinate system to be used in the equations and discussions throughout the work is the one shown in Fig.2.1.

2.1 Elasticity theory

The property of solid materials to deform under the application of an external force and to regain their original shape after the force is removed is referred to as its elasticity. Elasticity theory considers solids from a macroscopic point of view, and deals with them as an elastic continuum. The basic assumption is that a solid can be divided into small elements, each of which is considered

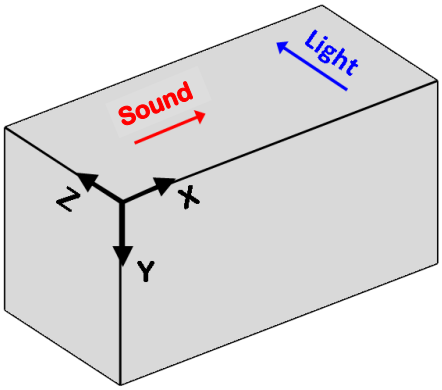

Figure 2.1: Coordinate system used in this work. The light propagates in the z direction, and the sound waves propagate in the x direction.

to be of macroscopic size. The smallest volume of material is defined as an *acoustic particle*, which is large compared with the spacing between atoms of the material. Within the volume of an acoustic particle, the magnitudes of macroscopic physical quantities are constants, i.e., independent of spatial coordinates. Moreover, small changes in the state of the solid with respect to a reference configuration are also assumed, so that the response of the solid is well within the elastic regime; in other words, the amount of deformation is proportional to the applied force, just as in a spring. The external force applied on a specified area is known as *stress*, while the amount of deformation is called the *strain*. The elasticity theory is well established and can be found in many standard books on acoustic wave theory, for example [23]. This chapter gives a brief overview of the basic concepts that will be used throughout the text.

The first element of elasticity theory to be defined is the *displacement vector*, which describes the vibrational motions of all acoustic particles within a medium, and is given by:

$$\mathbf{u} = u_x\,\hat{x} + u_y\,\hat{y} + u_z\,\hat{z}, \tag{2.1}$$

taking for now the displacement to be independent of time. The motion of a particle is expressed by the strain tensor S_{ij}, and the strain-displacement relation takes the form

$$S_{ij}(x,y,z) = \frac{1}{2}\left(\frac{\partial u_i}{\partial x_j} + \frac{\partial u_j}{\partial x_i}\right), \text{ with } i,j = x,y,z. \tag{2.2}$$

The quadratic terms are ignored, based on the assumption that the strains are sufficiently small, which will always be the case in linear ultrasonics. The internal forces are described by a stress tensor T_{ij}, which is related to the strain by means of the elastic stiffness tensor or elastic constant tensor, c_{ijkl}, according to the Hooke's Law:

$$T_{ij} = c_{ijkl}S_{kl}, \text{with } i,j,k,l = x,y,z. \tag{2.3}$$

If the stress and strain are functions of time as well as position, the motion is subject to Newton's laws in addition to the above equations, and these constraints can be combined in the form of an equation of motion [24],

$$\rho\frac{\partial^2 u_i}{\partial t^2} = \frac{\partial T_{ij}}{\partial x_j},\ i,j = 1,2,3, \tag{2.4}$$

where ρ is the density of the material.

2.1.1 Piezoelectricity

Piezoelectricity is a phenomenon which, in many materials, couples elastic stresses and strains to electric fields and displacements. It occurs only in anisotropic materials, whose internal structure lacks a center of symmetry. This includes many classes of crystals, but often the effect is weak. In a homogeneous piezoelectric insulator, the stress components T_{ij} at each point are related to both the electric field E and the strain components S_{ij}, by the relation:

$$T_{ij} = c^E_{ijkl}S_{kl} - e_{kij}E_k, \tag{2.5}$$

where the superscript on c^E_{ijkl} identifies this as the stiffness tensor for constant electric field and e_{kij} is the piezoelectric tensor, that relates elastic to electric fields.

2.1.2 Elastic isotropy conditions

This work concerns mainly with wave motion in anisotropic materials. But the complexity of the equations of elasticity for anisotropic materials is such that the properties of the waves can usually be found only by numerical techniques. The numerical technique used here is discussed in Chapter 3. In contrast, the solutions for isotropic materials are much easier to obtain, and since they have many features in common with the solutions for anisotropic materials, they will be described here for insight purposes.

The requirement that, in an isotropic solid, the physical constants must be independent of the choice of the reference coordinate system, imposes further constraints on the 21 constants of the stiffness tensor c_{ijkl}. It can be shown [25] that each stifnness constant can be represented by two parameters, the so-called Lamé coefficients λ and μ, where λ is called the first Lamé constant (and has no physical meaning) and μ is known as the modulus of rigidity. In this case:

$$c_{ijkl} = \lambda\delta_{ij}\delta_{kl} + \mu(\delta_{ik}\delta_{jl} + \delta_{il}\delta_{jk}), \tag{2.6}$$

where δ_{ij} is the Kronecker symbol. Thus, for an isotropic solid, the stiffness matrix is reduced to

$$[c] = \begin{pmatrix} \lambda+2\mu & \lambda & \lambda & 0 & 0 & 0 \\ \lambda & \lambda+2\mu & \lambda & 0 & 0 & 0 \\ \lambda & \lambda & \lambda+2\mu & 0 & 0 & 0 \\ 0 & 0 & 0 & \mu & 0 & 0 \\ 0 & 0 & 0 & 0 & \mu & 0 \\ 0 & 0 & 0 & 0 & 0 & \mu \end{pmatrix}. \tag{2.7}$$

Four elastic constants are routinely used to completely describe the elastic properties of an isotropic material. These are the Young's modulus $E_{_Y}$, the bulk modulus K, the Poisson's ratio σ and the rigidity (shear) modulus, which is identically equal to the Lamé's constant μ. These constants can be obtained by the Lamé constants:

$$E_{_Y} = \frac{\mu(3\lambda+2\mu)}{\lambda+\mu}, \tag{2.8}$$

$$\sigma = \frac{\lambda}{2(\lambda + \mu)}, \text{ and} \tag{2.9}$$

$$K = \lambda + \frac{2\mu}{3}. \tag{2.10}$$

In practice, many materials, due to methods of production, exhibit a certain amount of anisotropy, and various identities between constants must be used with care to avoid errors.

2.1.3 Anisotropic crystals

Most semiconductors are crystalline solids. Regarding commonly used elemental and compound semiconductors, the important crystal structures are diamond, zinc blende and wurtzite, and their unit cell structure is represented in Fig. 2.2. If a stress is applied to certain crystals, they develop an electric moment whose magnitude is proportional to the applied stress. This is known as direct piezoelectric effect.

A crystal with a center of symmetry cannot be piezoelectric. Thus, the diamond-type crystals (Si, Ge, etc.) cannot be piezoelectric. The III-V compounds crystallizing in the zinc-blende structure are the simplest crystals lacking a center of symmetry and, hence, capable of exhibiting piezoelectric and related effects. The zinc-blende crystal lattice is cubic with two atoms per unit cell, whereas the wurtzite lattice has a hexagonal structure with four atoms per unit cell [26].

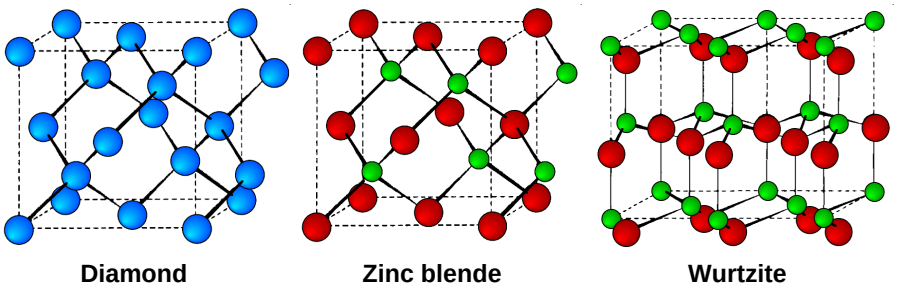

Figure 2.2: Unit cell structure of the diamond lattice, zinc blende lattice and wurtzite lattice.

The zinc-blende structure is based on the cubic spaced group $F\bar{4}3m$. The stiffness and the piezoelectric matrices of cubic crystals, such as zinc-blende, have the following symmetry characteristics:

$$[c]_{\text{cubic}} = \begin{pmatrix} c_{11} & c_{12} & c_{12} & 0 & 0 & 0 \\ c_{12} & c_{11} & c_{12} & 0 & 0 & 0 \\ c_{12} & c_{12} & c_{11} & 0 & 0 & 0 \\ 0 & 0 & 0 & c_{44} & 0 & 0 \\ 0 & 0 & 0 & 0 & c_{44} & 0 \\ 0 & 0 & 0 & 0 & 0 & c_{44}, \end{pmatrix}, \tag{2.11}$$

$$[e]_{\text{cubic}} = \begin{pmatrix} 0 & 0 & 0 & e_{14} & 0 & 0 \\ 0 & 0 & 0 & 0 & e_{14} & 0 \\ 0 & 0 & 0 & 0 & 0 & e_{14} \end{pmatrix}, \tag{2.12}$$

while the stiffness and piezoelectric matrices of hexagonal crystals, such as wurtzite, have the following symmetry characteristics:

$$[c]_{\text{hexagonal}} = \begin{pmatrix} c_{11} & c_{12} & c_{13} & 0 & 0 & 0 \\ c_{12} & c_{11} & c_{13} & 0 & 0 & 0 \\ c_{13} & c_{13} & c_{33} & 0 & 0 & 0 \\ 0 & 0 & 0 & c_{44} & 0 & 0 \\ 0 & 0 & 0 & 0 & c_{44} & 0 \\ 0 & 0 & 0 & 0 & 0 & c_{66} \end{pmatrix}, \tag{2.13}$$

$$[e]_{\text{hexagonal}} = \begin{pmatrix} 0 & 0 & 0 & 0 & e_{15} & 0 \\ 0 & 0 & 0 & e_{15} & 0 & 0 \\ e_{31} & e_{31} & e_{33} & 0 & 0 & e_{14} \end{pmatrix}. \tag{2.14}$$

2.1.4 Transformation properties

The stiffness and piezoelectric constants for crystalline materials are normally given with respect to crystal axes. This, however, may not always be the most convenient choice of axes for solving specific problems, and it is therefore necessary to relevant constants may be transformed into other coordinate systems

[23]. The stiffness matrix, the piezoelectric matrix and the dielectric constant matrix can be transformed respectively by the following equations:

$$[c'] = [M][c][M]^T, \tag{2.15}$$

$$[e'] = [M][e][M]^T \text{ and} \tag{2.16}$$

$$[\varepsilon'] = [M][\varepsilon][M]^T, \tag{2.17}$$

where $[c']$, $[e']$ and $[\varepsilon']$ represent the transformed matrices, and where $[M]$ is the 6x6 Bond transformation matrix [23]:

$$[M] = \begin{pmatrix} a_{11}^2 & a_{12}^2 & a_{13}^2 & 2a_{12}a_{13} & 2a_{13}a_{11} & 2a_{11}a_{12} \\ a_{21}^2 & a_{22}^2 & a_{23}^2 & 2a_{22}a_{23} & 2a_{23}a_{21} & 2a_{21}a_{22} \\ a_{31}^2 & a_{32}^2 & a_{33}^2 & 2a_{32}a_{33} & 2a_{33}a_{31} & 2a_{31}a_{32} \\ a_{21}a_{31} & a_{22}a_{32} & a_{23}a_{33} & a_{22}a_{33}+a_{23}a_{32} & a_{21}a_{33}+a_{23}a_{31} & a_{22}a_{31}+a_{21}a_{32} \\ a_{31}a_{11} & a_{32}a_{12} & a_{33}a_{13} & a_{12}a_{33}+a_{13}a_{32} & a_{13}a_{31}+a_{11}a_{33} & a_{11}a_{32}+a_{12}a_{31} \\ a_{11}a_{21} & a_{12}a_{22} & a_{13}a_{23} & a_{12}a_{23}+a_{13}a_{22} & a_{13}a_{21}+a_{11}a_{23} & a_{11}a_{22}+a_{12}a_{21} \end{pmatrix}. \tag{2.18}$$

The a_{ij} coefficients define a transformation matrix $[a]$, which is built according to the symmetry conditions of the crystal.

2.2 Bulk acoustic waves in isotropic materials

Generally, it may be said that acoustic waves propagate in the bulk of the material in either the longitudinal or transverse (shear) mode. In the *longitudinal mode*, the motion of the medium is only in the direction of propagation. In the *shear mode*, the motion of the medium is transverse (perpendicular) to the direction of acoustic wave propagation.

An acoustic wave propagating through an anisotropic material in an arbitrary direction (which does not coincide with axes or planes of symmetry of the material) is in a combination of longitudinal and shear modes. This type

of wave is called either *quasi-longitudinal* or *quasi-shear*, depending on which component is predominant. In anisotropic media there are so-called pure mode directions, which coincide with the axes of crystal symmetry. Along these axes, waves can propagate in either the pure shear or pure longitudinal mode or both. In most bulk acoustic devices using anisotropic material, pure mode directions are chosen for propagating directions to facilitate the wave excitation and to maximize the electrical-to-mechanical conversion efficiency [27]. Some general considerations of bulk waves are now considered.

First consider an infinite medium supporting acoustic plane waves, with frequency ω, in which the displacement $\mathbf{u}$ takes the form:

$$\mathbf{u} = \mathbf{u_0}\, e^{i(\omega t - \mathbf{k}\cdot\mathbf{x})}, \tag{2.19}$$

where $\mathbf{u_0}$ is a constant vector, independent of $\mathbf{x}$ and t.

Taking $\mathbf{u_0}$ to be perpendicular to $\mathbf{k}$ gives the shear or transverse waves, which wavevector is denoted by $\mathbf{k}_{_S}$, being

$$|\mathbf{k}_{_S}|^2 = \frac{\omega^2\,\rho}{\mu}, \tag{2.20}$$

with phase velocity $v_{_S}$ given by

$$v_{_S} = \sqrt{\frac{\mu}{\rho}}. \tag{2.21}$$

For the longitudinal waves, $\mathbf{u_0}$ is parallel to $\mathbf{k}$, with wavevector

$$|\mathbf{k}_{_L}|^2 = \frac{\omega^2\,\rho}{\lambda + 2\mu}, \tag{2.22}$$

and the velocity in this case is denoted by $v_{_L}$, and thus given by

$$v_{_L} = \sqrt{\frac{\lambda + 2\mu}{\rho}}. \tag{2.23}$$

Since λ and μ are always positive, the velocity of longitudinal waves is always larger than the velocity of shear waves:

$$\frac{v_{_L}}{v_{_S}} = \sqrt{\frac{\lambda + 2\mu}{\mu}} = \sqrt{\frac{1-\sigma}{0.5-\sigma}}. \tag{2.24}$$

In general, it is always possible to decompose the vector $\mathbf{u}$ defined in Eq. (2.1) into a divergenceless vector $\mathbf{u}_S$ and an irrotational vector $\mathbf{u}_L$ [27]. Therefore, it follows that

$$\mathbf{u} = \mathbf{u}_S + \mathbf{u}_L, \tag{2.25}$$

with

$$\nabla \cdot \mathbf{u}_S = 0 \text{ or } \mathbf{u}_S = \nabla \times \boldsymbol{\psi}, \tag{2.26}$$

and

$$\nabla \times \mathbf{u}_L = 0 \text{ or } \mathbf{u}_L = \nabla \phi \tag{2.27}$$

where ψ and ϕ are termed the vector and scalar potentials. They can be written in terms of velocities, such as

$$\nabla^2 \phi - \frac{1}{v_L} \frac{\partial^2 \phi}{\partial t^2} = 0, \text{ and} \tag{2.28}$$

$$\nabla^2 \boldsymbol{\psi} - \frac{1}{v_S} \frac{\partial^2 \boldsymbol{\psi}}{\partial t^2} = 0. \tag{2.29}$$

The use of potential functions, in addition to making it possible to separate variables, allows the solutions to be simply related to other quantities such as stress and velocity. Now Eq. (2.25) can be written as

$$\mathbf{u} = \nabla \phi + \nabla \times \boldsymbol{\psi}. \tag{2.30}$$

This format will be useful for the derivations in the next sections.

2.3 Acoustic waves in plates

As previously mentioned, guided acoustic waves have most of their energy concentrated near the surface, i.e., in the optical waveguide vicinity. This makes the guided acoustic waves good candidates for applications in optical integrated circuits. The acoustic waves of concern here will be the ones guided

in plates. Although bulk and guided waves are fundamentally different, they are actually governed by the same set of partial differential wave equations, being the difference in the boundary conditions to be satisfied, which make the problem difficult to be solved analytically. Some examples of guided wave problems that have been solved - and whose solutions have inherited the name of the investigators - are Rayleigh [28], Lamb [29], Love [30] and Stoneley [31] waves. Rayleigh waves are free waves on the surface of a semi-infinite solid, and are the most used in integrated devices. Lamb waves are waves of plane strain that occur in a free plate (membrane), and are widely used in flaw detection and delay lines. These are the two waves of concern in this work, and their characteristics will be described now in more detail.

2.3.1 Rayleigh waves

Rayleigh waves consist of combined longitudinal motion and shear motion, which are coupled by the boundary surface, as shown in Fig. 2.3 [27].

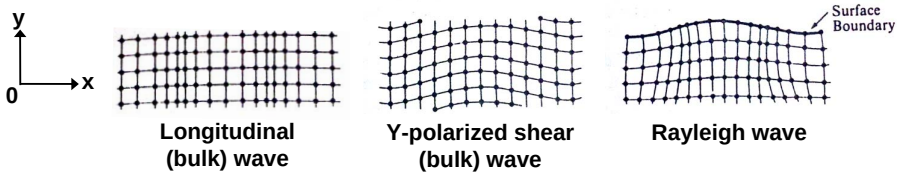

Figure 2.3: Comparison of longitudinal (bulk) wave, y-polarized shear (bulk) wave and Rayleigh wave, all propagating in the x direction. The polarization of the SAW wave is in the xy plane. From [27].

Rayleigh waves represent elastic perturbations propagating near the free boundary of a solid and decaying with increasing depth. The wave is non-dispersive, with a velocity v_R a little smaller than the shear wave velocity v_S. The motion of the material is in the sagittal plane xy, i.e., the plane containing the surface normal and the propagation direction. The motion of the individual acoustic particles is elliptical.

The existence of a Rayleigh wave will be derived here by means of the so-called direct method, according to Ristic's textbook [27]. Consider now an isotropic medium that extends infinitely in the x and z directions, with a boundary at $y = 0$, so that the medium occupies the space $y < 0$, and the space

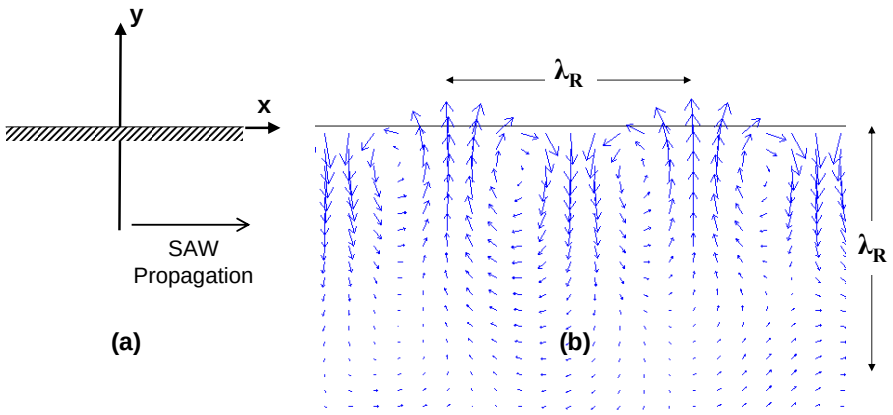

Figure 2.4: (a) Coordinate system used in the equations, (b) Instantaneous displacements for Rayleigh wave propagation. λ_R is the wavelength of the Rayleigh wave.

$y > 0$ is a vacuum, as shown in Fig. 2.4. The Rayleigh wave has no variation in the z direction, and therefore the field quantities will be independent of the z coordinate. The potentials defined by Eq. (2.26) and Eq. (2.27) are dependent on the x and y coordinates only, $\phi = \phi(x, y)e^{i\omega t}$, and the vector potential $\boldsymbol{\psi}$, which has only a z component, can be expressed as $\boldsymbol{\psi} = \hat{z}\ \psi = \hat{z}\ \psi(x, y)e^{i\omega t}$.

In that case, Eq. (2.28) and Eq. (2.29) can be written as

$$\frac{\partial^2\phi}{\partial x^2} + \frac{\partial^2\phi}{\partial y^2} + {k_{_L}}^2\phi = 0, \text{ and} \tag{2.31}$$

$$\frac{\partial^2\psi}{\partial x^2} + \frac{\partial^2\psi}{\partial y^2} + {k_{_S}}^2\psi = 0, \tag{2.32}$$

where $k_{_L}$ and $k_{_S}$ are wavenumbers of the longitudinal and transverse modes, respectively, given by

$$k_{_L} = \frac{\omega}{v_{_L}} \quad \text{and} \quad k_{_S} = \frac{\omega}{v_{_S}}. \tag{2.33}$$

The components of the displacement are obtained from Eq. (2.25) and are

given by

$$u_x = \frac{\partial \phi}{\partial x} + \frac{\partial \psi}{\partial y} \text{ and} \tag{2.34}$$

$$u_y = \frac{\partial \phi}{\partial y} + \frac{\partial \psi}{\partial x}. \tag{2.35}$$

Using the strain equation in Eq. (2.2), and the isotropy condition given by Eq. (2.7), Hooke's law can now be written in terms of the Lamé coefficients and scalar and vector potentials (this step is omitted here). The potentials are now assumed to vary as $e^{i\beta_R x}$ where β_R is the wavenumber of the Rayleigh wave. Denoting by

$$\gamma_L{}^2 = \beta_R{}^2 - k_L{}^2 \text{ and } \gamma_S{}^2 = \beta_R{}^2 - k_S{}^2 \tag{2.36}$$

and after applying the boundary condition of zero stress at the surface, the solutions obtained are

$$\phi = A_1 \, e^{i(\omega t - \beta_R x)} \, e^{\gamma_L y} \text{ and} \tag{2.37}$$

$$\phi = -iA_1 \, \frac{2\beta_R \gamma_L}{\beta_R{}^2 + \gamma_S{}^2} \, e^{i(\omega t - \beta_R x)} \, e^{\gamma_S y}. \tag{2.38}$$

for $y < 0$ under assumptions of $\gamma_L{}^2 > 0$ and $\gamma_S{}^2 > 0$, and where A_1 is an amplitude constant. It is seen that both potentials decay with depth; that is, the SAW energy is concentrated at the solid-air interface. The dispersion characteristic equation is obtained by combining the boundary condition $T_{yy} = 0$ with the Hooke's law and the vector potential equation:

$$(\beta_R{}^2 + \gamma_S{}^2)^2 - 4\beta^2 \gamma_L \gamma_S = 0. \tag{2.39}$$

Denoting the SAW velocity by $v_R = \omega/\beta_R$, it follows that the approximate real solution is given by [32]

$$\frac{v_R}{v_S} = \frac{0.87 + 1.12\sigma}{1 + \sigma}. \tag{2.40}$$

In the more general case of anisotropic substrate, the value of v_R is usually found by numerical techniques. A numerical method will be discussed in

Chapter 3. Sometimes on anisotropic materials, in addition to displacement components u_x and u_y, there may be a displacement component u_z perpendicular to the sagittal plane. These waves are termed generalized Rayleigh SAW waves. Also on anisotropic substrates the pure SAW modes are usually found in the planes of crystal symmetry. Many other types of surface waves can exist at the boundary between two materials or in a layered solid bonded to material of semi-infinite extent. For certain crystal cuts or at the interface between two materials, it may happen that ${\gamma_S}^2 < 0$, that is, the SAW velocity is larger that the shear wave velocity. Those are called *leaky waves*, because as they propagate they leak their energy continuously toward the interior of the solid. Some examples of leaky-SAW will be found throughout this work.

Finally, the displacements are found to be

$$u_x = -iA_1\beta\left[e^{\gamma_L y} - \frac{2\gamma_L\gamma_S}{\beta^2 + {\gamma_S}^2}\right]e^{i(\omega t - \beta_R x)} \tag{2.41}$$

and

$$u_y = A_1\gamma_L\left[e^{\gamma_L y} - \frac{2\beta^2}{\beta^2 + {\gamma_S}^2}\right]e^{i(\omega t - \beta_R x)}. \tag{2.42}$$

A plot of the displacements u_x and u_y of the Rayleigh mode in a plane across the depth of the material is shown in Fig. 2.5. The insets show the distribution of displacements for one acoustic wavelength.

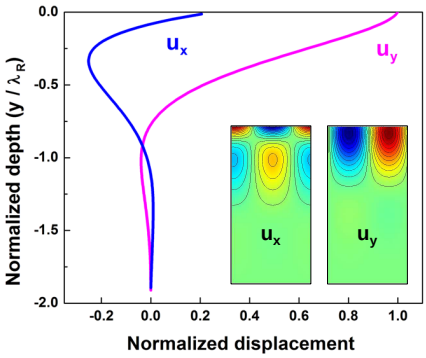

Figure 2.5: Horizontal and vertical displacement distributions of the Rayleigh mode.

2.3.2 Lamb waves

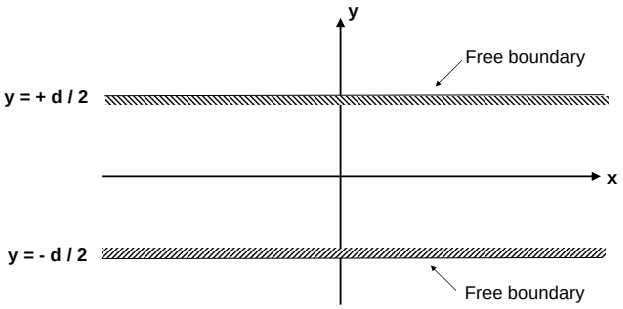

Figure 2.6: Coordinate system used in the equations for Lamb waves. The Lamb wave propagation is in the x direction.

Lamb waves refer to elastic perturbations propagating in a solid plate (or layer) with free boundaries, for which displacements occur both in the direction of the wave propagation and perpendicularly to the plane of the plate. In a plate with thickness d, such as the one shown in Fig. 2.6, there can exist a finite number of symmetrical and antisymmetrical Lamb waves, differing from one another by their phase and group velocities and distribution of the displacements and stresses throughout the thickness of the plate [32].

The phase velocity is the fundamental characteristic of a Lamb wave. Once it is known, the wavenumber, the stresses and displacements in any point of the plate can be determined. The equations used to determine the velocity at which a wave of a particular frequency (f d product) will propagate within the plate are called the Rayleigh-Lamb equations, and were first derived at the end of the nineteenth century.

The Rayleigh-Lamb frequency equations can be written as [33]:

$$\frac{\tan(qd)}{\tan(pd)} = -\frac{4k^2pq}{(q^2-k^2)^2} \text{ for symmetric modes.} \tag{2.43}$$

$$\frac{\tan(qd)}{\tan(pd)} = -\frac{(q^2-k^2)^2}{4k^2pq} \text{ for antisymmetric modes.} \tag{2.44}$$

Here, p and q are given by:

$$p^2 = \left(\frac{\omega}{v_S}\right)^2 - k^2 \tag{2.45}$$

$$q^2 = \left(\frac{\omega}{v_T}\right)^2 - k^2. \tag{2.46}$$

The wavenumber k is equal to ω/v_p, where v_p is the phase velocity of the Lamb wave mode and ω is the angular frequency.

From Eq. (2.43) and Eq. (2.44) it is possible to obtain the Lamb dispersion curves. But despite of looking quite simple, these equations can only be solved by numerical methods. A method to to obtain the eigensolutions for Eq. (2.43) and Eq. (2.44) will be described in Chapter 3. The distribution of the displacements of the first antisymmetric mode a_0 and the first symmetric mode s_0 are shown in Fig. 2.7. In the limit of $fd \to \infty$, the a_0 and s_0 modes become degenerate, and their displacements are tightly bound to the surface, corresponding then to independent Rayleigh waves on the upper and lower surfaces.

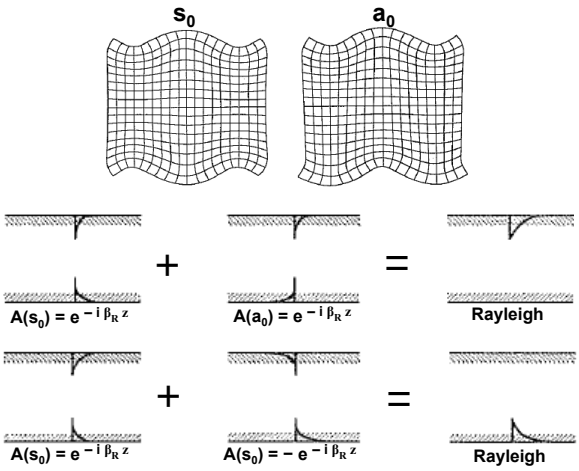

Figure 2.7: Top: displacement distribution of s_0 and a_0 Lamb modes. Bottom: Combination of a_0 and s_0 to form Rayleigh wave on upper and lower boundaries, in the limit $fd \to \infty$ (from [23]). A represents the amplitude of the fields.

That effect can also be clearly noticed by looking at the dispersion curve of the Lamb waves, which is plotted in Fig. 2.8. As the thickness of the plate increases, the velocity of the a_0 and s_0 modes converge towards the Rayleigh wave velocity.

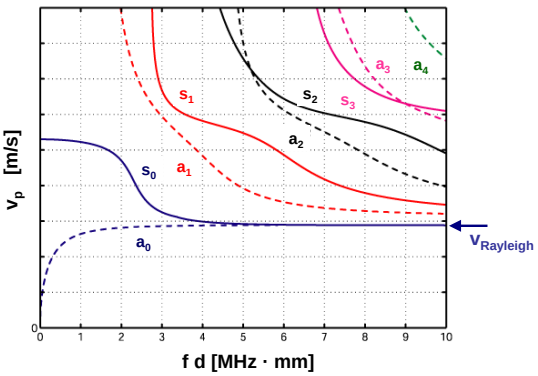

Figure 2.8: General shape of the dispersion curves for the Lamb modes.

2.4 Interdigital transducers

Interdigital transducers (IDTs) are widely used for the excitation and detection of SAWs [34]. They consist of metal strips deposited on a piezoelectric material, periodically spaced and connected by bus-bars, where the voltage is applied.

The configuration shown in Fig. 2.9 (a), which consists of two strips per period, is called single-electrode type, or single-finger. It is widely used due to its structural simplicity, which allows for easy fabrication, usually just by means of photolithography. But the spacing between the fingers is equivalent to a Bragg grating, which deteriorates the IDT characteristics for a large number of fingers. The other configuration shown in Fig. 2.9 (b), has four fingers per period and is called double-finger or split-finger. This configuration requires narrower finger widths, what makes the fabrication more challenging, but it allows for suppression of the Bragg reflection [35]. For this reason, this is the IDT configuration mostly used throughout this work.

With the purpose of concentrating stronger acoustic fields in smaller areas, one can also make use of the focused IDT configuration [1], as shown in Fig.

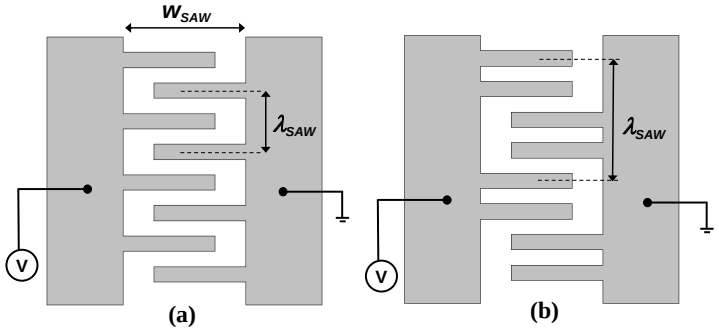

Figure 2.9: Schematic representation of the configurations of (a) single-finger and (b) split-finger IDTs.

2.10. Focused IDTs require a more delicate design, since the change in the angle of acoustic propagation generates reflections and coupling to the bulk acoustic waves, but they can nevertheless exhibit very good performance and are the strongest candidate for compact devices.

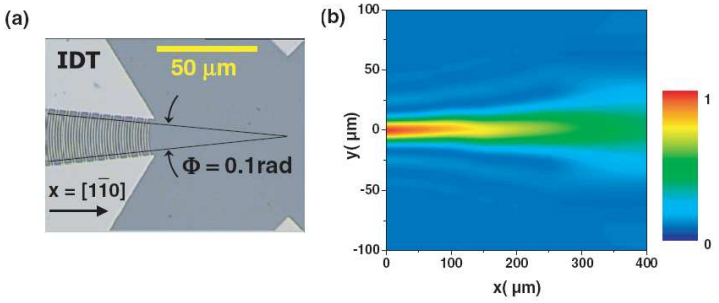

Figure 2.10: Focused IDT [1]: (a) microscope image, (b) Normalized acoustic power intensity delivered outside the transducer.

2.4.1 Transducer admittance

When a voltage V_t is applied to an isolated transducer, the transducer current is I, and the ratio I/V_t is the transducer admittance, Y_t. Usually, a major part of the admittance arises from the electrostatic charge density, which gives a

capacitive contribution to Y_t. This is usually written explicitly and denoted by C_t. The admittance is then written as [24]

$$Y_t(\omega) = G_a(\omega) + iB_a(\omega) + i\omega C_t. \tag{2.47}$$

The equivalent circuit thus has these three components in parallel, as shown in Fig. 2.11. Here $G_a(\omega)$ and $B_a(\omega)$ are the real and imaginary contributions due to the acoustic charge density. They are respectively the acoustic conductance and the acoustic susceptance. For an uniform transducer, the capacitance is approximately proportional to the number of periods of the transducer. The susceptance and the conductance are related to each other by causality [24].

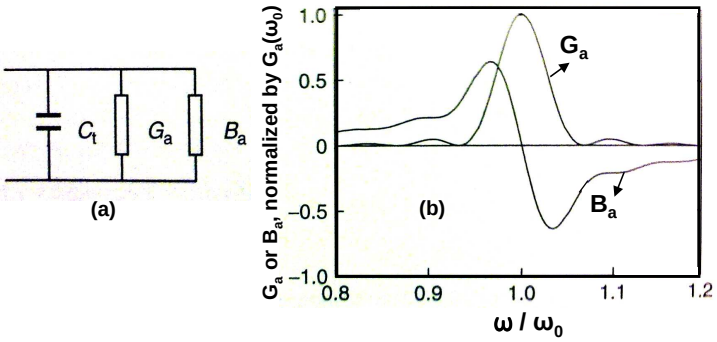

Figure 2.11: From [24]: (a) Equivalent circuit of a transducer, (b) Acoustic conductance and susceptance for uniform transducer.

The susceptance and the conductance are both frequency dependent, and are therefore directly related to the transducer frequency response. The susceptance will be used later in this work (in Chapter 5) as a numerical parameter for comparison with the experimental frequency responses obtained for the fabricated IDTs. It can be calculated by

$$B_a(\omega) = -\frac{\text{Imag}\{\text{Current on the surface of the electrode}(\omega)\}}{\text{Applied electric potential}}, \tag{2.48}$$

in units of Siemens.

2.4.2 Electromechanical coupling factor

Many of the acoustic wave properties of a material can be deduced by calculating the wave velocity, what is a complex calculation, for involving anisotropy and piezoelectricity. To obtain a faster estimation of the efficiency of a material on acoustic excitation, a parameter named *electromechanical coupling factor* is commonly used. First a metallized surface is defined, where the IDT fingers are deposited. The fingers are assumed to be an idealized metal coating which shorts out the parallel component of the electric field at the surface, but at the same time too thin to have any mechanical effect. The acoustic velocities for a free surface v_f, and for a metallized surface, v_m, will be different. The fractional difference between these velocities, $\Delta v/v$ characterizes the piezoelectric coupling to the wave. It is more common to define a coupling constant K^2, the so-called electromechanical coupling factor, as twice this value:

$$\frac{\Delta v}{v} = \frac{v_f - v_m}{v_f} \equiv \frac{K^2}{2}. \tag{2.49}$$

The electromechanical coupling factor is an indicator of the effectiveness with which a piezoelectric material converts electrical energy into mechanical energy, and therefore a high K is usually desirable for efficient energy conversion.

2.4.3 Thin films

SAW devices are also realized by using piezoelectric thin films such as ZnO and AlN. In layered structures, SAW properties significantly depend on the configuration used for the IDTs. The achievable electromechanical coupling factor in layered structures can be larger than that of individual materials under proper combination of materials and film thickness. The reason for this is that the structure can be designed in a way to concentrate the SAW fields on the piezoelectric film, and the IDTs can be placed appropriately for efficient SAW excitation. An example of this effect can be seen in Fig. 2.12 [36]. Four different configurations of IDTs are shown: (a) embedded transducer, (b) conventional configuration, and (c) and (d) are similar to the previous configurations with the addition of a counter-electrode. In the presence of the counter-electrode, the crossed electric field is dominant. For the other configurations, the in-line

field is dominant. The electromechanical factor is determined according to which direction of the electric field the piezoelectricity is most sensitive. Fig. 2.12 (e) shows the electromechanical coupling factor for a Rayleigh wave on a ZnO/Pyrex-glass structure, for different relations of ZnO thicknesses and SAW wavelength, for the four different configurations of IDTs. It can be noticed that the IDT configurations have a large influence on the electromechanical coupling factor behavior.

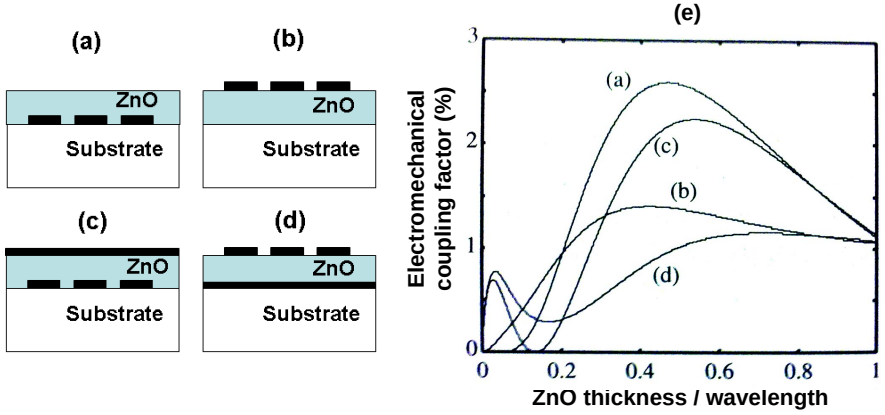

Figure 2.12: From [36]: (a)-(d) Different configurations of IDT and counter-electrode, (e) Electromechanical coupling factor for SAW on ZnO/Pyrex-glass structure for configurations (a)-(d).

The combination of thin films with high acoustic speed substrates, such as sapphire and diamond, can lead to the formation of vertical acoustic waveguides [1]. The near-surface region acts as a two-dimensional waveguide that prevents the leakage of the acoustic modes excited on the surface into the bulk. The acoustic field becomes more tightly confined to the surface in the waveguide configuration of Fig. 2.13, where the substrate is covered by a surface layer with lower acoustic velocity. In general, vertical confinement of the acoustic fields can be efficiently realized using layer structures with high contrast in elastic properties and thicknesses comparable to the acoustic wavelengths. The stronger vertical confinement induced by the slow overlayer not only increases the acoustic density near the surface, but also gives rise to additional surface acoustic wave modes bound to the surface, such as Sezawa modes [37].

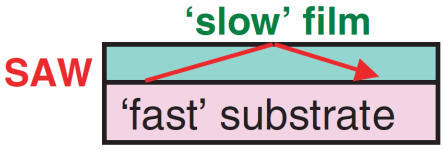

Figure 2.13: Illustration of a vertical acoustic waveguide, where the substrate has an acoustic velocity higher than of the thin film.

2.5 Ultrasonic modulation of guided light

The propagation of an ultrasonic wave in a solid produces a change in its crystal symmetry, which results in significant changes of its optical properties. The changes in the refractive index of the medium caused by the strain are described by means of the photoelastic effect [38],

$$\Delta\left[\frac{1}{n^2}\right] = p_{ijkl}S_{ij}, \tag{2.50}$$

where p_{ijkl}, called the photoelastic constant, is a fourth-order tensor. Using the stress-strain relation, the equation can also be written in terms of the stress components. For the specific case of media with cubic structure, the relation between the refractive index n and the stresses is given by [39]:

$$\begin{pmatrix} n_{xx} \\ n_{yy} \\ n_{zz} \\ n_{yz} \\ n_{xz} \\ n_{xy} \end{pmatrix} = \begin{pmatrix} n_0 \\ n_0 \\ n_0 \\ 0 \\ 0 \\ 0 \end{pmatrix} - \begin{pmatrix} C_1 & C_2 & C_2 & 0 & 0 & 0 \\ C_2 & C_1 & C_2 & 0 & 0 & 0 \\ C_2 & C_2 & C_1 & 0 & 0 & 0 \\ 0 & 0 & 0 & C_3 & 0 & 0 \\ 0 & 0 & 0 & 0 & C_3 & 0 \\ 0 & 0 & 0 & 0 & 0 & C_3 \end{pmatrix} \begin{pmatrix} T_{xx} \\ T_{yy} \\ T_{zz} \\ T_{yz} \\ T_{xz} \\ T_{xy} \end{pmatrix}, \tag{2.51}$$

where C_1, C_2 and C_3 are the stress-optical constants of the material, n_0 is the refractive index of the isotropic medium with no stress, and n_{ij} are the refractive index tensor components of the medium under stress, now anisotropic. The distribution of the stresses (strains) in the media, or in special in the region of the optical waveguide, is not uniform, and it is directly influenced by the material properties and by the geometry of the structure. Therefore the

geometry design is a determinant factor for the optical-strain overlap. A numerical method is usually required for the calculation of Eq. (2.51). Details on the method used here can be found in Chapter 3.

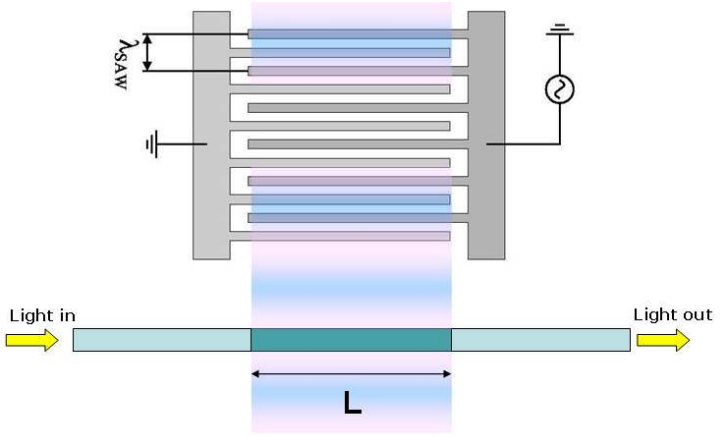

Figure 2.14: Configuration of SAW incident perpendicularly to an optical waveguide. The acoustic wavelength is not represented on scale, since it is assumed to be much larger than the width of the waveguide.

Considering perpendicular incidence of the ultrasonic wave onto the photonic waveguides, as shown in Fig. 2.14 and assuming the acoustic wavelength to be much larger than the waveguide dimensions, the acousto-optic diffraction is in the so-called Raman-Nath regime [15], previously illustrated in Fig. 1.4 (b). The analytical expression for this regime is:

$$\frac{I_m}{I_i} = J_m^2(\xi) \tag{2.52}$$

where I_m is the intensity of the light of diffraction order m, I_i the intensity of the incident light and J_m the m_{th} order Bessel function of the first kind of the Raman-Nath parameter ξ defined as:

$$\xi = k_0\, \omega_{SAW}\, \Delta n_{eff}, \tag{2.53}$$

where k_0 is the wavevector of the light, ω_{SAW} is the angular frequency of the

SAW and Δn_{eff} is the change in the effective index of the optical mode induced by the acousto-optical effect.

The light propagating through the acoustically-induced refractive index grating undergoes an instantaneous phase shift given by

$$\Delta\phi = \frac{2\pi\ \Delta n_{eff}\ L}{\lambda_0} \tag{2.54}$$

where λ_0 is the wavelength of light in free space, L is the interaction length between the acoustic and optical waves, represented in Fig. 2.14, and x is the propagation direction of the SAW.

2.6 Material platforms

Although there is a great number of lithographically processable materials that can be used to fabricate optical waveguides, only a few of them have shown the required characteristics to develop integrated optical devices. These include a wide range of glasses, crystals and semiconductors. In particular, the substrates most commonly used are glasses, lithium niobate, silicon-on-insulator, III-V semiconductor compounds and polymers. Each type of material has its own advantages and disadvantages, and the choice of a specific substrate depends on the particular application of the photonic device. Nowadays there exists a great variety of devices based on each of these materials.

Additionally, in order to build integrated ultrasonic-photonic devices, the material must also be suitable for acoustic excitation and propagation. An important parameter in the construction of a device based on acoustic waves is the substrate material. Some of the important properties of the material are the acoustic velocity, the piezoelectric coupling, temperature sensitivity, and the level of unwanted bulk-wave generation. Three material platforms were chosen to be investigated in this work, and a brief discussion on the advantages and disadvantages of each material in terms of integration follows.

2.6.1 AlGaAs / GaAs alloy

The alloy system AlGaAs/GaAs is very suitable for the fabrication of integrated devices, due to the perfect lattice match between $Al_xGa_{1-x}As$ and GaAs for all

values of x [40]. Another attractive feature of GaAs for integrated optics is that its alloys with other compounds of column III and V elements have refractive indices and bandgaps that vary with the amount of the other compound added. For example, the refractive index of $Al_xGa_{1-x}As$ at a wavelength of 0.9 μm decreases almost linearly with x, from 3.59 for x = 0 to 2 .97 for x = 1 [41]. GaAs total integration is possible, because the components for light generation and light detection can also be fabricated on GaAs. GaAs has been used to produce (near-infrared) laser diodes since 1962 [42].

GaAs forms crystals with the zinc-blende arrangement, and is therefore piezoelectric, making a suitable substrate for the fabrication of integrated ultrasonic-photonic devices. The maximum coupling of the transverse acoustic waves is along the [110] direction for the zinc-blende crystal, which is the reason why most of the experiments involving acoustic waves in GaAs are carried out with crystal cut in this direction [43].

2.6.2 ZnO / Silicon on Insulator

Silicon is the most used semiconductor in the photonics industry, mainly due to three reasons: (i) its low cost of production, for being abundant and cheap to process, (ii) its native insulator, silicon dioxide, is one of the best insulators available and simultaneously provides a very high refractive index contrast, (iii) its high mobility allows the fabrication of high-speed P-channel field effect transistors, which are required for CMOS logic.

The semiconductor laser is the key device for photonic applications. Bulk silicon is an indirect bandgap material and cannot be an efficient light emitter because the fast non-radiative recombination processes dominate the carrier transfer between the conduction and valence bands. Considerable effort has been devoted to developing efficient silicon-based light emitters, and many significant achievements have been obtained. Many studies have found that light emission from silicon is possible in low-dimensional Si structures - such as porous silicon [44], silicon nanocrystals, silicon/insulator superlattices [45], and silicon nanopillars - and in doped Si, with active impurities such as erbium [46]. Hybrid silicon lasers have also been developed [47, 48], which could potentially be produced in large scale, reducing the costs and making the silicon a platform compatible with the active substrates.

The main challenge on the acoustic aspect is the fact that silicon is not

piezoelectric, and therefore the excitation of the ultrasonic waves requires the deposition of a piezoelectric thin film, such as AlN or ZnO. ZnO has good piezoelectric properties and a high electro-mechanical coupling coefficient. It can be grown in thin film form by RF magnetron sputtering on a variety of substrates, including silicon, making it a promising material to be integrated with control electronic circuitry [49]. Other advantages of using ZnO films for SAW devices include high temperature stability and low cost of deposition. Modern microfabrication technology has allowed the production of SAW devices using ZnO films with high resonant frequencies [50]. ZnO thin films usually have a hexagonal wurtzite crystal structure.

2.6.3 (Al)GaN / Sapphire

GaN is probably the most important semiconductor material besides silicon. It has high piezoelectricity, a high sound velocity, a high heat capacity, and it is very hard and mechanically stable. It is widely used in the light-emitting diodes industry [51]. (Al)GaN layers grown on sapphire or semi-insulating SiC substrates have been widely investigated for high-power, high-frequency electronic devices due to their excellent electrical and thermal properties [52]. Recently, (Al)GaN-based SAW devices have been investigated for the purpose of exploiting both the piezoelectric properties and semiconductor characteristics of group-III nitrides [53, 54].

The most common orientation of sapphire used for GaN growth is the c-plane (0001). The crystal class of wurtzite GaN is $6mm$, which leads to isotropic elastic and piezoelectric properties in the c-plane, whereas the crystal class of sapphire $\bar{3}m$ has a sixfold symmetry of the elastic properties in the c-plane which results in no piezoelectricity. The (Al,Ga)N system has several advantages for SAW applications associated with the stronger piezoelectricity of the nitride compounds and wider variation of the elastic properties with composition [54]. In addition, the acoustic velocities are larger than in (Al,Ga)As layers, so that higher frequencies can be achieved for interdigital transducers fabricated with the same periodicity as in the (Al,Ga)As system [37].

Chapter 3

Modeling of modulated photonic waveguides

This chapter deals with the optimization of the performance of ultrasonic-photonic devices by means of improving the acousto-optic interaction. This is done by carefully modeling the system and finding optimal parameters that enhance this interaction. First, the numerical modeling concepts and characteristics are introduced, and subsequently applied to several scenarios. The waveguide geometry parameters are varied in search for simultaneous single-mode operation, low confinement losses, easier integration and higher acousto-optic modulation. The epitaxial structure of the materials is also investigated. Slow light in photonic crystal waveguides is discussed as a tool to enhance nonlinear phase change in the waveguides, and finally membranized systems are proposed as innovative means of increasing the modulation frequency and amplitude of the devices.

3.1 Finite element method modeling

The method chosen for modeling the systems presented here is the finite element method, by means of the software Comsol Multiphysics [55] together with Matlab [56] scripts. The objective is to approximate a partial differential equation (PDE) problem by discretizing it, i.e., dividing the geometry into small

parts called *mesh elements*. Triangular Lagrange elements of quadratic order are used, like the one shown in Fig. 3.1, what means that the function on each mesh element is a polynomial of second degree.

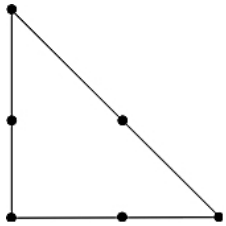

Figure 3.1: Representation of a triangular Lagrange element of quadratic order. For this kind of element, the node points are at the corners and side midpoints of all mesh triangles.

The configuration of interest consists of an acoustic wave propagating perpendicularly to the optical wave, as previously described in Chapter 2.

The material parameters used in the calculations are shown in Table 3.1. The mechanical and piezoelectric parameters for GaAs and AlGaAs were taken from [43]; the mechanical parameters for Sapphire are from [57], the ones for GaN from [37] and the ones for ZnO, Si and SiO_2 from [23]. The stress-optical constants were taken from [39].

3.2 Optical modes

The Comsol module used for modeling the optical modes is the RF Module. It is possible to simulate the in-plane modes and the perpendicular ones, depending on the geometry studied. For the case of simple channel waveguides, the propagation plane can be assumed to be infinite, and therefore the modes can be calculated as perpendicular to the calculation domain. By using the Hybrid modes formulation, all the components of the electric/magnetic field are solved, and therefore all the different polarizations supported by the waveguide can be obtained. Here, the formulation for the magnetic field **H** is used, and in this case the equation calculated for each node is

		GaAs	Al_xGaAs	ZnO	Si	SiO_2	GaN	Al_2O_3
Stiffness constants x 1^{10} [N/m^2]	c_{11}	11.88	11.88+0.14x	20.97	16.57	7.85	3.7	4.9749
	c_{12}	5.38	5.38+0.32x	12.11	6.39		1.45	1.6304
	c_{13}			10.51			1.1	1.1694
	c_{14}							0.2286
	c_{33}			21.09			3.9	5.0159
	c_{44}	5.94	5.94-0.05x	4.247	7.956	3.12	0.9	1.4751
	c_{66}						1.125	
Piezoelectric constants [C/m^2]	e_{14}	-0.16	-0.16-0.065x					
	e_{15}			-0.48			-0.3	
	e_{31}			-0.573			-0.36	
	e_{33}			1.32			1	
Stress-optical constants x 1^{-12} [1/Pa]	C_1	-18.39			-11.35	0.65		
	C_2	-10.63			3.65	4.50		
	C_3	-24.46				-3.85		
	Density [kg/m^3]	5360	5360-1600x	5606	2330	2634	6150	3986
	Refractive index (λ = 1.55 µm)	3.374	Dependent on x*	1.93	3.5	1.45	2.32	1.76

*Table 3.1: List of constants used in the modeling (*Equation can be found in [43]).*

$$\nabla \times (n^{-2}\nabla \times \mathbf{H}) - k_0^2 \mathbf{H} = 0, \tag{3.1}$$

where

$$\mathbf{H} = \mathbf{H}(x, y) \exp(\zeta z), \tag{3.2}$$

and $n^2 = \varepsilon_r$, the eigenvalue $\zeta = -i\beta - \delta_z$ with δ_z being the skin depth, and considering $\mu_r = 1$ and $\sigma = 0$.

In order to reduce the computational domain and calculate the losses, perfectly matched layer (PML) domains are used around the geometry of interest, as shown in Fig. 3.2. The PMLs are an additional domain with the purpose of absorbing incident radiation without producing reflections. The PML formulation can be deduced from Maxwell's equations by introducing a complex-valued coordinate transformation under the additional requirement that the wave impedance should remain unaffected [58].

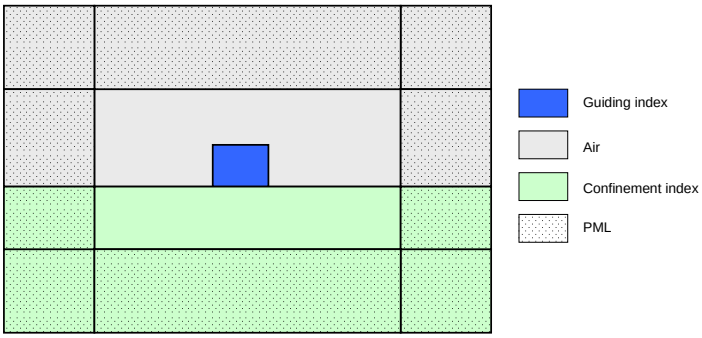

Figure 3.2: Geometry of the waveguide model, showing the perfectly matched layers.

Photonic waveguides are one of the fundamental components of integrated photonic circuits [59]. The waveguide in which light is confined in both the x and y directions is called 3D waveguide or *channel waveguide*. Most waveguide devices require 3D waveguides to control the guided modes efficiently because these waveguides can provide transverse light confinement within the guide surface (usually by means of lateral grooves) in addition to light confinement along the depth (by using an epitaxial layer with smaller refractive index than the

dielectric material of the waveguide). The modes supported by these waveguides cannot be calculated analytically, but the FEM method provides a very accurate approximation. The types of waveguides studied here will be the ridge and rib waveguides. There is some disagreement in the literature related to the nomenclature used for the waveguides, so the definition to be adopted here will be as follows. The difference between the ridge and rib waveguides is on the etching depth of the lateral grooves used for lateral index confinement, as can be seen in Fig. 3.3. In the case of the ridge waveguides, the sides are etched all the way down to the confinement (cladding) layer, while for the rib waveguides they are only partially etched [60]. This etching height makes a difference both for the distribution of the optical modes of the waveguides and for the propagation of the SAW across the waveguide, as it will be shown here. The geometrical parameters are defined as shown in Fig. 3.4. For the case of the ridge waveguide, $h = 0$. The calculations presented here are always performed for an optical wavelength of 1.55 μm, unless stated otherwise.

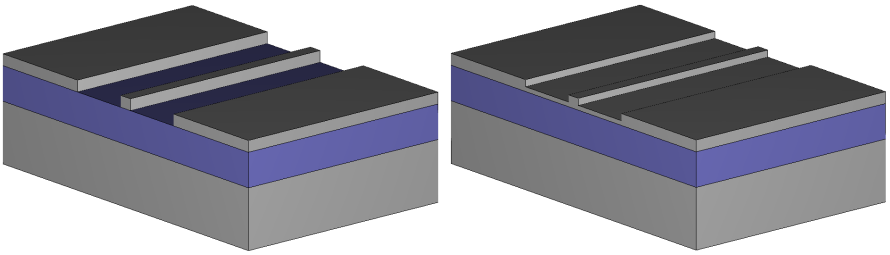

Figure 3.3: Artistic illustration of a ridge (left) and a rib (right) waveguide.

Depending on the material platform used, the refractive index contrast will vary, and therefore the mode confinement as well. To be able to quantify that, a *confinement factor* is commonly defined as the amount of optical power contained in the rectangular region $w \times H$ under the rib with respect to the total optical power associated to the propagating mode [7]. Fig. 3.5 shows three examples of modes guided in waveguides with different geometries and materials, where it is possible to compare the different confinement factors and observe the distribution of the modes. It is also important to investigate the propagation losses for different waveguide geometries. The propagation loss α can be calculated from the imaginary part of the propagation constant β by

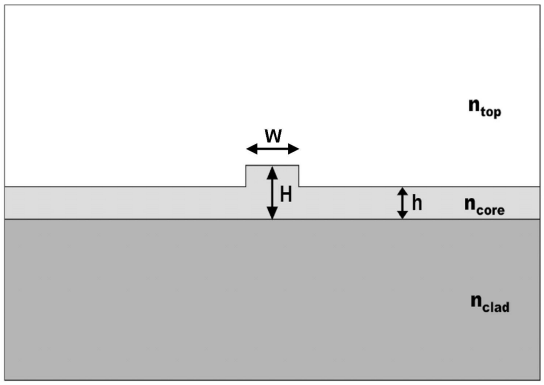

Figure 3.4: Geometrical parameters which are used in the analyses.

the relation:

$$\alpha = \mathrm{Im}\{\beta\} = \frac{2\pi}{\lambda_0}\mathrm{Im}\{n_{eff}\}, \tag{3.3}$$

where λ_0 is the wavelength of the light in free space and n_{eff} is the effective refractive index of the guided mode.

3.3 Acoustic modes

In order to model the acoustic waves and also to account for the piezoelectric effects, the structural mechanics and electrostatics equations need to be solved simultaneously. Here, the MEMS module in Comsol is applied. It is assumed that the acoustic propagation in the z direction is invariant, and therefore a plane strain approximation is used, meaning that the strain components S_{zz}, S_{yz} and S_{xz} are assumed to be zero. The dependent variables are the displacements in x and y directions and the electric potential V. Two kinds of analyses can be performed: eigenfrequency analysis and frequency response analysis.

3.3.1 Acoustic eigenfrequencies

In order to design interdigital transducers, i.e., to define the right width of the fingers for exciting a certain acoustic frequency, it is necessary to know the

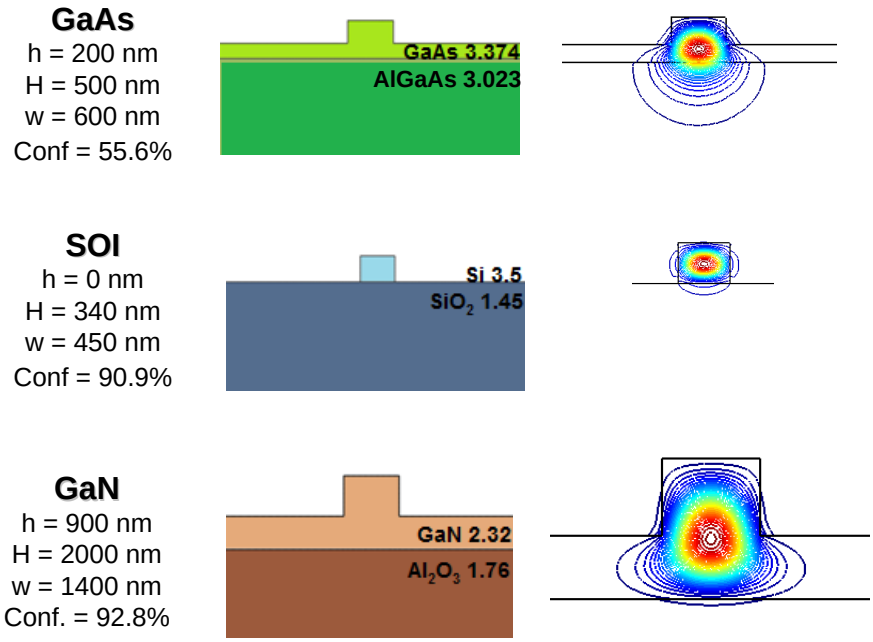

Figure 3.5: Geometry parameters, confinement factor and distribution of the fundamental TE mode in waveguides made of different materials.

velocity of the acoustic mode in the material. In the case of Rayleigh waves, since they are dispersionless, the acoustic velocity of the mode can be directly obtained by the eigenfrequency and the acoustic wavelength. IDTs usually have several hundreds of fingers, and each finger is usually much longer than its width. For that reason, edge effects can be neglected and a periodic unit cell can be defined. The geometry used for the calculation of double-finger IDTs is shown in Fig. 3.6. The voltage applied to the fingers in the models is ± 10 V unless stated otherwise. Periodic boundary conditions are applied to the boundaries Γ_1 and Γ_2, such that the values of u_x, u_y and V are the same in both boundaries. This implies that the calculated Rayleigh modes have wavelengths that are multiples of the width of the geometry. The depth of the material should be at least two times the acoustic mode wavelength, to assure that the displacements decay to zero at the bottom. The bottom boundary is fixed (zero mechanical displacement).

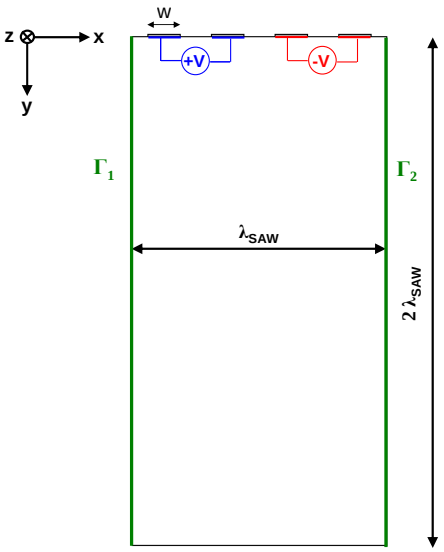

Figure 3.6: Geometry model for the simulation of a double-finger IDT. The alternated electric potential is applied as boundary condition on the fingers, Γ_1 and Γ_2 are periodic boundary conditions, and w is the width of the finger.

3.3.2 Acoustic wave propagation

In the previous case of the acoustic eigenfrequencies modeling, the periodic boundary conditions simulated an infinite system and therefore avoided reflections from the boundaries. In the case of real systems with well defined boundaries, it is necessary to use other methods for avoiding reflections. Here, PMLs are once more applied, this time to absorb the incident mechanical waves, by means of coordinate transformations [61]. The geometry is presented in Fig. 3.7 (a). To avoid having to include several fingers of the IDT in the model, it is possible to excite the acoustic wave in one of the boundaries by using an analytical equation. This allows one to easily control the acoustic power and frequency that will be excited in the model. The equations used for the displacements are [1, 62]

$$\mathbf{u}_{x_0} = \frac{A_{ph}}{k_{SAW}} 2\mathbb{C} \exp\left(ik_{SAW}x\right) \left[\exp\left(\Omega_R k_{SAW} y - i\varphi_R\right) + \exp\left(\Omega_R^* k_{SAW} y + i\varphi_R\right)\right], \tag{3.4}$$

and

$$\mathbf{u}_{y_0} = \frac{A_{ph}}{k_{SAW}} 2\mathbb{C} \exp\left(ik_{SAW}x\right) \left[\gamma_R \exp\left(\Omega_R k_{SAW} y - i\varphi_R\right) + \gamma_R^* \exp\left(\Omega_R^* k_{SAW} y + i\varphi_R\right)\right], \tag{3.5}$$

with

$$A_{ph} = \sqrt{\frac{k_{SAW} P_\ell}{2\rho v_{SAW}^3}}, \tag{3.6}$$

and where P_ℓ is the linear acoustic power density and $\mathbb{C}$ is a normalization constant. Ω_R, γ_R and φ_R are parameters of the material that can be determined by the solution of the following equations [63]:

$$0 = (c'_{11} - Xc_{11} - \Omega_R^2 c_{11})(c_{44} - Xc_{11} - \Omega_R^2 c_{44}) + \Omega_R^2 (c_{12} + c_{44})^2, \tag{3.7}$$

$$\gamma_R = \Omega_R \frac{c_{12} + c_{44}}{c_{44} - (X + \Omega_R^2)c_{11}}, \tag{3.8}$$

$$e^{-2i\gamma_R} = -\frac{\gamma_R^* - \Omega_R^*}{\gamma_R - \Omega_R}, \tag{3.9}$$

where $c'_{11} = \frac{1}{2}(c_{11} + c_{12} + 2c_{44})$ and $X = \rho v_R^2 / c_{11}$, with ρ as the density and c_{ij} as the elastic constants of the material. In order to solve Eq. (3.7) and Eq. (3.8), the velocity of the Rayleigh wave v_R must be known, and it can either be calculated by using the eigenfrequency model described in the previous section or by using analytic solutions of the SAW, which are available for certain geometries [63].

Figs. 3.7 (b) and (c) show the cross section plot of the displacements on the surface of the material. The absorption of the acoustic waves by the PMLs can also be observed.

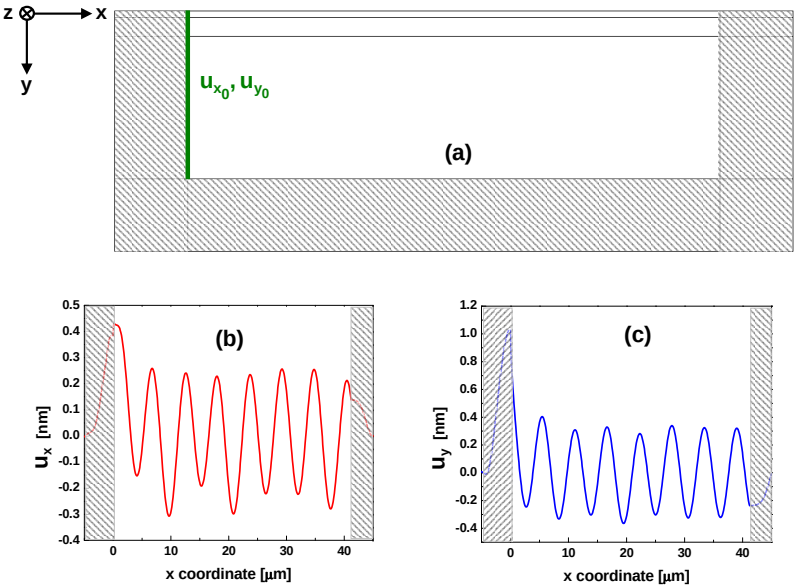

Figure 3.7: Simulation of the acoustic wave propagation for a GaAs/AlGaAs system: (a) geometry showing the boundary where the analytical equation for the SAW is applied and the PMLs (shaded area), (b) cross section plot of u_x on the surface of the material, (c) cross section plot of u_y on the surface of the material. The shaded areas in (b) and (c) represent the displacements inside the PML region.

3.4 Acousto-optic interaction

As described in Chapter 2, the strain induced by the acoustic wave changes the refractive index of the material along where it propagates. An optical mode guided in this medium will therefore experience changes on its effective index. In order to quantify the changes in n_{eff} caused by the strain, the optical mode must first be calculated in the absence of strain. Then the distribution of the strain is calculated for that geometry, and the optical mode is once more calculated, now in the media with refractive indices modified by the strain. Eq. (2.51) is used to couple the mechanical and optical models, and the geometry used in the calculations is shown in Fig. 3.8.

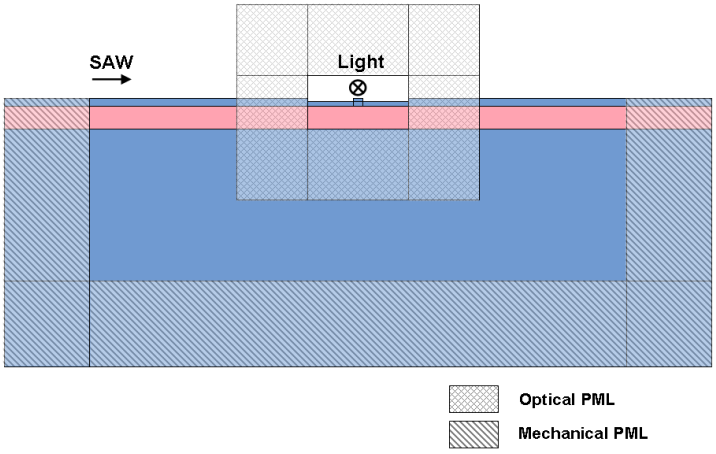

Figure 3.8: Geometry model of mechanical and optical systems coupled together.

3.5 Channel waveguides

Channel waveguides are the fundamental components of integrated photonic devices. Single-mode waveguides are more suitable for the construction of ultrasonic-photonic devices. In multi-mode waveguides, the acousto-optic interaction becomes more complicated due to the different propagation characteristics of each modal field. The geometry of the waveguide determines the

number of optical modes supported. A more detailed discussion can be found in Chapter 4. All the geometries used in the examples of this chapter lead to single mode behavior.

Two material platforms are investigated: GaAs/AlGaAs and Silicon-on-insulator. Silicon and GaAs are some of the most important semiconductors for discrete devices and integrated circuits [64]. The properties of these materials were briefly discussed in Chapter 2. GaAs has the advantage of being piezoelectric and having direct bandgap, what facilitates the on-chip integration. The GaAs wafers have more flexibility on the epitaxial growth than the SOI ones, but are also more expensive, and the refractive index contrast is much lower.

The geometrical parameters adopted in the next sections are the same that were previously defined in Fig. 3.4.

3.5.1 GaAs/AlGaAs waveguides

Rib waveguides are one of the most commonly used types of channel waveguide for GaAs/AlGaAs heterostructures [65]. In general, rib waveguides are less susceptible to optical scattering losses caused by surface roughness and non-vertical waveguide sidewalls. The reason is that the propagation loss of waveguides arises mainly due to light scattering from the etched sidewalls. Minimizing the optical field overlap with etched interfaces can effectively reduce the waveguide propagation loss, therefore decreasing the etching depth can realize this purpose [66].

The etching depth $(H - h)$ is a parameter that can have strong influence on the acoustic wave scattering, due to the discontinuities on the surface of propagation. To investigate this influence, the width w of the waveguides is fixed to 600 nm and the height H is fixed to 500 nm. The only parameter varied is h. This will allow the waveguide to be single-mode for the entire range of values of h - this validation can be found later in Chapter 4.

Let us first investigate the optical properties of the waveguides for different geometries. For very small values of h/H, the waveguide essentially behaves as a ridge waveguide, since the small heights of the rib layer do not support any optical modes for the 1.55 μm wavelength. For very large values of h/H, the waveguide essentially behaves as a slab waveguide, since the etching depth becomes so small that the lateral index confinement ceases. This behavior can

be observed in Fig. 3.9, where the effective indices of rib waveguides with different values of h/H are plotted, together with the effective indices of slab waveguides with different heights h. For $h/H < 0.37$ the slab doesn't support any modes. For $h/H \approx 0.948$ the values of n_{eff} of both the slab and rib waveguides become the same.

The geometry of the waveguide has a large influence on the confinement of the optical mode. To quantify this, the confinement factor and the propagation losses of different waveguide geometries are calculated and plotted in Fig. 3.10. For deeply-etched waveguides, which behave as ridge waveguides, the confinement losses are very high, due to the low vertical index confinement provided by the AlGaAs layer. For shallow-etched waveguides, which behave as slab waveguides, the poor lateral confinement leads again to high losses. The confinement effects can be visually observed in the insets in the right side of Fig. 3.10. The optimal geometry for lowest loss (higher confinement) is achieved for $h/H \approx 0.4$, which will be the geometry adopted here for fabrication of devices.

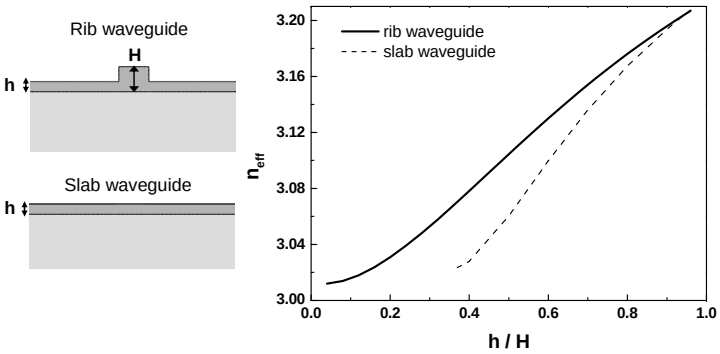

Figure 3.9: Effective indices of the TE fundamental modes of the rib waveguides with different h/H and of the slab waveguide with heights h.

To make efficient ultrasonic-photonic devices, it is necessary to obtain large modulation amplitudes. Therefore it is fundamental to know the relationship between the waveguide geometry and the changes in the effective index of the mode that can be obtained by acousto-optic modulation. Calculations of the change in the effective index of the fundamental TE mode were performed for different waveguide geometries, for an acoustic power density of 200 W/m, using the model described in Fig. 3.7. The results of these calculations are

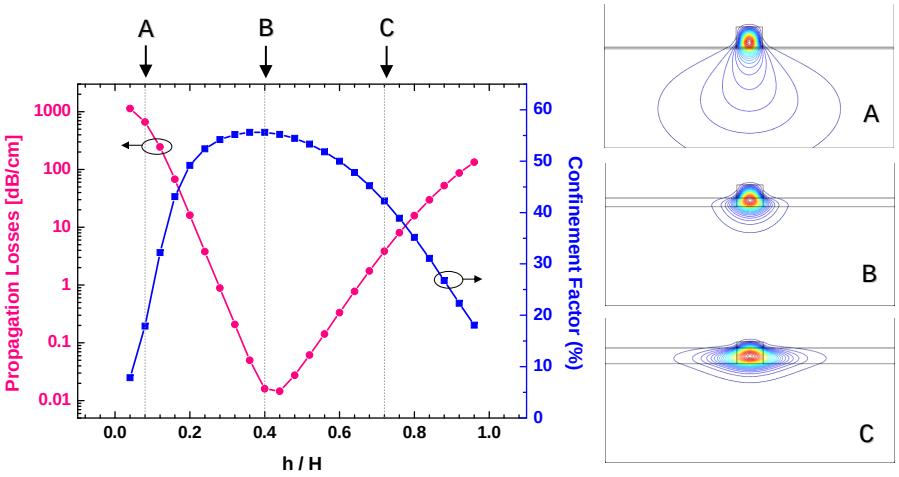

Figure 3.10: Propagation losses and confinement factor for GaAs/AlGaAs rib waveguides with different geometries. The right side shows the distribution of the TE optical mode for three different values of h/H.

presented in Fig. 3.11. It can be seen that the geometry of the waveguides has large influence on the modulation amplitudes that can be achieved by the same acoustic power density. First, it can be seen that Δn_{eff} is at least 3 times higher for the rib waveguides compared to ridge waveguides. This can be explained by the distribution of the stress in the waveguides, as shown in the right side of Fig. 3.11. In the case of the ridge waveguide, plotted in A, most of the stress is concentrated in the inferior corners of the waveguide, where there is a very small amount of light being guided, reducing the acousto-optic effect. The Δn_{eff} then increases for decreasing etching depths, reaching a maximum around $h/H = 0.7$.

The acousto-optic modulation is known to be proportional to the square root of the acoustic power density. The calculation of Δn_{eff} for different acoustic power densities, for the waveguide with geometry $h = 200$ nm, $H = 500$ nm and $w = 600$ nm is shown in Fig. 3.12. For this specific waveguide geometry and material, the relationship obtained is $\Delta n_{eff} \approx 6.45 \times 10^{-4} \sqrt{P_\ell}$. This number allows the previous results to be extrapolated for different acoustic powers [1].

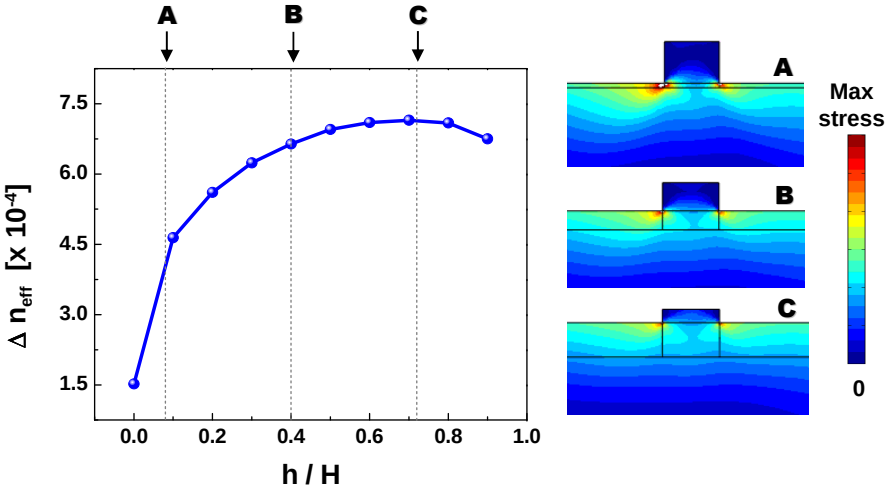

Figure 3.11: Changes in the effective refractive index of the fundamental TE mode of waveguides with different h/H relations, and plots of the distribution of the horizontal stress S_{xx} for three different values of h/H.

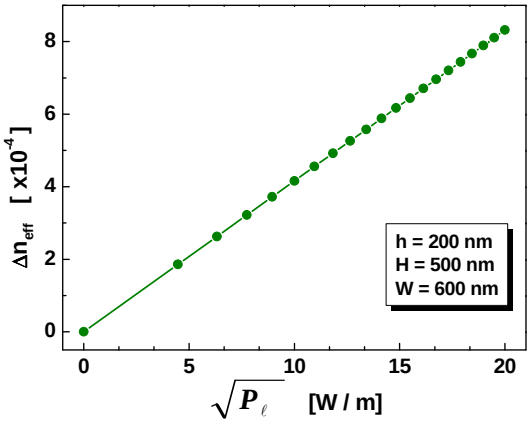

Figure 3.12: Changes in the effective refractive index of the fundamental TE mode of a GaAs/AlGaAs rib waveguide for different acoustic power densities. The dimensions of the waveguide are $h = 200$ nm, $H = 500$ nm and $w = 600$ nm. The linear dependence of the modulation amplitude with the square root of the acoustic power can be clearly observed.

3.5.2 Silicon-on-insulator waveguides

As mentioned before, silicon is not a piezoelectric material, and to be able to excite acoustic waves in a SOI device, one needs to deposit a piezoelectric thin film, such as ZnO.

There are several possible configurations, which are illustrated in Fig. 3.13. It is possible to have ZnO pads only in the region of the IDTs, where the acoustic wave is excited and then propagates from the pad to the silicon layer. Another alternative is to deposit ZnO all over the SOI wafer, covering also the waveguides. And the last option is to deposit a different material as planarization medium first, such as glass, and afterwards deposit the ZnO on top. All these configurations have advantages and disadvantages in terms of fabrication and performance. The influence on the performance of the devices will be examined by modeling these systems. Details on how to fabricate these different systems will be discussed later in Chapter 5.

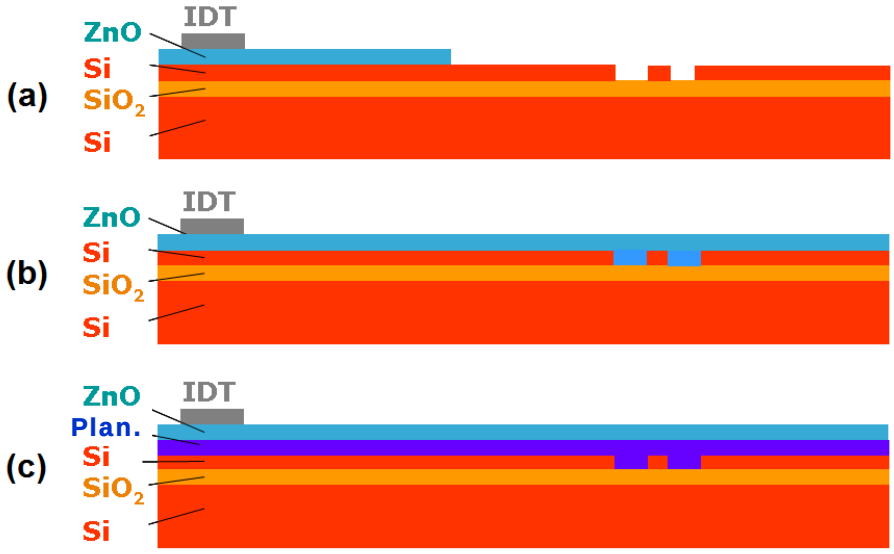

Figure 3.13: Different configurations of ZnO deposition on SOI wafer. (a) ZnO pads, (b) ZnO all over the wafer and (c) wafer planarization followed by ZnO deposition. The question mark in (c) represents the planarization material to be chosen.

The propagation of the SAW is severely affected by discontinuities on the surface. Thus, in terms of acoustic modulation, the planarization is expected to be a better choice of configuration. The thickness of the planarization layer is also expected to play an important role, both in the optical mode confinement and acousto-optic modulation. To quantify this effect, the confinement factor of the fundamental TE mode and the changes in effective index induced by the acoustic wave on this mode were calculated, for different thicknesses of planarization. SiO_2 was used as the material for the planarization layer. The results of these calculations are shown in Fig. 3.14. There is an optimum thickness of planarization layer of ~100 nm, for which the modulation is higher. For layers with thickness larger than this value, the modulation is reduced, due to larger distance between the waveguide and the higher piezoelectric field intensities. In the case of the non-planarized structure (ZnO pads configuration), the modulation is at least 5 times smaller, as plotted in the shaded area. The optical confinement factor is not much affected by the planarization with this material.

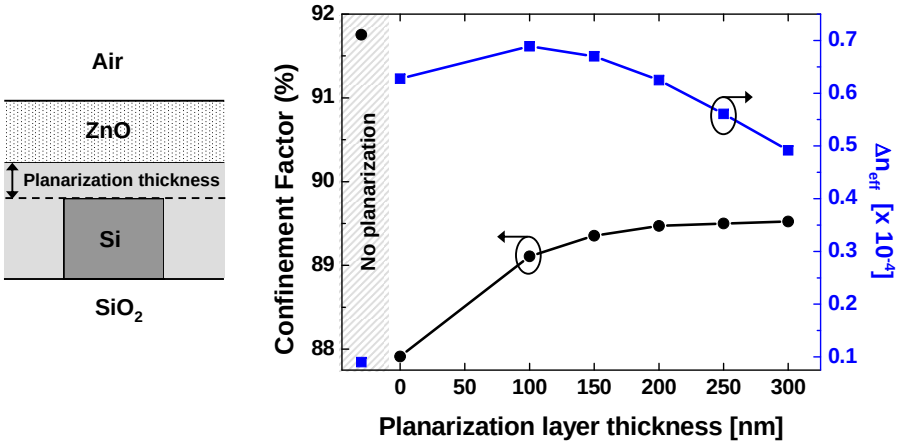

Figure 3.14: Confinement factor and changes in the effective index of the fundamental TE mode for SOI waveguides with different thicknesses of planarization. The shaded area in the graph shows the values for the structure with no planarization (ZnO pads).

In order to visualize the influence of the planarization layer in terms of the acoustic fields, Fig. 3.15 shows the distribution of the vertical displacement

(u_y) and the horizontal stress (T_{xx}) for two different configurations of ZnO deposition: with ZnO pads and with a planarized surface, where the glass layer used for the planarization covers only the trenches of the waveguide (planarization layer thickness = 0). In the case of the ZnO pads, the discontinuity of the pad has at least two effects on the acoustic wave propagation: increasing the acoustic losses (due to scattering to the bulk) and changing the acoustic wavelength (due to change in the epitaxial structure). These effects will of course influence the stress distribution in the region of the waveguides, as seen in the right side of Fig. Fig. 3.15. It can also be seen the planarized configuration introduces more stress in the region of the waveguide, due to the piezoelectric wave propagating above it, what explains the better performance compared to the non-planarized configuration.

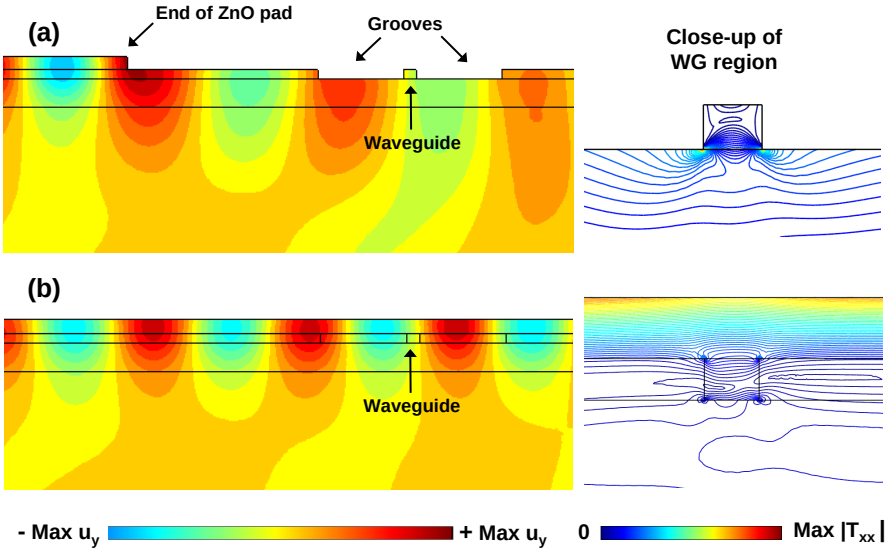

Figure 3.15: SAW propagation (vertical displacement distribution) and distribution of the horizontal stress in a SOI waveguide with (a) ZnO pads configuration and (b) planarized configuration.

It is also important to analyze how the confinement of the optical mode in the waveguide would be affected if a layer with a different refractive index would be used for the planarization. To estimate this effect, the confinement

factor for a SOI waveguide covered by materials with different refractive indices is calculated, and the results are presented in Fig. 3.16. If the material of choice is glass, which has a refractive index around 1.45, or ZnO, that has a refractive index around 1.93, the modes can still be fairly well confined. For values higher than that, the choice of material starts to play an important role on the optical confinement.

Certainly the mechanical properties of the material used for planarization also play an important role. The acousto-optic modulation would be expected to reduce with the use of materials that present strong acoustic dampening, such as polymers.

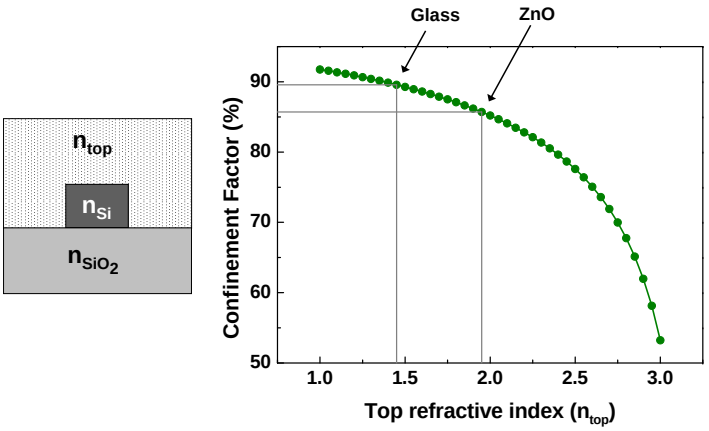

Figure 3.16: Confinement factor for a SOI waveguide covered by materials with different refractive indices.

3.6 Photonic Crystal waveguides

3.6.1 Introduction to photonic crystals

Photonic crystals (PhCs) are multidimensional periodic structures with a period of the order of the optical wavelength. The research field became active in the late 1970s and 1980s, triggered especially by the works of Yablonovitch [67] and John [68], with the development of the photonic band theory, an optical analogue of the electronic band theory, which can be used to compute

the dispersion characteristics of light in arbitrary PhC structures. The theory predicted the existence of a photonic bandgap (PBG), a frequency band of inhibited optical modes. Since the 1990s, PhCs with PBGs have been explored for various device applications. At present, PhC slabs, a high-index thin film with a two-dimensional array of air holes surrounded by air cladding, are widely used because of their intrinsic lossless optical confinement and simple fabrication process. Waveguides can be formed on the PhC slabs by introducing a defect in the array of air holes, such as reducing the size of the holes in one or several rows or removing complete rows of holes. The W1 PhC waveguide consists of a line defect created by removing one row of air holes in the PhC slab [69]. Light propagates through the defect, confined by total internal reflection in the vertical direction and by Bragg reflection, due to the PBG, in the lateral direction. Actually, different advantages are expected from such a guiding [70]: (i) the miniaturization of bends, (ii) the realization in a single technological step of a number of different functions, such as guiding, dispersion, filtering, as well as coupling and confinement functions. It has been known since 2001 that the strong dispersion in PhC waveguides generates slow light in the vicinity of the photonic band edge [71].

3.6.2 Slow light in PhC waveguides

The nature of the delay in a photonic crystal waveguide is easily understood by invoking the familiar ray picture commonly used to describe light propagation in a dielectric waveguide. Compared with total internal reflection alone, however, photonic crystals offer two additional features that can lead to the formation of slow modes - backscattering and omnidirectional reflection [72], as illustrated in Fig. 3.17 (a) and (b), respectively. Light is coherently backscattered at each unit cell of the crystal, so the crystal acts as a 1D grating, indicated by the vertical lines on the left-hand side of Fig. 3.17 (a). If the forward propagating and the backscattered light agree in phase and amplitude, a standing wave results, which can also be understood as a slow mode with zero group velocity. Away from the Brillouin zone boundary, one enters the slow light regime; the forward and backward travelling components begin to move out of phase but still interact, resulting in a slowly moving interference pattern: the slow mode. Further from the Brillouin zone boundary, the forward and backward travelling waves are too much out of phase to experience

much interaction and the mode behaves like a regular waveguide mode that is dominated by total internal reflection. The other unique feature offered by the PhC environment is that there is no cut-off angle; if a photonic bandgap is present, light propagating at any angle is reflected. Even light propagating at or near normal incidence may therefore form a mode, as indicated by the steep zigzag in Fig. 3.17 (b). Such modes have very small forward components, i.e. they travel as slow modes along the waveguide, or for k = 0, form a standing wave. These two effects also represent the two limiting cases for slow light propagation in photonic crystal waveguides; hence the bandwidth is ultimately limited by the size of the Brillouin zone.

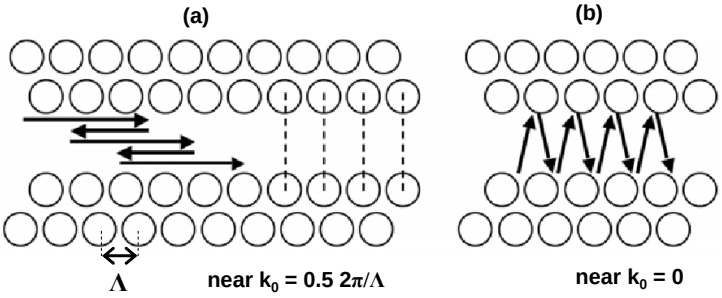

Figure 3.17: Illustration of the two possible mechanisms for achieving slow light in photonic crystal waveguides, namely (a) coherent backscattering and (b) omnidirectional reflection [72].

To better understand the mechanism of the slow light regime, let us analyze the example of a PhC waveguide made of silicon, with a hexagonal lattice of air holes, with the following geometry: the diameter of the holes is 220 nm and the pitch Λ (space between the holes) is 370 nm. Many numerical methods can be used on the simulation of PhCs, and the choice here is to use FEM, although the most commonly used methods for this kind of analysis are finite-difference time-domain (FDTD) [73] and plane wave expansion (PWE) [74] methods. Since the structure is not uniform in the z direction, as in the case of the previous ordinary channel waveguides, the analysis requires In-Plane propagation equations. A unit cell can be defined (shown at the top of Fig. 3.18, according to the symmetry of the structure, and by applying Floquet periodicity as boundary conditions [74], it is possible to calculate the dispersion

curve of the guided mode of the PhC waveguide, as shown in Fig. 3.18 (a). For simplicity, only the curve corresponding to the even mode is plotted, instead of the complete band diagram.

The group velocity v_g of light with frequency ω in an optical waveguide is given as

$$v_g = \frac{\mathrm{d}\omega}{\mathrm{d}k} = \frac{c}{n_g}, \tag{3.10}$$

where k is the wavevector, c is the speed of light in vacuum and n_g is the group index.

Using Eq. (3.10), it is possible to calculate the group velocity curve, plotted in Fig. 3.18 (b). It reveals a dramatic reduction in v_g for increasing wavevectors (lower frequencies). As expected, the group velocity $v_g \approx c/4$ is close to that of light propagating in a conventional silicon waveguide, for $k_z \leq 0.3$. For $k_z > 0.3$, v_g decreases monotonically below $c/20$. Near $k_z = 0.5$, v_g approaches zero, hence, addressed as the slow-light regime [75].

The knowledge of the modal field distribution can help on understanding the characteristics of the W1 PhC waveguide. At the bottom of Fig. 3.18 are plotted the modal field distributions for the even PBG mode for three different wavevectors marked by a pentagon, a circle and a square. For $k_z \leq 0.3$ with $v_g \approx c/4$ (pentagon), the mode is seen to be well confined in the waveguide core and the mode profile looks similar to that of a fundamental mode in a ridge waveguide. Hence, in this index-like regime the mode is usually referred to as being index-guided. Entering the slow-light regime (circle), the mode starts to penetrate into the PhC cladding and, eventually, has its field highly concentrated in the first and second row of holes (square).

In order to achieve a group velocity of c/n_g, the maximum bandwidth can then be determined as follows:

$$\Delta\nu = \frac{1}{2\pi}\,\frac{c}{n_g}\,0.5\frac{2\pi}{\Lambda} = \frac{c}{2n_g\Lambda}. \tag{3.11}$$

The slowdown factor S is defined as the ratio of the phase velocity over the group velocity [72]

$$S = \frac{v_p}{v_g}, \tag{3.12}$$

where $v_p = \omega/k_0$.

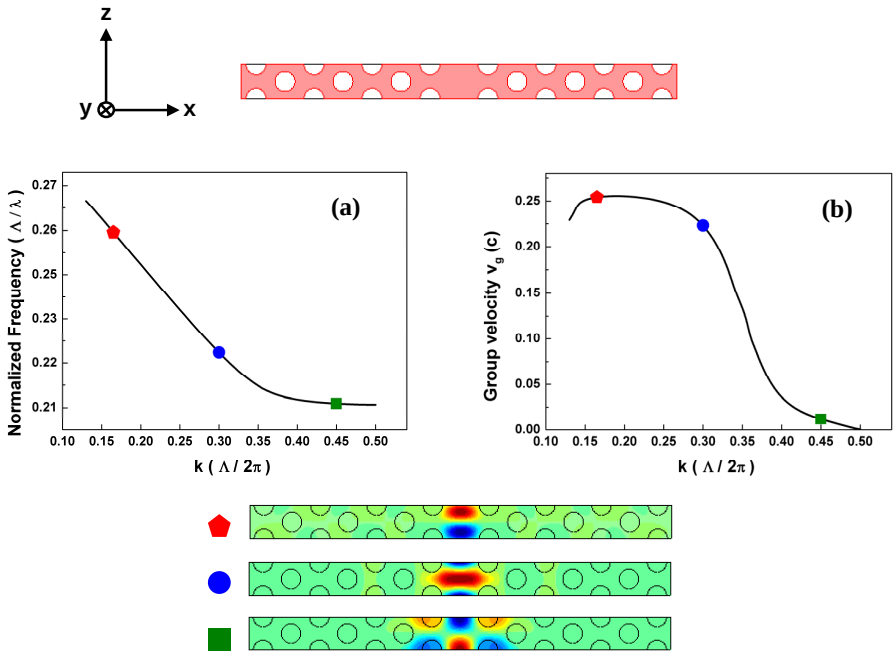

Figure 3.18: Characteristic curves of guided mode of the PhC waveguide: (a) Dispersion curve, (b) Group velocity. The top figure shows the geometry simulated and the bottom figures show the distribution of the z-component of the magnetic field for different values of k. The light propagates in the z direction.

3.6.3 Acousto-optic modulation enhancement by slow light

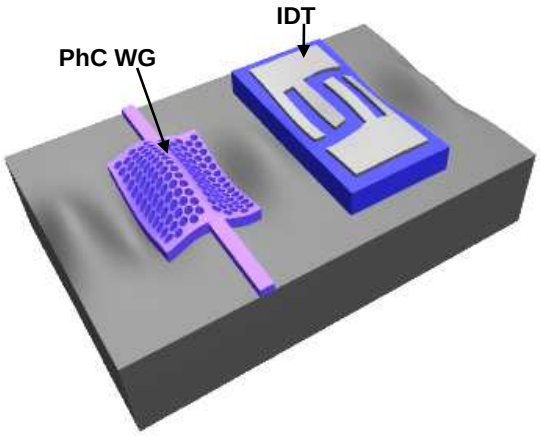

Figure 3.19: Artistic representation of the PhC WG being modulated by a SAW excited by an IDT.

Slow group velocities are known to enhance nonlinear effects as a consequence of the compression of the local energy density. It has been shown that the sensitivity of the phase to induced changes in the refractive index can be drastically enhanced if one operates in the regimes of slow group velocities [76]. Therefore phase modulation of light by SAWs can also be enhanced in the slow light regime [77, 78]. The purpose of this section is to analyze the enhancement of SAW-induced phase modulation that can be achieved by replacing an ordinary optical waveguide by a PhC waveguide, such as illustrated in Fig. 3.19. To quantify this enhancement, a figure of merit for the increase of the phase shift induced by a SAW in a PhC waveguide compared to in a straight waveguide is defined as:

$$FoM = \frac{\Delta\phi_{\text{PhC modulated}} - \Delta\phi_{\text{PhC not modulated}}}{\Delta\phi_{\text{WG modulated}} - \Delta\phi_{\text{WG not modulated}}}, \tag{3.13}$$

where $\Delta\phi$ is the unwrapped relative phase delay measured between the input and output of the ordinary and PhC waveguides, in the absence and presence of strain, in the positions shown in Fig. 3.20.

Now instead of using the super-cell, the whole device is modeled, to be

able to account for the phase changes in the propagating light. The system is composed of a W1 PhC waveguide, with ridge waveguides serving as coupling media at the input and output facets. The 2D In-Plane TE mode equations are used, and an input field is excited at the left facet of the ridge waveguide. The distribution of the magnetic field H_z for a wavelength inside the photonic bandgap is shown in Fig. 3.20, as well as the field in a straight waveguide with the same wavelength.

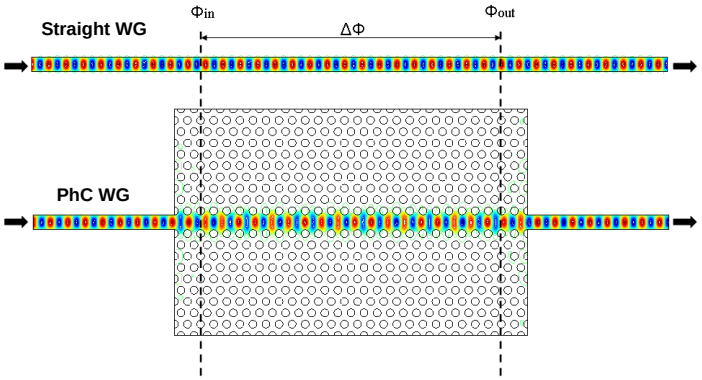

Figure 3.20: Propagation of the magnetic field in the z-direction for a straight waveguide and for the PhC waveguide. The definition of $\triangle\phi$ used in the FoM is pointed out in the figure.

A SAW modulation is now to be introduced in the model. In this case, the SAW propagation is perpendicular to the plane where the light propagates. To avoid a 3D modeling system, the SAW modulation is introduced as an instantaneous distribution of changes in the refractive index of the dieletric material, as presented in Fig. 3.21. The maximum change in the refractive index is assumed to be $\Delta n/n = 10^{-3}$. Initially the acoustic wavelength is assumed to be much larger than the periodicity of the structure, and the acoustic beam width is assumed to have a Gaussian distribution with $1/e$ smaller than the length of the PhC, therefore not affecting the coupling ridge waveguides.

By measuring the output power of a waveguide for different input wavelengths, it is possible to obtain the transmission spectrum. In the case of a straight waveguide, the transmission spectrum is a nearly flat curve, which decays very slowly due to the mode dispersion. In the case of the PhC WG, the

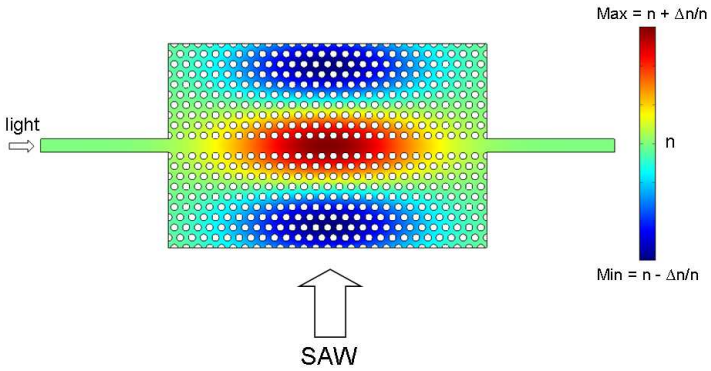

Figure 3.21: Distribution of changes in the refractive index induced by the SAW for a certain SAW wavelength.

transmission is high inside the photonic bandgap, and shows a cutoff at the wavelength that corresponds to the band edge. This behavior can be observed in Fig. 3.22 (a). The region of the cutoff corresponds to the region of slow-light regime. The FoM for different wavelengths is plotted in Fig. 3.22 (b), and its direct correspondence with the light group velocity can be observed. For this example, the phase modulation can be enhanced up to 300 times by making use of the slow group velocities of the PhC waveguide, and still having a transmission around 60%. Comparing with the group velocity curve shown in Fig. 3.18 (b), the peak in enhancement would correspond to $n_g \approx 150$. Using Eq. (3.11), a bandwidth of ≈ 2.74 THz is obtained, what corresponds to about 1.4 % of the carrier wavelength. This could still be enough for several applications, but the bandwidth can also be increased by tailoring the dispersion of the PhC waveguide [75], with the penalty of reducing the FoM. The slow down factor obtained from the curves in Fig. 3.18 and Eq. (3.12) is also plotted in Fig. 3.22 (c) for comparison purposes. The values of the FoM and S are of the same order of magnitude, but don't exactly match due to the non-uniform changes of refractive index induced by the SAW and due to the inclusion of the optical coupling aspects in the model. In practice, the values of FoM can be expected to decrease due to imperfections in fabrication, but nevertheless values as high as 61 have been experimentally obtained for different geometry and material [77].

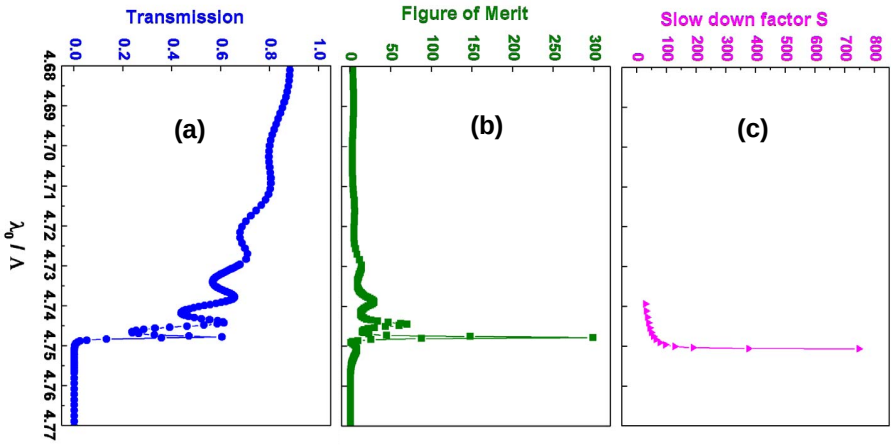

Figure 3.22: Slow down factor, transmission and FoM of the PhC waveguide.

The FoM for different SAW wavelengths is now calculated, and the result in shown in Fig. 3.23. As the SAW wavelength becomes smaller, it becomes comparable to the dimensions of the waveguide region, where most of the optical power is confined. That means that the strain fields can have opposite signs inside this region and the overall integral of the strain-optical overlap in the region can be reduced, reducing the FoM.

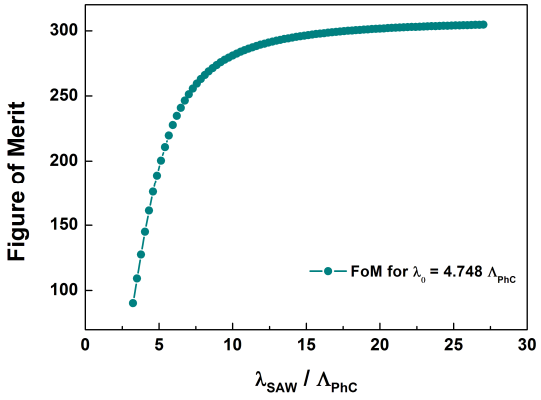

Figure 3.23: Figure of Merit for different SAW wavelengths.

3.7 Membranized photonic waveguides

The use of Lamb waves for acousto-optic modulation has first been proposed by Chang [18] as a first attempt of exciting both an acoustic guided wave and an optical guided wave in the same film. The optical mode was guided by a planar waveguide. This approach was overtaken by the use of surface-bound waves [79], and so far the use of Lamb waves had not been applied on the modulation of channel 3D waveguides. This application is investigated in this section.

As an attempt of improving the overlap between the acoustic and the optical fields, membranized waveguides (as shown in Fig. 3.24) are investigated. By removing part of the material underneath the optical waveguides, a second mechanically free surface is created. These thin plates can support different types of acoustic modes (as discussed in Chapter 2), opening up the possibility to confine the acoustic modes in smaller volumes and tailor the strain distribution in the area of the optical waveguide. The increase in vertical index confinement due to the presence of air underneath the waveguide also improves the optical mode confinement, as seen in the inset of Fig. 3.24.

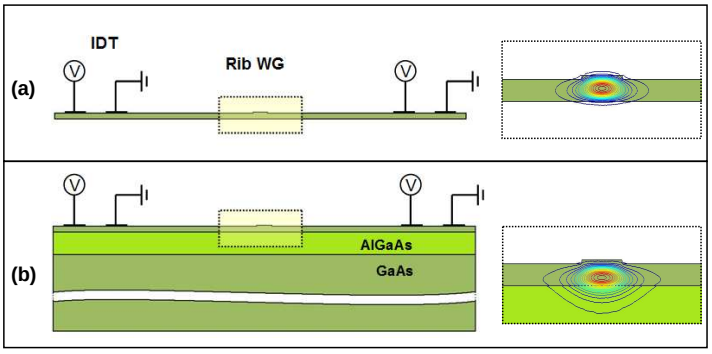

Figure 3.24: Configurations of (a) membranized and (b) bulk devices for acousto-optic devices based on rib waveguides. The inset to the right shows the distribution of the optical power of the fundamental TE mode.

The material platform chosen for this study is GaAs, because it is an inherently piezoelectric semiconductor and therefore makes it possible to excite acoustic waves directly on the membrane. Processes similar to those used in

micromachining technology could be used for the fabrication of such structures [80]. Other non-piezoelectric semiconductor materials such as silicon and InP can also be used, in combination with a piezoelectric thin film such as ZnO for the excitation of the acoustic wave.

The objective is to make use of Lamb waves guided in the membrane to modulate the light confined in the rib waveguide. As discussed in Chapter 2, Lamb waves appear in two different forms, symmetrical and anti-symmetrical. In a plate of thickness h at a frequency f, a finite number of these two types of waves can exist, differing from each other by their phase velocities and the distribution of mechanical displacements and strain fields along the thickness of the plate. High frequency Lamb modes can be excited in very thin plates, overcoming one of the main drawbacks of conventional acousto-optic devices which is the low frequency range. Very recently, the idea of using a higher order Lamb mode (a_1) to increase the frequency range of devices has been applied on the construction of a resonator [81], achieving a frequency of 6.3 GHz. The use of Lamb waves to modulate light in channel waveguides is introduced for the first time here [82].

Lamb waves can also be excited by IDTs [83]. To excite the Lamb modes in membranes in the numerical model, a model similar to the one used previously here for the Rayleigh waves is built, using Eq. (3.4) and Eq. (3.5), with a few modifications. First, the absolute value of the y coordinate is now used in the equations, and the membrane in centered in $y = 0$, what would be equivalent to having IDTs on both sides of the membrane. This is common practice for modeling Lamb waves [84]. The second modification is that displacements are now introduced on the left and right boundaries, as shown in Fig. 3.25. By doing this, any Lamb mode supported by the structure can be excited independently, including both the symmetric and the anti-symmetric ones.

The thickness of the membrane is chosen to be large enough to allow some higher order Lamb modes to be excited. Since the thickness of the membrane determines in this case the geometry parameter h of the waveguide, that implies the use of large core rib waveguides. The first three Lamb modes of the structure are investigated: a_0, s_0 and a_1. Fig. 3.26 shows the geometry used, the distribution of the TE optical mode, and the horizontal (u_x), vertical (u_y) and total displacement ($\mathbf{u}$) distributions for the first three Lamb modes of the structure.

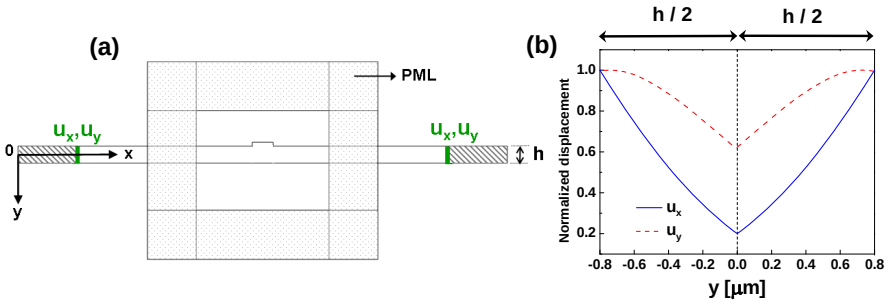

Figure 3.25: (a) Model used on the simulation of the membranized rib waveguides, showing the mechanical and the optical PMLs and where the boundary conditions are applied, (b) plot of the u_x and u_y displacements on the left excitation boundary.

These modes present different velocities, as presented on the dispersion curves in Fig. 3.27 (a). Using these modes to modulate the effective index of the optical modes in the rib waveguides leads to very different results, as seen in Fig. 3.27 (b). The change in n_{eff} induced by the a_1 mode is ~18 times higher than the one induced by the Rayleigh mode, with a frequency almost 2 times higher. Other higher order modes could lead to even better results, and the next step would be to investigate several modes to seek for the optimal strain-optic overlap. Based on these results, the concept of using Lamb waves for acousto-optic modulation of light in channel waveguides proves to be a very promising path to obtain integrated ultrasonic-photonic devices with higher performance and higher operation frequency.

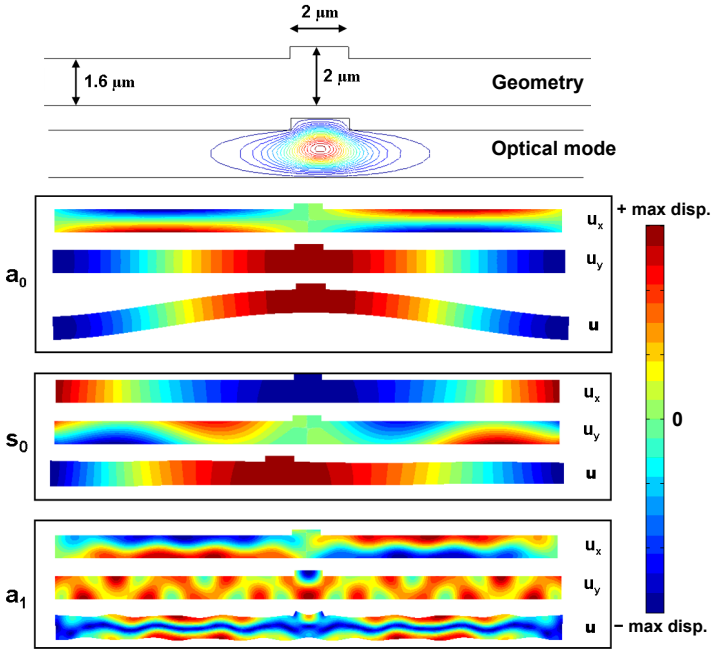

Figure 3.26: Membranized GaAs rib waveguide: geometry, TE optical mode, and horizontal, vertical and total displacement distribution for the 3 first Lamb modes of the structure: a_0, s_0 and a_1.

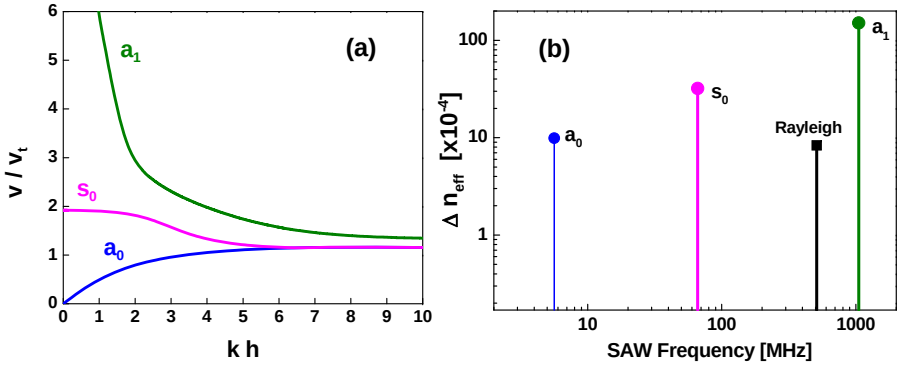

Figure 3.27: (a) Dispersion curves for GaAs for the a_0, s_0 and a_1 Lamb modes, (b) Changes in the effective index of the TE and induced by the Lamb modes and the Rayleigh mode.

Chapter 4

Design of Ultrasonic-photonic circuits

In this chapter the main aspects related to the design of ultrasonic-photonic devices based on Mach-Zehnder interferometers are discussed. First, a brief literature review on previous works illustrates the main advantages and challenges related to such devices, and shows where the possibilities are for new inventions. Then the main aspects of the design process are presented, showing also the challenges related to the numerical methods to be used for that purpose.

4.1 Mach-Zehnder Interferometers

The acoustic modulation of a straight waveguide only promotes a phase shift of the light. In order to be able to use this effect in other applications than phase shifting, one must make use of smarter configurations, such as interferometers. Mach-Zehnder interferometers (MZIs) are, for this reason, fundamental tools for the construction of SAW-based photonic devices. By spacing the arms of the interferometer properly, the relative phase change can be adjusted and interfered constructively or destructively, leading to a new class of devices that will be briefly discussed now.

The use of acousto-optically modulated MZIs was first proposed by Gorecki

et al. [20]. Their proposal was to modulate only one of the arms of the interferometer, using an acoustic absorber to avoid modulation of the other arm. A different approach was introduced by Lima *et al.* [21] by modulating both arms of the interferometer simultaneously by the same SAW, and adjusting the space between the arms to be an odd multiple of half the wavelength of the SAW. That way, the light propagating in the two arms experiences refractive index changes of opposite phases during the passage of the SAW, like illustrated in Fig. 4.1, and the device would hence work as a modulator.

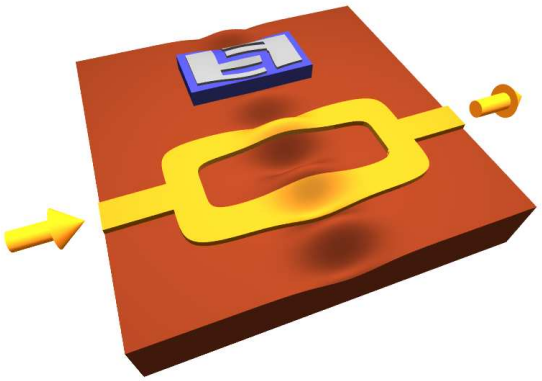

Figure 4.1: Illustration of a waveguide-based Mach-Zehnder interferometer being modulated by a SAW generated by an IDT.

The output electric field of the MZI modulator is given by:

$$E_{out} = \frac{E_0}{2}\left\{\sin[\omega t - \Delta\phi_1 \sin(\omega_{SAW} t)] + \sin\left[\omega t - \Delta\phi_2 \sin\left(\omega_{SAW} t - \frac{\pi}{2}\right) - \Delta\phi_S\right]\right\}, \tag{4.1}$$

where E_0 is the electric field amplitude at the MZI input, $\Delta\phi_{1,2} = \omega\, \Delta n\, L/c$ are the phase shifts caused by the SAW modulation on each arm, respectively, ω_{SAW} is the angular frequency of the SAW and $\Delta\phi_S$ is the static phase shift introduced by a difference in length in one of the arms. Later on, this concept was extended to the simultaneous modulation of multiple interferometer arms [22, 85], which could give the device the capability of realizing other functions such as optical switching.

4.2 Numerical methods for optical propagation calculation

While Comsol Multiphysics has great flexibility for modeling photonic devices, the computational demands of the general finite element method make it most suitable for small devices, on the order of a few microns in extent. Many integrated optical devices are much larger, having lengths of hundreds of microns or millimeters. Therefore to model the propagation of light in such devices, other numerical methods are usually applied, such as the beam propagation method and the eigenmode expansion method. This section will discuss the working principle of a few different numerical methods used in design calculations. The methods are based on different approximations and therefore have different accuracy, as shown in the example of mode calculation in Fig. 4.2. Each method is used here for different purposes, trying to take advantage of what each of them can calculate more efficiently or accurately.

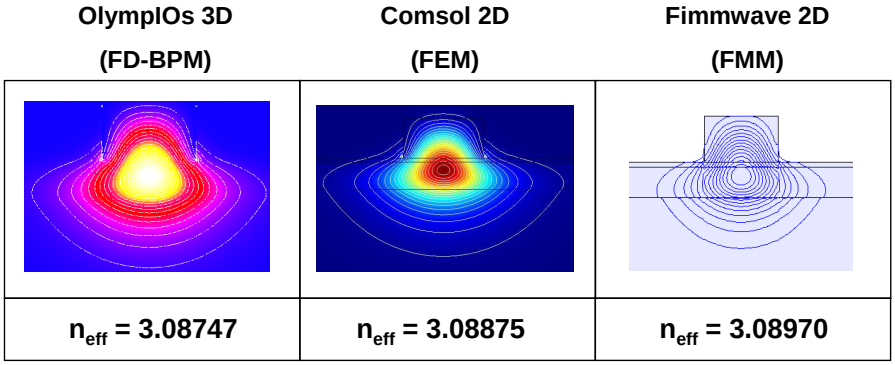

Figure 4.2: Effective index and optical power distribution of TE and TM modes in GaAs rib waveguides calculated using different softwares. The polarization designation differs due to the different coordinate systems adopted.

The geometrical parameters used in this chapter are again the ones previously defined in Fig. 3.4.

4.2.1 Effective index method

The effective index method (EIM) [86, 87] is based on a separation of the 2D wave equation into two 1D equations. The structure is split into x-invariant substructures, such as shown in Fig. 4.3. Calculations on these substructures are performed and the solutions are combined into a y-invariant structure, which is again calculated to obtain the final field and propagation constants. For each lateral position x, the 1D modal wave equation is solved and an effective index is obtained. Then, a new 1D structure is obtained from which the overall propagation constant is calculated.

The EIM yields to a simple condition between the transversal sizes of rib waveguides for single mode propagation [88]:

$$t < \frac{r}{\sqrt{1-r^2}}, \tag{4.2}$$

where

$$\begin{gathered} t = \tfrac{w_{eff}}{H_{eff}}, \;\; r = \tfrac{h_{eff}}{H_{eff}}, \\ h_{eff} = h + q, \;\; H_{eff} = H + q, \\ w_{eff} = w + \tfrac{2\gamma_c}{k\sqrt{\left(n_{core}^2 - n_{top}^2\right)}}, \\ q = \tfrac{\gamma_c}{k\sqrt{\left(n_{core}^2 - n_{top}^2\right)}} + \tfrac{\gamma_s}{k\sqrt{\left(n_{core}^2 - n_{clad}^2\right)}}, \\ \gamma_{c,s} = 1 \text{ for TE modes and} \\ \gamma_{c,s} = \left(\tfrac{n_{top,clad}}{n_{core}}\right)^2 \text{ for TM modes.} \end{gathered} \tag{4.3}$$

where n_{top}, n_{core}, n_{clad}, h, H and w are defined in Fig. 3.4.

The effective index method is meant to be used for quasi-planar modes, assuming small y-derivatives of the permittivity. For structures produced by etching techniques, the approximation may be valid, if either the etching depth remains small when compared with the typical vertical guiding dimensions, or if the local field strength at the rib flanks is small for the mode under investigation.

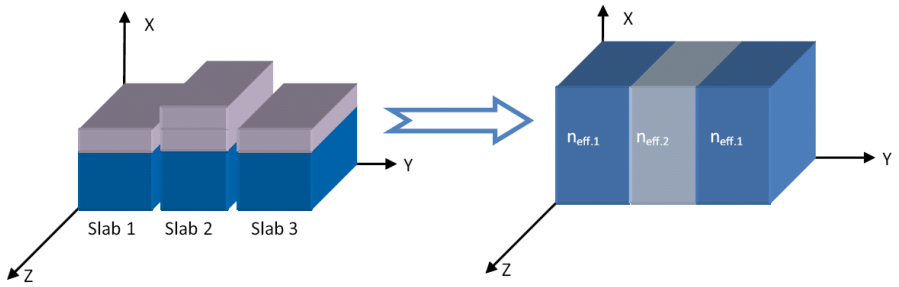

Figure 4.3: Illustration of the effective index method.

4.2.2 Beam propagation method

The OlympIOs software [89] uses the Finite-Difference Beam Propagation Method (FD-BPM) to determine the propagation of light in a 2D domain. The equation to be solved (for the BPM method) is the one-dimensional scalar wave equation in the slowly varying amplitude approximation, i.e., assuming an $e^{i\omega t}$ time dependence, and paraxial propagation in the positive z-direction in a medium with a mean refractive index n_0, chosen so that it should as closely as possible match the expected index of propagation of the light in the structure. For TE modes, the equation to be solved is:

$$2ik_0 n_0 \frac{\partial \psi}{\partial z} = \left\{ \frac{\partial^2}{\partial x^2} + k_0^2 [n^2(x,z) - n_0^2] \right\} \psi, \tag{4.4}$$

where $\psi = E_y e^{ik_0 n_0 z}$. Since ψ varies slowly with z, its second derivative with respect to z is ignored. A uniform discretization with step sizes Δx and Δz is used, and the equation is solved for each of the steps. This process is repeated until the wave reaches the boundary of the domain resulting in a final field distribution. The resulting collection of successive field profiles gives a clear picture on how the wave propagates through a structure, as shown in Fig. 4.4. The number of step sizes is decided by the user, and will influence on the accuracy of the calculation.

For design purposes, the two dimensional BPM is normally sufficient to achieve a rather good estimate about the device performance, given a few boundary conditions. The advantage compared to the more robust 3D BPM is the speed, reduced memory usage and more simplified analysis. In order to

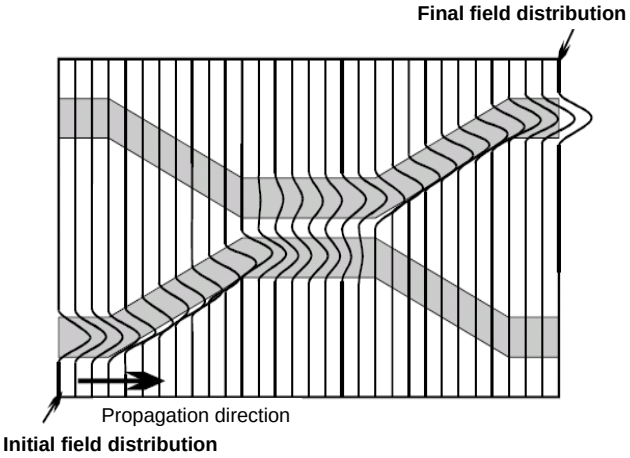

Figure 4.4: Example of a BPM simulation of a propagating wave through a structure (directional coupler).

use the 2D approach, the EIM must be first applied to the real 3D structure in order to obtain the effective indices used in the model. More details on the 2D models can be found in [90]. This limits the accuracy of the 2D approach for the cases where the mode can't be well approximated by effective indices, such as in the case of weakly confined modes in low index contrast rib waveguides. For these cases, the 3D approach should be used, or other numerical methods should be applied.

4.2.3 Film mode matching method

The Fimmwave software [91] is designed to model a wide variety of 2D and 3D waveguide structures using a rigorous fully vectorial formalism. The program is based around a fully vectorial waveguide solver based on the film mode matching (FMM) method due to Sudbo [92, 93]. Fimmwave has a fully vectorial solver based on the FMM method, which is very suitable for waveguide structures with a rectangular geometry. It is a semi-analytic method that does not need any discretization of the structure, provided that the structure can be well described by a finite set of rectangles. This makes it very efficient in modeling waveguides that have very small features or are very wide, or both.

It is ideal for epitaxially grown structures that might include very thin layers.

Taking as a reference the example of a semiconductor ridge waveguide, the working principle of the method is as follows. The waveguide cross section is considered to be a sandwich of slices, like shown in Fig. 4.5. Each slice is considered to be cut from a film waveguide. The FMM method involves finding the TE and TM modes of each film (or just the scalar modes if the guide is weak), collecting the modes that have the same z-component k_z of the modal wavevector, and matching the field distributions at the slice interfaces by adjusting the modal amplitudes in each film. Only for certain values of k_z a set of non-zero mode amplitudes with matching distributions at the slice interfaces can be found. Each set constitutes a waveguide mode. The continuous spectrum of unbound film modes must somehow be discretized. Usually this discretization is achieved by the introduction of artificial boundaries, placed sufficiently far from the waveguide core so that for the mode of interest both the field components and their gradients are negligible.

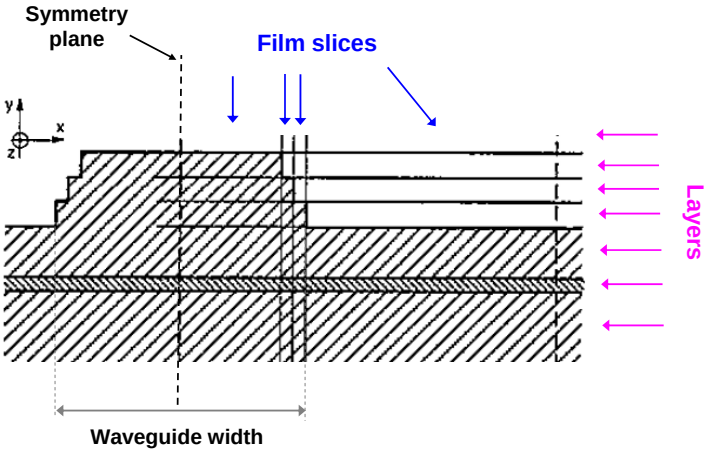

Figure 4.5: FMM geometry of a typical semiconductor ridge waveguide cross section, modeled by a number of film guide slices. The sloped sides of the ridge have been approximated by staircases [92].

4.2.4 Eigenmode expansion method

The Fimmprop software [94] is a tool for simulating 2D and 3D propagation phenomena in waveguides. Fimmprop is based on the eigenmode expansion (EME) method, and allows one to analyze a variety of 3D waveguide structures in a rigorous and fully vectorial manner [95]. In a structure where the optical refractive index does not vary in the z direction, assuming a single wavelength and time dependence of the form $e^{i\omega t}$, the method seeks for solutions of Maxwell's equations of the form

$$\mathbf{E}(x, y, z) = \mathbf{e}_m(x, y)e^{i\beta_m z}. \tag{4.5}$$

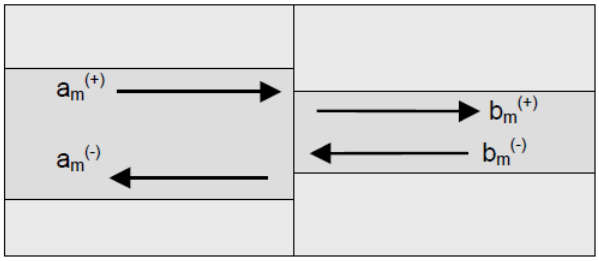

Figure 4.6: EME amplitude coefficients at a joint between two waveguides.

Mathematically, $\mathbf{e}_m(x, y)$ and β_m are the eigenfunction and eigenvalue of the solution. In a typical waveguide, there are a few guided modes (which propagate without loss along the waveguide), but in addition there are an infinite number of radiation modes (which carry optical power away from the waveguide). The guided and radiation modes together form a complete basis set. In other words, any solution of the Maxwell's Equations in the region of the waveguide can be expressed in terms of a superposition of the forward and backward propagating modes:

$$\mathbf{E}(x, y, z) = \sum_{k=1}^{M} \left(a_k e^{i\beta_k z} + b_k e^{-i\beta_k z}\right) \mathbf{E}_k(x, y) \tag{4.6}$$

for the electric field and

$$\mathbf{H}(x, y, z) = \sum_{k=1}^{M} \left(a_k e^{i\beta_k z} + b_k e^{-i\beta_k z}\right) \mathbf{H}_k(x, y) \tag{4.7}$$

for the magnetic field, where a_k and b_k are the forward and backward amplitudes, respectively. For a junction between two waveguides, such as shown in Fig. 4.6, due to the continuity conditions for the fields, e.g. the tangential electric fields must be equal on each side of the interface, one obtains:

$$\sum_{k=1}^{M} \left(a_k^{(+)} e^{i\beta_k z} + a_k^{(-)} e^{-i\beta_k z} \right) \mathbf{E}_{kt}^{a}(x,y) = \sum_{k=1}^{M} \left(b_k^{(+)} e^{i\beta_k z} + b_k^{(-)} e^{-i\beta_k z} \right) \mathbf{E}_{k,t}^{b}(x,y). \tag{4.8}$$

Applying these conditions, together with conditions on the longitudinal electric field and the fields, and noting that the modes are orthonormal, and after some mathematics, a relationship between the coefficients can be deduced:

$$\begin{bmatrix} \mathbf{a}^{(-)} \\ \mathbf{b}^{(+)} \end{bmatrix} = S_{J} \begin{bmatrix} \mathbf{a}^{(+)} \\ \mathbf{b}^{(-)} \end{bmatrix} \tag{4.9}$$

where S_J is the scattering matrix for the joint. A device can be described by several S-matrices, and once the individual S-matrices are calculated, combined S-matrices can be computed, until an S-matrix for the whole device is obtained.

4.3 Single mode waveguides

Rib dielectric waveguides are quite complex to model, usually approximate schemes are developed. The main issue is to find the geometry that allows the propagation of only one mode. By using numerical methods such as FEM, many spurious solutions are obtained, and it is difficult to distinguish those from the physical solutions. Several approximations have been proposed in the literature to solve this problem, the most standard ones being the one proposed by Marcatili [96] and by Soref [97].

Most of the studies are concerned with large-core waveguides [98, 65, 88] though, and the objective here is to make compact devices and therefore use waveguide with small dimensions whenever possible.

The approach here was to use the FMM method to determine the single-mode condition for different geometries. Using this method, it is possible to calculate a parameter called *side loss*, which is an estimation of how quickly

a mode would radiate away through the lateral boundaries, normalized to the power flux in the z direction. By calculating the side losses of the first higher order mode, the dimensions for which this mode starts to be leaky can be found, as shown in Fig. 4.7 (a). Leaky higher order modes do not propagate, and therefore for these dimensions the waveguide will behave as single mode. This analysis was performed for waveguides with small dimensions (H = 500 nm) and the results are presented in Fig. 4.7 (b).

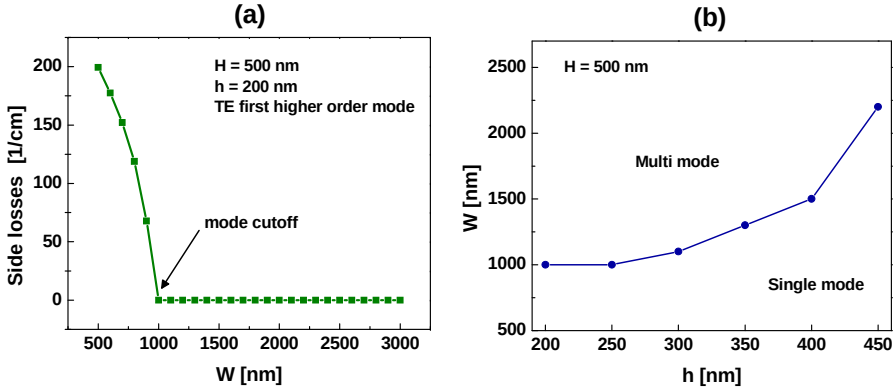

Figure 4.7: (a) FMM side loss calculation for the first higher order TE mode of a waveguide with different widths and h = 200 nm (b) Single-mode / multi-mode cutoff curves for TE mode of GaAs/AlGaAs rib waveguide with H = 500 nm.

In the previous modeling study of membranized rib waveguides in Chapter 3, waveguides with large core were used. In the case of rib waveguides with large core ($H > 1\mu m$), the EIM can provide a good indication of the geometries that can be used for single mode guiding [88].

The single/multi-mode cutoff curve for membranized GaAs rib waveguides with large core calculated using the EIM method is presented in Fig. 4.8. It confirms that the dimensions used in the example in Chapter 3 lead to single mode guidance.

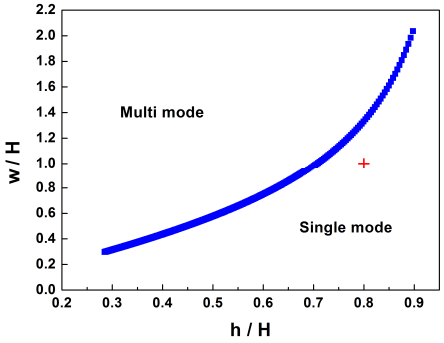

Figure 4.8: Mode cutoff curve for GaAs membranized rib waveguide with large dimensions calculated by the effective index method. The cross indicates the dimensions used in the example of Chapter 3.

4.4 Waveguide couplers

Since photonic devices are usually connected to at least one optical fiber, it is of major importance to obtain an efficient coupling of light between the fiber and the photonic device. The very small refractive index difference in a glass fiber results in a weakly guided optical mode with a typical mode size of 8–10 μm. In semiconductor waveguiding devices, such small refractive index differences can only be achieved with extremely small compositional changes. In an optimized semiconductor waveguide component, however, the mode sizes are usually smaller than 2 μm. Besides, unlike the circular mode in a fiber, the mode shape in a semiconductor device is usually highly asymmetric, resulting in an additional mode mismatch between the fiber mode and the semiconductor waveguide mode. There are several approaches to improve the fiber-chip coupling efficiency, such as the use of tapered/lensed fibers [99]. This approach is adopted on the characterization of the devices here studied. However, this approach alone still suffers from the field mismatch problem, since only the size and not the shape of the optical mode is converted. The reduction of the coupling loss is usually at the expense of the alignment tolerances.

Mode size converters can be used in order to achieve a larger and more symmetric near field pattern at the device facet. They allow both low coupling loss and large alignment tolerances. The lowest coupling losses (or field mis-

match losses) are achieved when the semiconductor waveguide optical mode and the fiber optical mode are fully matched. The optical mode in a fiber has a quasi-Gaussian shape. Therefore, tapered waveguides are often designed to have a nearly Gaussian mode-profile at the waveguide output facet. There are many different technological approaches for the monolithic integration of mode size converters (or tapers) with semiconductor devices, such as lateral, vertical, combined and special tapers designs [100]. To avoid further complexity in the fabrication process, the technology adopted here is the use of lateral tapers.

4.4.1 Lateral tapers

Lateral tapers or lateral mode size converters have the most simple and straightforward design of all tapers, where only the width of the waveguide is changed without affecting the vertical waveguide structure, such as shown in Fig. 4.9 (a). As the optical beam propagates from the large end of the taper to the smaller end, it contracts laterally, owing to diffraction, thereby concentrating the optical power over a narrower region.

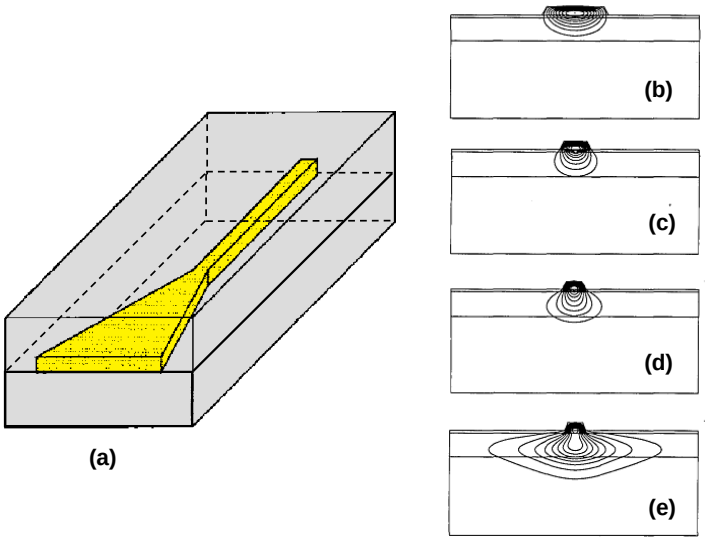

Figure 4.9: (a) Representation of a laterally tapered waveguide, (b) – (e) Cross section of rib waveguide and level lines of the electric field for decreasing width of the rib [101].

The structure is designed such that for the limiting case of infinite rib width, the system supports essentially a single mode, which resides mainly in the upper waveguide core, whereas in the limiting case of zero rib width, the corresponding structure supports a mode that resides mainly in the lower core. Figs. 4.9 (b) – (e) show the contour plots of the field for a tightly confining wide guide and progressively narrower guides [101]. The layer thicknesses and refractive indices are the same; only the rib width is different. For wide widths such as in (b), the mode is held tightly confined in both the transverse and the lateral dimensions under the rib; for narrow widths the mode spreads and becomes much larger in both dimensions as in (e). If the rib width is tapered gradually enough to preserve nearly adiabatic propagation, the mode size and location can be transformed from that in (b) to that in (e) by lateral patterning only, which can be readily achieved using a single step of lithography and etching.

Another interesting approach is the one suggested by Smith *et al.* [102], where a mesa is created underneath the rib waveguide, leading to a tapered-rib adiabatic-following fiber coupler, as shown in Fig. 4.10 (a). The working principle of the device is shown in Fig. 4.10 (b). When the rib is initially narrowed, the mode remains well confined. As the waveguide rib is further narrowed to $w \sim 1.3$ μm, the fundamental mode is pushed down into the mesa. For $w \sim 1.0$ μm, the fundamental mode has moved almost entirely into the mesa, where it is well suited for overlap with the approximately Gaussian-shaped mode of an optical fiber. The fundamental mode remains in the mesa and is virtually unchanged as the rib width is narrowed further.

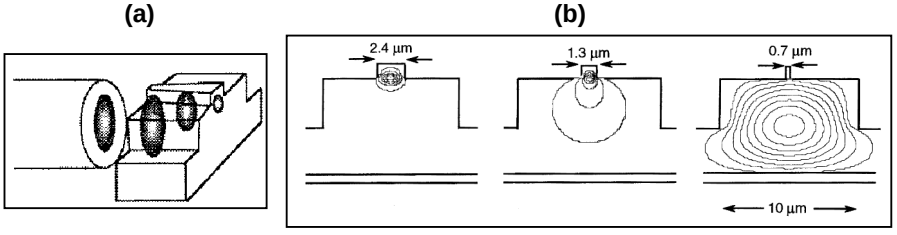

Figure 4.10: (a) Light coupled from a fiber to a mesa waveguide then traveling through a tapered-rib adiabatic-following fiber coupler and exiting from a rib waveguide, (b) The fundamental TE mode for three rib widths (electric field contours) with a mesa underneath the rib. From [102].

4.5 Bending losses

In the construction of integrated photonic devices, bent waveguides are used for optical-path direction changes. Bent waveguides are also used in the construction of rings, splitters, delays, or even simply for optimized physical space distribution on a chip. The schematic representation of a bent waveguide is shown in Fig. 4.11 (a). As the curvature radius R becomes smaller, an optical-path direction is changed at a shorter propagation distance. On the other hand, optical bending loss increases as R decreases. At a certain radius r_c, the optical power is carried at the speed of light by the guided mode. The optical power in the guided mode at $r \geq r_c$ radiates towards the outside of the arc [38]. This inherent radiation loss due to optical bending should be evaluated when designing bent waveguides.

A rigorous analytical analysis of bent waveguides is complex [103]. The software Fimmwave has an application for the calculation of bent waveguides, using the scheme shown in Fig. 4.11 (b), where the bending loss for a 90° bend is simulated, given the curvature radius. This method was used on the calculation of bending losses of a GaAs rib waveguide with geometry $h = 200$ nm, $H = 500$ nm and $w = 600$ nm, for different curvature radii. The results can be seen in Fig. 4.12, where it is shown that the losses increase very dramatically for tight bends. In contrast, the optical modes of SOI ridge waveguides are almost insensitive to this range of bend curvatures, due to the strong confinement.

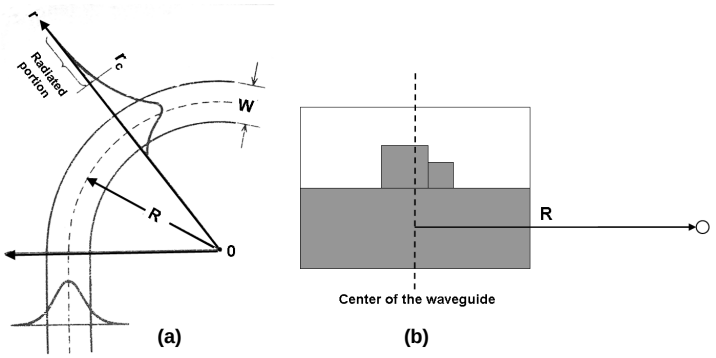

Figure 4.11: (a) Field distribution of the guided mode in a bent waveguide with a curvature radius R (from [38]), (b) Geometry in Fimmwave of waveguide bent to the right side, with curvature radius R.

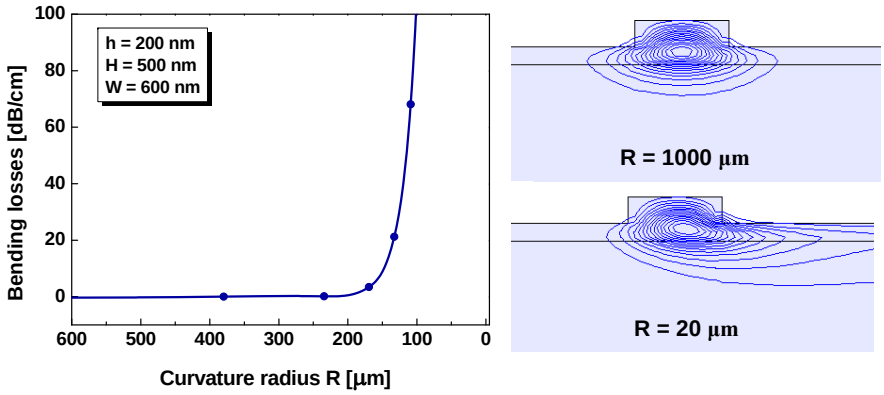

Figure 4.12: (a) Bending losses calculated for GaAs/AlGaAs waveguide with $h = 200$ nm, $H = 500$ nm and $w = 600$ nm, and optical power distribution of the TE mode for bend radius of (b) 1000 μm and (c) 100 μm.

4.6 S-bends

In many applications of integrated optics, such as modulators, couplers and analog-to-digital converters, it is necessary to connect two parallel noncollinear single-mode-channel waveguides that have a given amount of transverse offset. If this offset is to be achieved, the waveguide must bend. Typically, two corner bends with some bend angle, as shown in Fig. 4.13 (a), are used to couple the light from one straight portion of the waveguide to the other straight portion.

There are three common S-shaped bend geometries: two circular arcs with constant curvature (double-arc), sine-generated curve, and cosine-generated curve, as shown in Figs. 4.13 (b)–(d). The equations for an S-bend with length L along the z axis, and height B for these three geometries are given next [104].

The sine S-bend is a waveguide, for which the path line is built around sine function, given by:

$$x(z) = \frac{B}{2\pi} \sin\left(\frac{2\pi}{L} z\right) - \frac{B}{L} z. \tag{4.10}$$

Cosine S-bend is a waveguide, for which the path line is built around cosine function, given by:

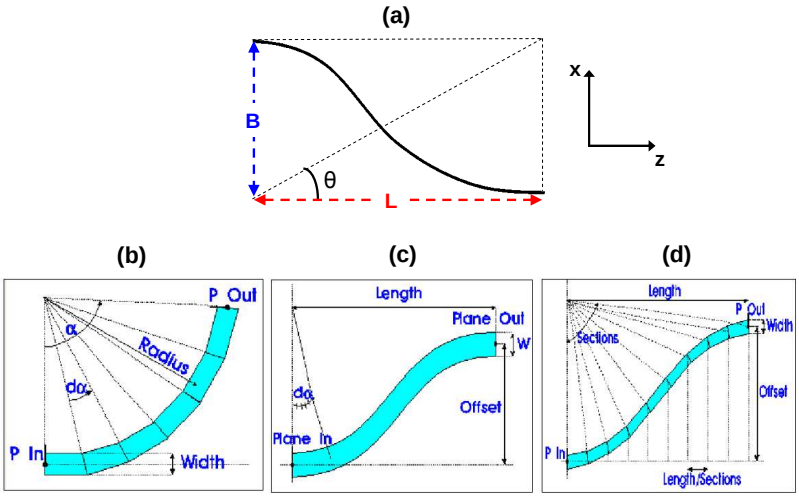

Figure 4.13: Types of waveguide S-bends: (a) geometry used for the equations, (b) arc bend, (c) cosine S-bend and (d) sine S-bend. The geometrical parameters shown in (b)–(d) are the ones used by the software OlympIOs for the definition of the different bends.

$$x(z) = \frac{B}{2\pi}\left\{\cos\left(\frac{2\pi}{L}z\right) - 1\right\}. \tag{4.11}$$

And the arcs of the double-arc S-bend have a radius of:

$$R = \pm\frac{L^2}{4B}\left\{1 + \left(\frac{B^2}{L^2}\right)\right\}. \tag{4.12}$$

The nominal angle of these S-shaped bends is defined as $\theta = \arctan(B/L)$.

Radiation losses in S-bends have been previously analyzed [105, 106], and the theoretical results as well as experimental data show that the cosine S-bend provides less loss compare to the double arc S-bend and the sine S-bend. However, there is another possible way to reduce bending loss of S-bends by introducing a waveguide offset, as shown in Fig. 4.14 [60, 107]. The offset is introduced at the interface between the straight and bent waveguides or at

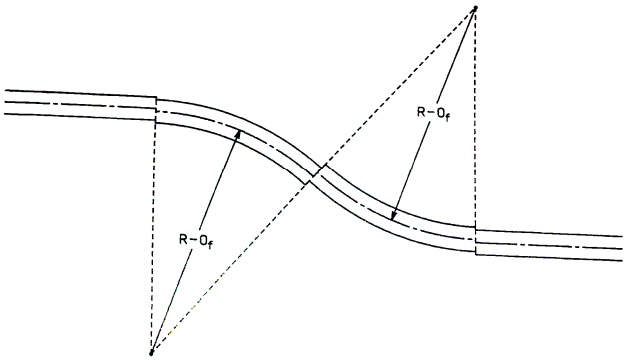

Figure 4.14: S-shaped bent waveguide with a waveguide offset [60].

interface between the two oppositely bent waveguides. The offset compensates for the field deformation experienced by the light in the bend and therefore alleviates the bend-induced radiation loss. BPM simulations can be used in order to design the proper offset. For simplicity, the approach adopted in this work is to use cosine S-bends on the construction of the different parts of the device, such as static phase delays and y-splitters, to be discussed next.

4.7 Power splitters

Means of splitting the optical power between different waveguides are necessary in the construction of an interferometer. The power splitters most commonly used in integrated photonics are the y-branches and multimode interference couplers.

4.7.1 Y-branches

A schematic representation of a single-mode branching waveguide used as a power divider/combiner is shown in Fig. 4.15 (a). At the branching point, the wavefront of the incident guided mode is slanted by the angle θ with respect to the wavefronts of the modes in the output branches. This angle is a key factor in determining the characteristics of the branching waveguide. As the full branching angle 2θ becomes larger, the field overlap between the input waveguide and the two output branches is reduced. Uncoupled optical power in

the two output branches leaks into the substrate. Hence, the guided mode suffers considerable scattering loss from optical branching. A tapered waveguide used in connection with the y-branch as shown in Fig. 4.15 (b) is necessary to suppress occurrence of the first-order lateral mode at the branching point [38].

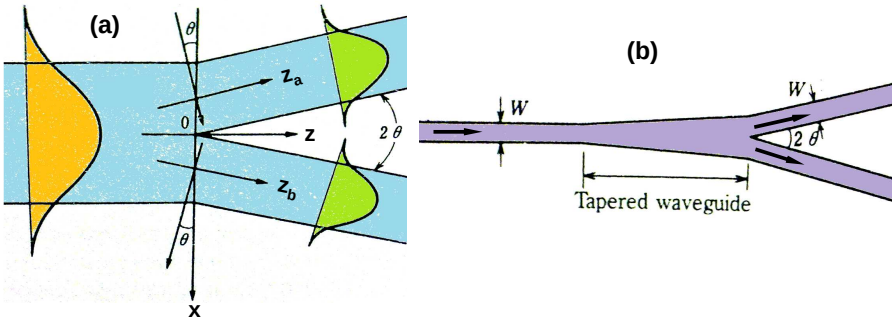

Figure 4.15: Single-mode branching waveguide structure: (a) analytical model, (b) with tapering structure.

The design of y-splitters is quite critical. It has been studied since the 1980s [108] up until nowadays [109], including studies for rib waveguides as well [110]. The shape of the S-bend used can also affect the performance of the splitter [111]. Fig. 4.16 shows the BPM calculation for a y-branch made of GaAs/AlGaAs waveguides, using a tapering section and cosine S-bends. It is possible to observe the symmetric distribution of the power between the two arms. More sophisticated designs can be used to further reduce losses and improve the power balance of the splitters [112, 113].

4.7.2 Multimode interference couplers

Multimode interference (MMI) couplers were first introduced by Bryngdahl [114], and have been widely used in the photonics industry since. They are based on self-imaging properties of multimode waveguides, by which an input field profile is reproduced in single or multiple images at periodic intervals along the propagation direction of the guide.

Fig. 4.17 (a) shows a schematic configuration of a MMI waveguide. The central structure of a MMI device is a waveguide designed to support a large number of modes. In order to launch light into and recover light from that

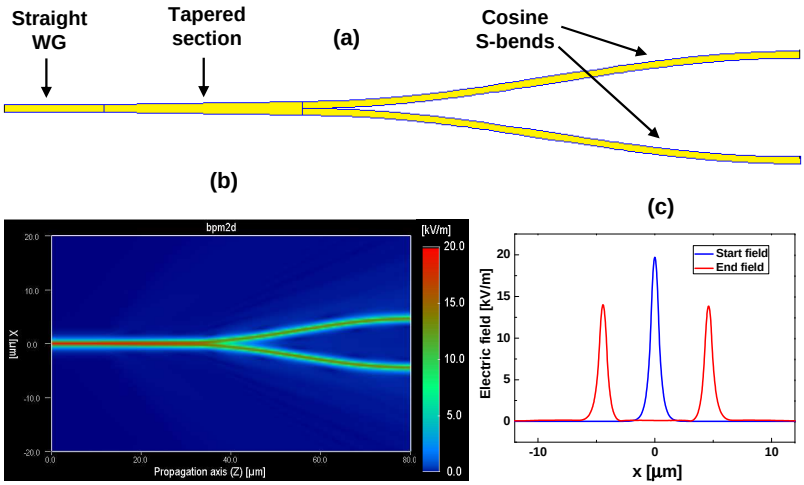

Figure 4.16: BPM simulation of Y-branch made of GaAs/AlGaAs waveguides: (a) Geometry showing the tapered section and the cosine S-bends, (b) Optical field intensity along the y-branch, (c) plot of the input and output fields.

multimode waveguide, a number of access (usually single-mode) waveguides are placed at its beginning and at its end. Such devices are generally referred to as $N \times M$ MMI couplers, where N and M are the number of input and output waveguides respectively. Here an analytical approximation is given for a 1 x N MMI, with the geometrical parameters shown in Fig. 4.17 (b).

Depending on the ratio of the MMI coupler length L to the square of the MMI coupler width W, and on the lateral positions of the input and output waveguides, different self-imaging arrangements are obtained. As the self-imaging depends on the interference of the different eigenmodes, the coupling length L_c, between the first two lowest order eigenmodes of the MMI coupler is used as a characteristic dimension [115]:

$$L_c \equiv \frac{\pi}{\beta_0 - \beta_1} = \frac{4}{3} n_{eff} \frac{W_{eq}^2}{\lambda_0}, \tag{4.13}$$

with β_0 and β_1 corresponding to the propagation constants of the first two modes and n_{eff} is the effective index of the central slab section of the MMI coupler. The last part of the equation can be considered as a definition of the equivalent width W_{eq} of the MMI coupler. For strongly guiding structure,

$W_{eq} \cong W$. Self-images of equal intensities appear in an MMI coupler, whose length L is given by [115]

$$L_{1\times N} = \frac{3L_c}{4N} \cong \frac{n_{eff}}{N}\frac{W^2}{\lambda_0}, \tag{4.14}$$

for 1 x N MMI couplers. By using these expressions, an initial geometry for the MMI can be determined. Further improvements can be made on the design by means of numerical simulations. Fig. 4.18 shows an EME simulation for a 1×8 MMI, where it is possible to see the interference patterns of the optical field and the nearly symmetric output fields.

MMI splitters are very popular for SOI platform, since they can be made very compact due to the high index contrast, but they also be constructed in GaAs/AlGaAs platform [116]. They can be less sensitive to fabrication tolerances than the y-splitters [115], and designs for splitting the optical mode into odd number of arms can be easily made.

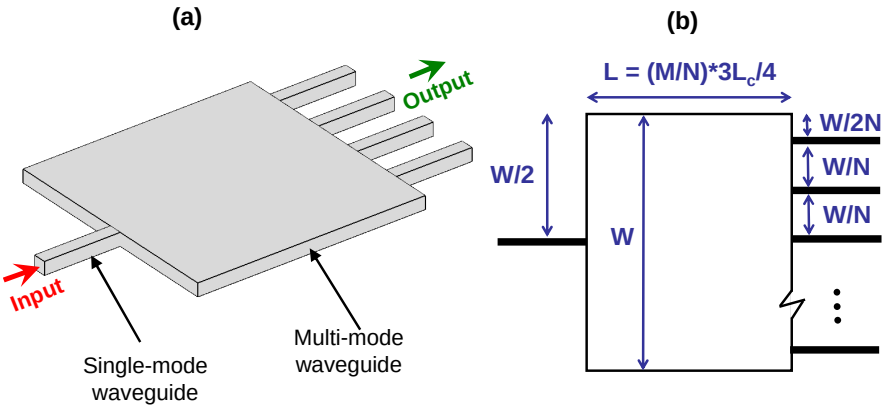

Figure 4.17: (a) Schematic configuration of a MMI coupler, (b) Geometrical design of symmetrical 1 x N MMI couplers.

It is also possible to obtain different relative phases for the different outputs of the MMI, for example by means of tapers [117], removing the need of extra phase delays and making a device more compact.

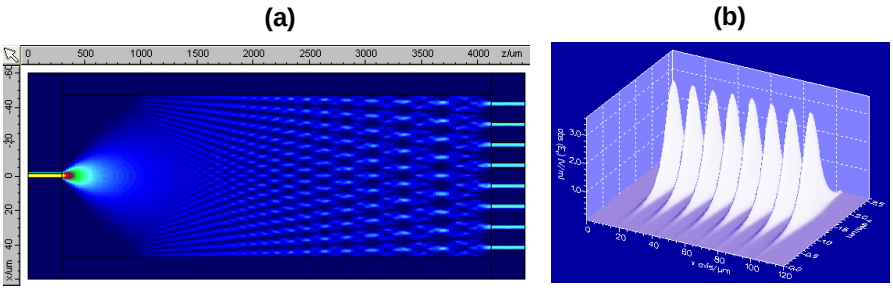

Figure 4.18: EME simulation of a MMI with one input and eight outputs: (a) Intensity profile of the MMI Coupler when the fundamental TE-like mode is launched at the input, (b) Electrical field profile at the output of the MMI Coupler.

4.8 Static phase delays

Differences in the length of the arms of a MZI allow to shape its transmission by destructive/constructive combination of the phases in the output. A simple way to elongate the arm length is by introducing two S-bends, as illustrated in Fig. 4.19 (a).

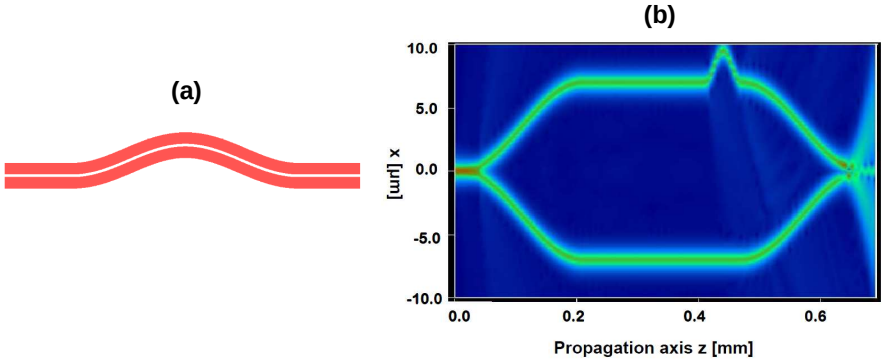

Figure 4.19: (a) Geometry of the phase delay built with cosine S-bends, (b) BPM simulation of a MZI with 2 arms, one of them having a π phase delay. The destructive interference in the output y-branch can be observed.

Depending on the shape of S-bend used, the total length introduced by it

will change. The length necessary for inducing the desired phase delay can be calculated by

$$\Delta\phi = \frac{2\pi \ n_{eff} \ \Delta z}{\lambda_0}. \tag{4.15}$$

where Δz is the total waveguide length introduced by the phase delay, and can be calculated according to the S-bend shape. Therefore the accuracy on the calculation of the effective index of the optical mode will also affect the design of the delays.

4.9 Coupling between waveguides

If two waveguides are placed sufficiently close so that their optical fields overlap, such as shown in Fig. 4.20, light can be coupled from one into the other. Optical power can be transferred between the waveguides, an effect that can be used to make optical couplers and switches. In some applications, the coupling can also be undesired. A short discussion on the properties of the coupling follows.

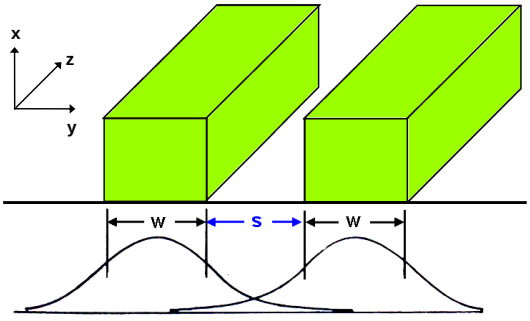

Figure 4.20: Representation of two channel waveguides spaced by a distance s, showing the overlap between their electric field distributions.

4.9.1 Directional couplers

The dual-channel directional coupler consists basically of parallel channel optical waveguides sufficiently closely spaced so that the energy is transferred from one to the other by optical tunneling. This energy is transferred by a process of

synchronous coherent coupling between the overlapping evanescent tails of the modes guided in each waveguide. The fraction of power coupled per unit length is determined by the overlap of the modes in the separate channels. Thus, it depends on the separation distance s and the interaction length L, both defined in Fig. 4.21 (a), and on the mode penetration into the space between channels [7]. The power is transferred back and forth between the two waveguides as a function of length, as it can be observed in Fig 4.21 (b)[118], where the fields in both waveguides are plotted at different propagation distances. The phase in the driven waveguide always lags 90° behind the other guide. That lagging phase relationship continues for increasing z, so that at the distance L all the power has been transferred to the other waveguide. L is defined as the *coupling length*, where 100% of the power is transferred if the two waveguides are identical. A concise theory of operation of the dual-channel directional coupler can be developed by following the coupled mode theory approach of Yariv [119], but that is beyond the scope of this work.

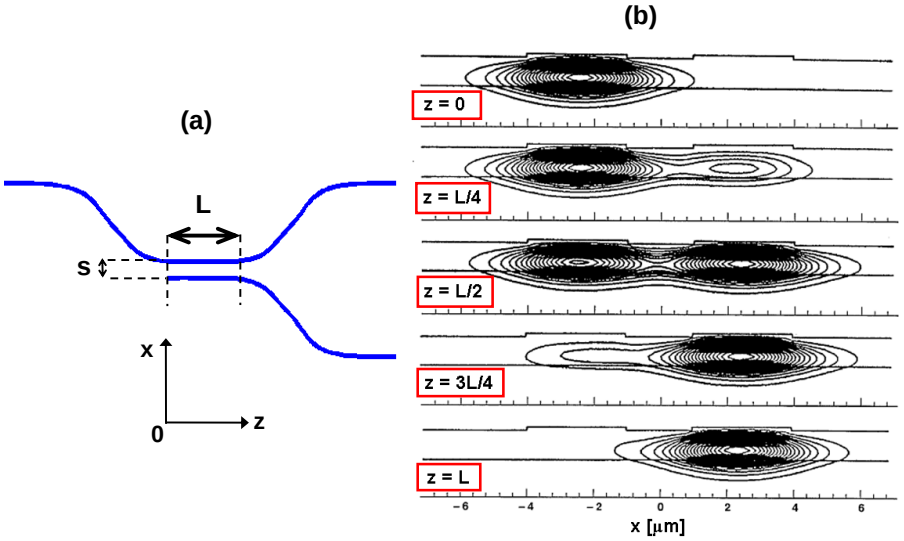

Figure 4.21: (a) Geometry of optical directional coupler with cosine S-bends in the input and output waveguides and (b) Energy transfer between two rib waveguides at different propagation distances. Distances are measured in coupling lengths L [118].

Directional couplers are very important components in the fabrication of various optical devices, such as Mach-Zehnder interferometers and ring resonators, as shown in Fig. 5.4. They can be used to replace y-branches, in special for applications where unequal power splitting into two outputs is required [120].

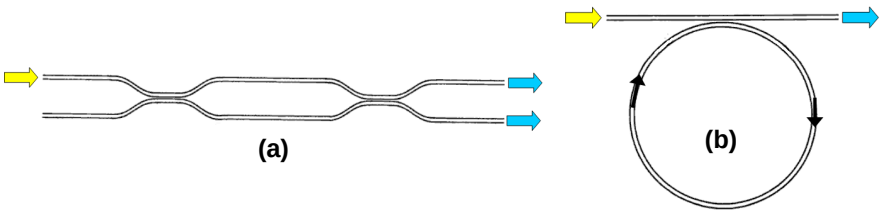

Figure 4.22: Optical waveguide devices using directional couplers: (a) Mach-Zehnder interferometer, (b) Optical ring resonator.

4.9.2 Channel spacing

Concerning the design of ultrasonic-photonic devices, there are two main factors involved with the choice of the spacing between the arms of the interferometers: the evanescent coupling between adjacent waveguides, as just described, and the dynamic phase modulation induced by the SAW.

Modes in adjacent waveguides can be coupled by their evanescent fields, which extend, into the region between them. Hence the extension of the mode in the waveguide must be analyzed priorly to the design of the device, so that the spacing between the waveguides of the device does not induce unwanted coupling. In the case of the rib waveguides, the intervening slab region will decrease the decay coefficient of the evanescent fields. Thus the coupling between rib waveguides will be larger than for similar guides without this region, such as the ridge waveguides [6].

There are other approaches on avoiding the coupling between the waveguides that allow to reduce the dimensions of the device, for instance by means of etching grooves in between the waveguides, as shown in Fig. 4.23 [121]. It has been found that etching a groove of a finite depth in the space between interacting waveguides can inhibit the exchange of power between them. The

particular advantages of the etched groove are compactness and low power loss. The cost is the added complexity in the fabrication process.

Moreover, the interferometers designed for SAW modulation have requirements on the spacing between the arms related to the relative phase modulation induced by the SAW, which is directly related to the acoustic wavelength. Thus, the knowledge of the correct acoustic wavelength is very important for the design of the device. A detailed numerical study on this issue can be found in [122].

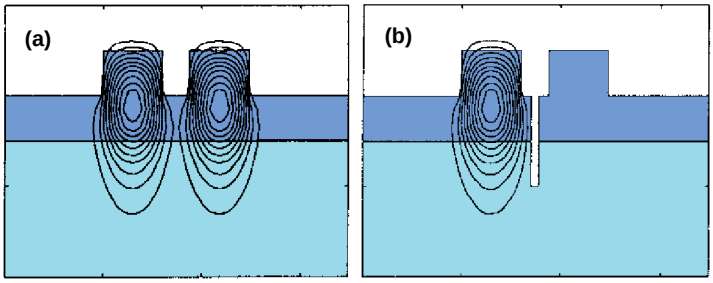

Figure 4.23: (Field contours showing the power exchange between the two adjacent rib waveguides in the (a) absence and (b) presence of an etched groove, at the same propagation distance [121].

Chapter 5

Fabrication and Characterization

This chapter describes the fabrication processes and characterization methods used to fabricate and measure integrated ultrasonic-photonic devices. Three material platforms were investigated: GaAs/AlGaAs, Silicon-on-insulator and GaN/sapphire. Comparisons are made with the numerical modeling and with other literature results.

5.1 Characterization

5.1.1 Acoustic excitation

IDTs characteristics are mostly determined by the finger geometry in the period, the number of finger pairs and the substrate material. The substrate material dependence is a very complex function of the electric field distribution and substrate orientation. However, it is possible to estimate many SAW properties by means of equivalent electrical values.

For RF circuit analysis, the scattering coefficient approach is widely used. The network analyzer, instrument commonly used for IDT characterization, measures the scattering coefficients of the device connected to transmission lines with a specific impedance of 50 Ω. Considering the case illustrated in Fig. 5.1, where the signal a_i is incident to and b_i is reflected from the circuit, if the

Figure 5.1: Incidence to and reflection from a linear circuit.

circuit is linear, b_i can be expressed as a linear combination of a_i:

$$\begin{pmatrix} b_1 \\ b_2 \end{pmatrix} = \begin{pmatrix} S_{11} & S_{12} \\ S_{21} & S_{22} \end{pmatrix} \begin{pmatrix} a_1 \\ a_2 \end{pmatrix} \tag{5.1}$$

where the matrix elements S_{ij} are the scattering coefficients. Note that a_i and b_i are normalized, so that their square corresponds to their power. For their units, dBm is used, and 0 dBm corresponds to $|a_i|^2$ of 1 mW. S_{11} and S_{22} are often referred to as reflection coefficients, while S_{12} and S_{21} are called transmission coefficients.

If one measures the S_{11} response of an IDT using a Network Analyzer, the curve will have a similar shape as plotted in Fig. 5.2. In the figure, G_R, which is almost independent of frequency, is due to electrode resistivity. The G_S strong peak is due to SAW radiation, and G_B is due to BAW radiation. These parameters can be used to characterize the performance of the fabricated IDTs.

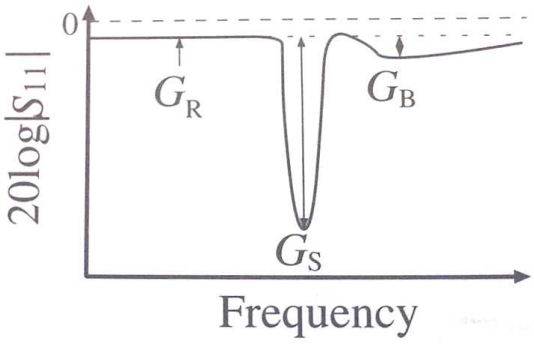

Figure 5.2: Schematic return loss characteristics of the IDT [36].

5.1.2 Device characterization

To characterize the samples, the setup schematized in Fig. 5.3 was used. The optical part is composed of a tunable laser source (TLS) with a range from 1480 to 1580 nm. The light from the TLS passes through a polarization control, and is coupled to the sample by means of a tapered and lensed single mode fiber. The same kind of fiber is used to couple light from the output of the sample directly to an optical spectrum analyzer (OSA).

The RF part of the setup is composed of a probe station, with high frequency RF probes which are used to deliver voltage to the IDTs, a low noise photodetector, a Lock-in amplifier, a multimeter, a RF spectrum analyzer and an oscilloscope. By plugging the output fiber into the photodetector and obtaining the electrical response, one can make use of the RF instruments to obtain the desired data, such as AC response, DC response, modulation spectrum, modulation amplitudes, etc. The measurements are performed at room temperature.

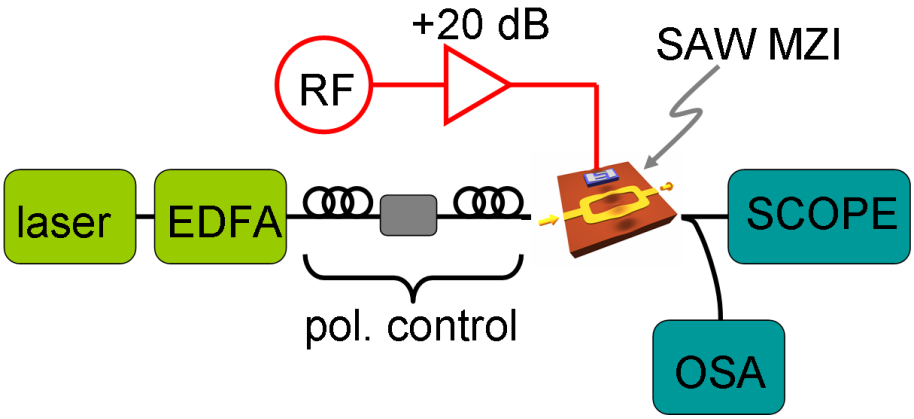

Figure 5.3: Schematic representation of the characterization setup for the ultrasonic-photonic devices.

5.2 Introduction on Fabrication

The largest part of the fabrication processes here described took place at the cleanroom facilities at Danchip, which is a national center located at and fully owned by the Technical University of Denmark (DTU). Therefore the processes described in this chapter will be based on the machines that were available there.

Before describing the actual processes used to make the samples, a short introduction on the main fabrication steps follows. Most micro/nanofabrication techniques have a few basic steps in common: lithography, thin film deposition and etching [123].

5.2.1 Lithography

Lithography is the technique used to transfer a computer generated pattern (lithographic mask) onto a substrate. This pattern is then used to etch an underlying thin film (etching mask) such as an oxide or nitride. Photolithography, which is lithography using a UV light source, is the most common lithography technique in microelectronic fabrication, due to its advantages in terms of large scale production. Other two important lithography techniques are electron-beam (e-beam) and X-ray lithography. E-beam lithography is the technique adopted to fabricate the samples presented here.

The development of e-beam lithography tools started in the late 1960s [124] by modifying the design of scanning electron microscopes (SEMs). The working principle of the e-beam lithography is relatively simple and very similar to photolithography: a focused beam of electrons is scanned across a substrate covered by an electron-sensitive material (resist) that changes its solubility properties according to the energy deposited by the electron beam. Areas exposed, or not exposed according to the tone of the resist, are removed by developing. The resolution limits of e-beam lithography can be pushed to below 10 nm [125].

E-beam resist

E-beam resists are usually polymers. A chemical or physical change is induced in the resist by irradiation, and this change allows the resist to be patterned.

For a positive e-beam resist, the polymer-electron interaction causes chemical bonds to be broken to form shorter molecular fragments. As a result, the molecular weight is reduced in the irradiated area, which can be dissolved subsequently in a developer solution that attacks the low-molecular weight material. Common positive e-beam resists include PMMA and ZEP520A. For negative e-beam resist, the irradiation causes radiation-induced polymer linking. The cross linking creates a complex 3D structure with a molecular weight higher than that of the non-irradiated polymer. The non-irradiated resist can be dissolved in a developer solution that does not attach the high-molecular-weight material. HSQ is a commonly used negative e-beam resist.

Proximity effects

In optical lithography, the resolution is limited by diffraction of light. In e-beam lithography, the resolution is not limited by diffraction (because the wavelengths associated with electrons of a few keV and higher energies are less than 0.1 nm) but by the electron scattering. When electrons penetrate the resist film and underlying substrate, they undergo collisions. These collisions lead to energy losses and path changes. Thus, the incident electrons spread out as they travel through the material until either all of their energy is lost, or they leave the material because of backscattering. By means of backscattering, electrons effectively can irradiate several micrometers away from the center of the exposure beam. Since the dose of a resist is given by the sum of the irradiations from all surrounding areas, electron beam irradiation at one location will affect the irradiation in neighboring locations. This phenomenon is called the proximity effect [64]. The proximity effect places a limit on the minimum spacings between pattern features. To correct for the proximity effect, patterns are divided into smaller segments. The incident electron dose in each segment is adjusted so that the integrated dose from all its neighboring segments is the correct exposure dose.

5.2.2 Thin film deposition

Thin film deposition is used extensively in micro/nanofabrication technologies, for many different applications, including electrical isolation/connection, mask for etching and doping, passivation, among others. Most of the thin films

deposited have different properties to those of their corresponding bulk forms. The techniques used on thin film deposition can have a great impact on the final properties of the film, for example, the internal stress (compressive or tensile) is extremely process-dependent. Adhesion is another important issue that needs to be taken into account when depositing thin films.

The deposition can be chemical or physical. In the case of the glasses and nitrides used as etch-masks here, the deposition process is chemical. Plasma is used as a precursor of chemical reactions in the gas phase to form the deposited film (plasma-enhanced chemical vapor deposition). In the case of the ZnO deposition, the process used here is physical. The film was formed by sputtering. In this process, usually a plasma of a noble gas, such as argon, is used to knock material from a "target" a few atoms at a time and sputter it on the sample. The e-beam resist films are deposited through spin coating, which is done by covering the sample with resist and rotating it. The thickness of the film can be controlled by changing the rotation speed and acceleration.

5.2.3 Etching

Etching is a fabrication step of fundamental importance, since it is the process that will form the photonic micro/nanostructures on the substrate. The removal of material from a substrate by chemical reaction or by ion bombardment is referred to as an etch process. The material that is not masked is removed, resulting in patterned regions. The rate of material removal is known as *etch rate*, and corresponds to the thickness removed per unit time (nm/min). Depending on the etch process and material, the etching can occur in both horizontal and vertical directions. The lateral etch ratio R_L is given by

$$R_L = \frac{\text{Horizontal etch rate}(r_H)}{\text{Vertical etch rate}(r_V)}. \tag{5.2}$$

For $R_L = 1$ the etching is isotropic, for $0 < R_L < 1$ the etching is anisotropic, and for $R_L = 0$ the etching is called directional. Illustrations of the different etching directionalities are shown in Fig. 5.4.

Typically, the masking material as well as the substrate are also attacked by the etch process. The ratio of etch rates of different materials is called the *selectivity* of an etch process, and is illustrated in Fig. 5.5.

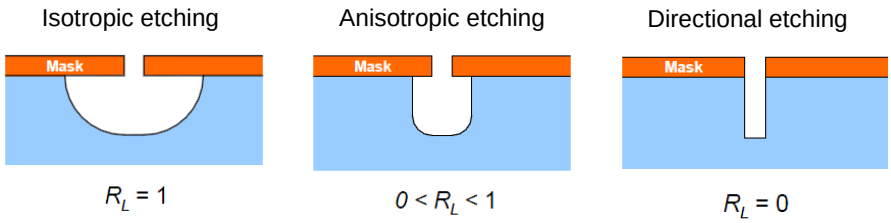

Figure 5.4: Illustration of the different etching directionalities for different values of lateral etch ratio.

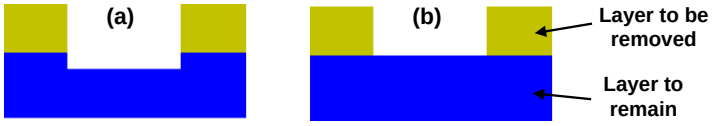

Figure 5.5: Illustration of the etching selectivity. (a) Poorly selective etch: removes the top layer, but also attacks the underlying material. (b) Highly selective etch: leaves the underlying material unharmed.

There are two types of etching mechanisms - wet and dry etches, illustrated in Fig. 5.6. Wet etching uses liquid etchants to remove material, while the dry etching uses plasma. Wet chemical etch processes are typically isotropic and can be very selective, while dry etch techniques can be highly anisotropic but usually have low selectivity.

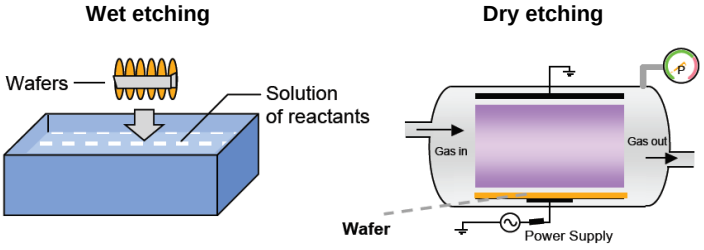

Figure 5.6: Illustration of the wet and dry etching processes.

Wet chemical etching

Wet chemical etching is used extensively in semiconductor processing. Chemical etchants are used for example for lapping and polishing to give an optically flat, damage-free surface. Prior to thermal oxidation or epitaxial growth, semiconductor wafers are chemically cleaned to remove contamination that results from handling and storing. The mechanisms for wet chemical etching involve three essential steps: the reactants are transported by diffusion to the reacting surface, chemical reactions occur at the surface, and the products from the surface are removed by diffusion. Both agitation and temperature of the etchant solution influence the etch rate. The major disadvantage of wet chemical etching in pattern transfer is the undercutting of the layer underneath the mask, resulting in a loss of resolution in the etched pattern. To achieve a high-fidelity transfer of the resist patterns required for ultralarge-scale integration processing, dry etching methods have been developed. Wet etching has only been used here for cleaning purposes and for the removal of etch-masks. For example, HF is used for removing the SiO_2 etch mask.

Dry etching

Dry etching is synonymous with plasma-assisted etching, which denotes several techniques that use plasma in the form of low-pressure discharges. Dry etch methods include plasma etching, reactive ion etching, sputter etching, among others. For the photonic structures patterning, dry etching is used here, in special the technique called reactive ion etching (RIE). It is a combination of physical and chemical processes. Inert gases – reactive gases containing fluorine, chlorine, bromine, or oxygen – are used. Ions are accelerated and their role can be to make the surface more reactive (by slight damage of the surface) or to supply additional energy for etch products to desorb from the surface. As the gas phase can react more readily and form volatile etch products, the etch rate increases. Two special cases are the deep-RIE (DRIE), capable of achieving very high aspect ratios and etching rates, and the inductively coupled plasma (ICP) RIE, where very high density plasma densities can be achieved.

The different etching machines used in the fabrication processes for this work are presented in Fig. 5.7. The III-V ICP machine shown in (c) was only made available during the last months of this project.

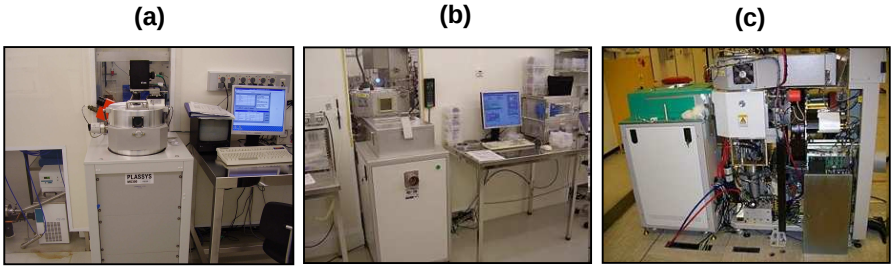

Figure 5.7: Picture of the etching machines used in the different fabrication processes: (a) Plassys - III-V RIE, (b) STS Advanced Silicon Etcher - ICP-DRIE, (c) SPTS III-V ICP-RIE Etcher.

5.3 GaAs Devices

The substrates used for GaAs processing were either grown by metalorganic vapour phase epitaxy (MOVPE) at Danchip or by molecular beam epitaxy (MBE) at the Niels Bohr Institute (NBI) at the University of Copenhagen. Their epitaxial structure for the fabrication of rib waveguides devices is shown in Fig. 5.8. The structure contains a thin a stop-etch layer, with a concentration of aluminum of 30%, to avoid oxidation of the AlGaAs after the etching. The confinement layer has 70% of aluminum content. This number represents a compromise to obtain lowest possible refractive index while obtaining smooth and uniform layers during the growth. The fabrication process used to fabricate the GaAs devices is described in Fig. 5.9. The RIE machine used for the GaAs processing had the following gases available: CHF_3, CH_4, O_2 and H_2. The GaAs etch processes had been developed at DTU for etching of photonic crystal membranes, but hadn't been optimized for channel waveguides yet.

The process starts with the deposition of a glass etch-mask by Plasma Enhanced Chemical Vapor Deposition (PECVD). Then e-beam resist, in this case ZEP520A, is spun on the sample, and the waveguide patterns (trenches) are transferred onto the resist by means of e-beam lithography. The sample is developed, and after that it is put into the RIE machine, where the glass mask is etched by using a combination of CHF_3 and O_2. After the patterns have been transferred to the glass mask, the e-beam resist is removed. The sample is again placed into the RIE machine, now for the GaAs etching, by

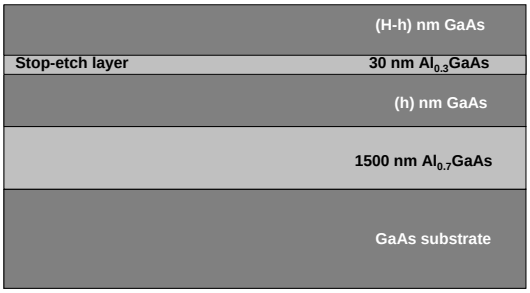

Figure 5.8: Epitaxial structure of the GaAs/AlGaAs wafers used on the fabrication of devices with rib waveguides.

using cyclic etch in a CH_4/H_2 plasma with O_2 cleaning steps in between [126]. The waveguide patterns have now been transferred to the GaAs layer. The glass mask is removed.

The second part, to fabricate the IDTs, starts by spinning the e-beam resist as before. Now the fingers of the transducers are defined by e-beam lithography, and once more the resist is developed. A thin layer of metal (aluminum or gold) is evaporated, and lift-off is performed, in order to create the IDTs. Lift-off refers to the process of creating patterns on the wafer surface through an additive process, as opposed to subtractive processes such as etching.

An important aspect in the e-beam lithography process is the proximity effect. Methods for proximity correction can be used with good results [127], as can be seen in Fig. 5.10. The darker (pink) areas are the trenches of the waveguides. It can be noticed that when placing large structures around the waveguide area, the waveguides collapse for the samples without proximity correction.

The GaAs fabrication process at DTU had been previously developed using Si_3N_4 as etching mask. Fig. 5.11 shows scanning electron microscope (SEM) pictures of the samples fabricated using this type of glass as mask.

The waveguides are relatively long (up to 3 mm), and a careful inspection throughout the length of the waveguides detected some defects. Some examples of these defects are shown in Fig. 5.12. If a piece of the waveguide is missing, no light can be guided to its output, what could also be noticed during the characterization of the samples. Several parameters of the process were ana-

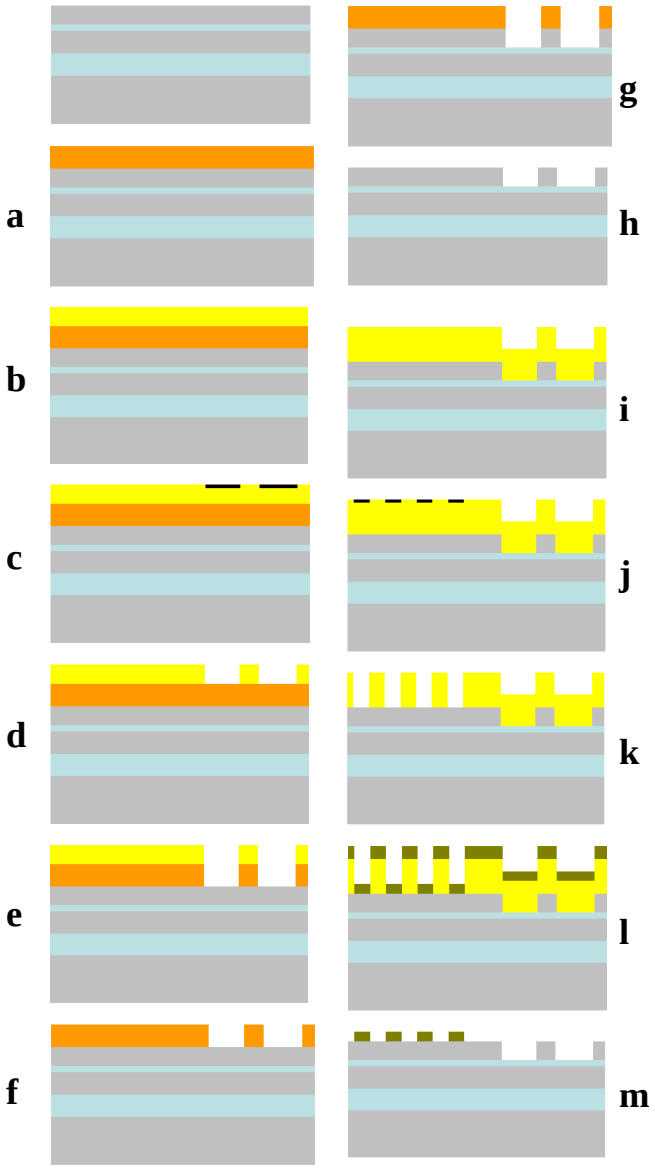

a) PECVD deposition of glass

b) Spinning of e-beam resist (ZEP520A)

c) E-beam patterning of the WG grooves

d) Resist development

e) RIE etching of glass mask

f) Removal of e-beam resist (wet chemistry and ultrasound bath)

g) RIE etching of GaAs

h) Removal of glass mask

i) Spinning of e-beam resist

j) E-beam patterning of the IDT fingers

k) Resist development

l) Metal evaporation

m) Lift-off

Figure 5.9: Representation of the fabrication steps in GaAs.

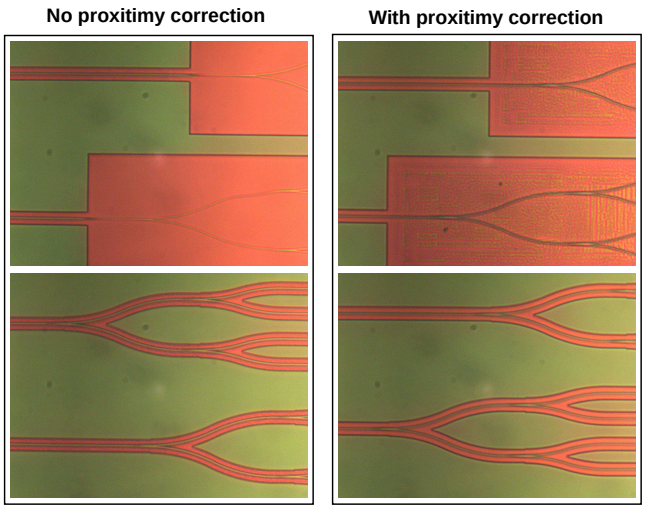

Figure 5.10: Pictures of GaAs patterns on e-beam resist after development for samples without (left) and with (right) proximity correction.

lyzed, and the conclusion was that the Si_3N_4 deposition was responsible for the waveguide breakage. Tensile stress on the Si_3N_4 film deposition [128] was probably causing the breakage.

To avoid this problem, the Si_3N_4 masks were replaced by SiO_2 ones. Fig. 5.13 shows SEM images of the SiO_2 mask after RIE etching.

The use of the SiO_2 mask solved the breakage problem. Pictures of the final samples are shown in 5.14.

To test the fabrication of the IDTs, a bare GaAs semi-insulating substrate was used, on which double-fingered IDTs with a width of 700 nm were deposited. The response of the planar and focused IDTs, measured with a Network Analyzer, is presented in Fig. 5.15 (b) and (c), respectively. The resonance frequency obtained is in very good agreement with the FEM calculations presented in Fig. 5.15 (a).

The fabricated waveguides were characterized, and the transmission curves are plotted in Fig. 5.16. The transmission obtained for the straight rib waveguides with geometry parameters $h = 200$ nm, $H = 500$ nm and $w = 700$ nm

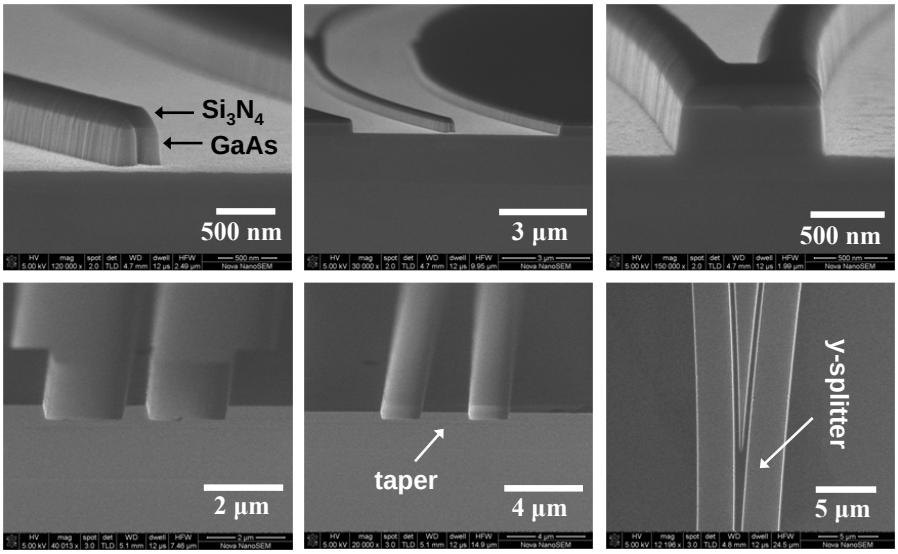

Figure 5.11: SEM pictures of GaAs devices fabricated with a Si_3N_4 etching mask. The darker top layer is the mask.

shows a strong wavelength dependence (∼6 dB variation over the 100 nm range measured), which could be numerically predicted by the dispersion and losses of the mode (dashed curve). The MZIs were designed to have a transmission dip at 1.55 μm, and the arrow in the figure points out the measured dip, which is very close to the one it was designed for.

Unfortunately the yield of simultaneously having good performance IDTs and waveguides on the same sample was so low that didn't make it possible to characterize the acousto-optic modulation of these devices. Improvements need still to be done on the fabrication process, but by better optimizing the etching process the yield could be increased. For example very high aspect ratio GaAs/AlGaAs waveguides with near-ideal vertical sidewalls can be produced by using chlorine-based ICP etching [129].

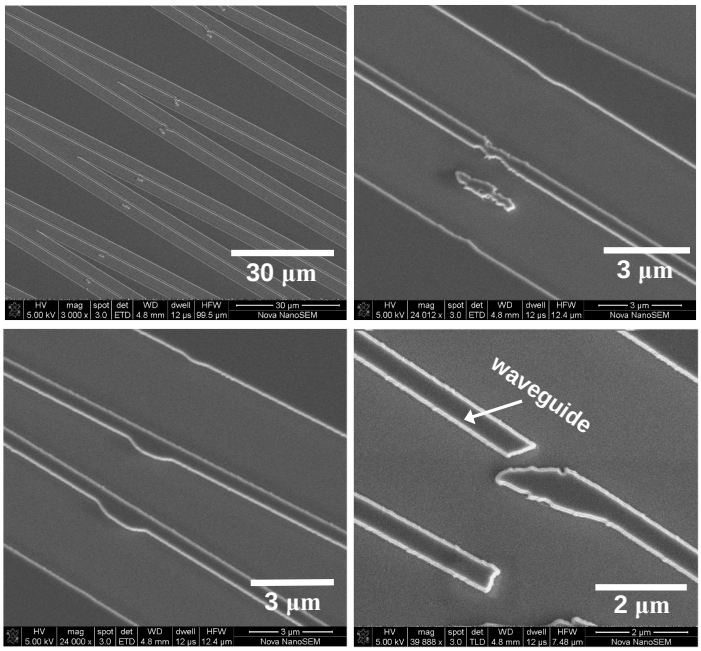

Figure 5.12: SEM pictures of GaAs devices (top view) fabricated with a Si_3N_4 etching mask. Regions were the waveguides are defective can be clearly seen.

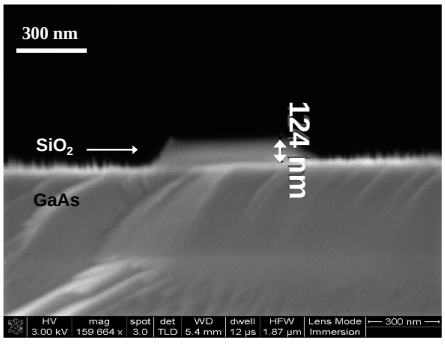

Figure 5.13: SEM pictures of SiO_2 mask after etching. The pictures are not so sharp due to charging effect on the insulator.

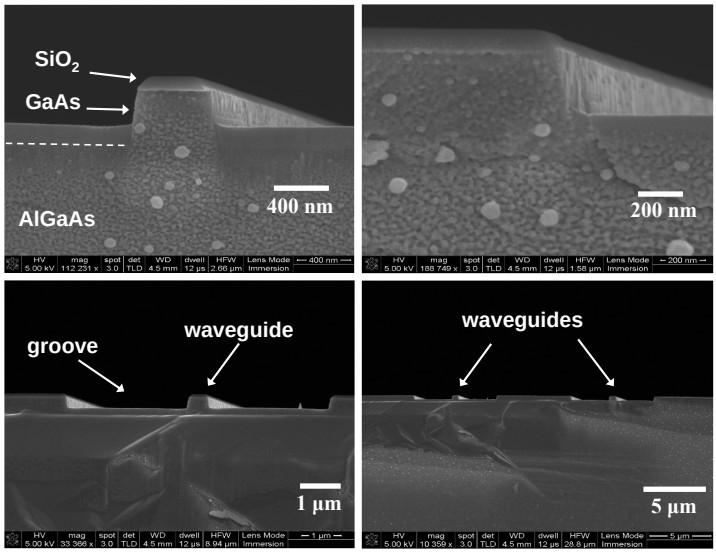

Figure 5.14: SEM pictures of GaAs rib waveguides fabricated using SiO_2 mask.

5.4 ZnO + SOI Devices

The substrates used for the fabrication of the SOI devices were standard wafers with 340 nm of top silicon and 1000 nm insulating layer produced via Smart Cut technology by Soitec [130]. The processing of SOI wafers was much simpler than for the GaAs case. The machine available for the etching process was a ICP-DRIE, which can produce very straight and smooth sidewalls. The gases used for the silicon etching were SF_6 and O_2 alternated with a passivation phase with C_4F_8. The deposition of ZnO thin films was performed at the Paul Drude Institute in Berlin. The fabrication of the photonic components is very similar to the GaAs process, and the steps are described in Fig. 5.17.

The fabricated devices had dimensions very close to the ones they were designed for, and the quality was also very good, with very smooth sidewalls, as can be seen in Fig. 5.18.

The first approach of first fabricating the optical structures and then depositing ZnO over the whole surface wasn't very successful. The sputtering of the ZnO thin films is very sensitive to discontinuities on the surface, what led to a very furry surface on the waveguide region, as shown in Fig. 5.19.

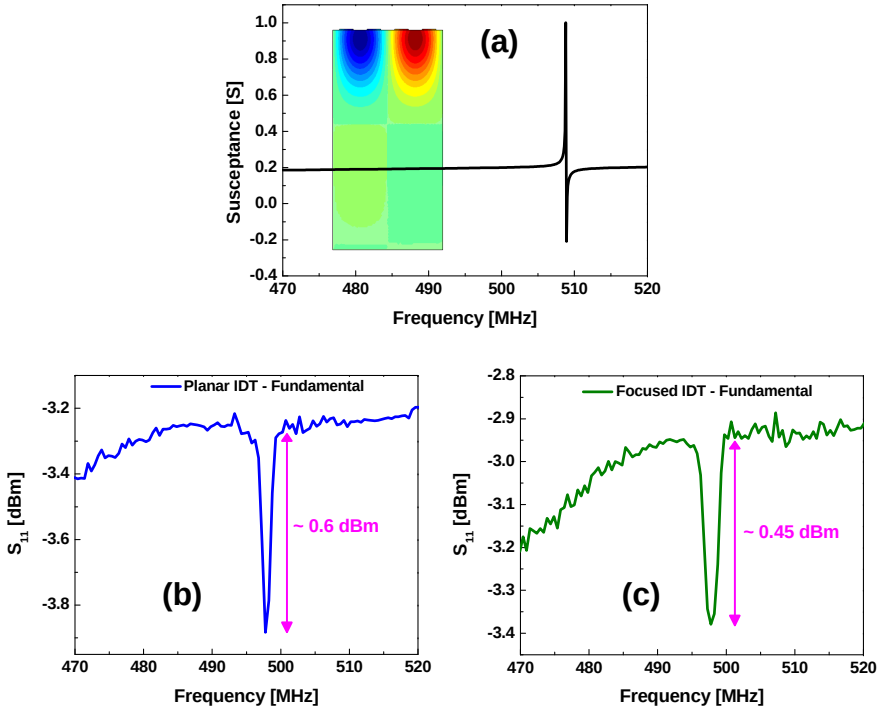

Figure 5.15: Characterization of IDTs fabricated in GaAs semi-insulating substrate: (a) FEM calculation of the acoustic susceptance (inset shows the vertical displacement), (b) measured S_{11} response of planar IDT, (c) measured S_{11} response of focused IDT. A good agreement between calculation and measurement of the resonance frequency can be observed.

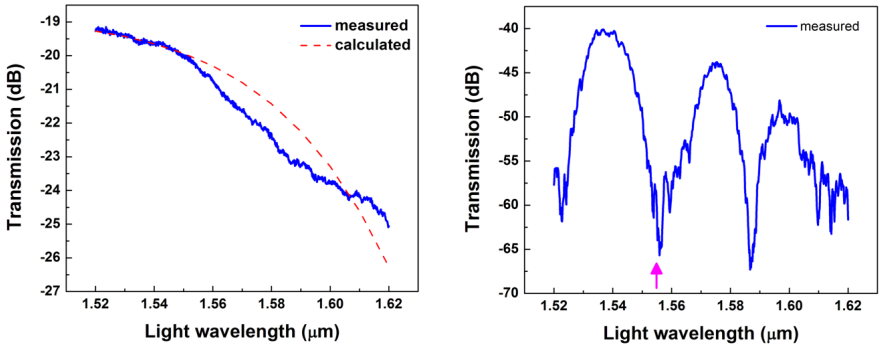

Figure 5.16: Optical transmission of the devices fabricated in GaAs: (a) straight rib waveguide (the dotted line shows the transmission calculated including propagation losses and dispersion), (b) MZI with 2 asymmetric arms, with transmission dip designed at 1.55μm.

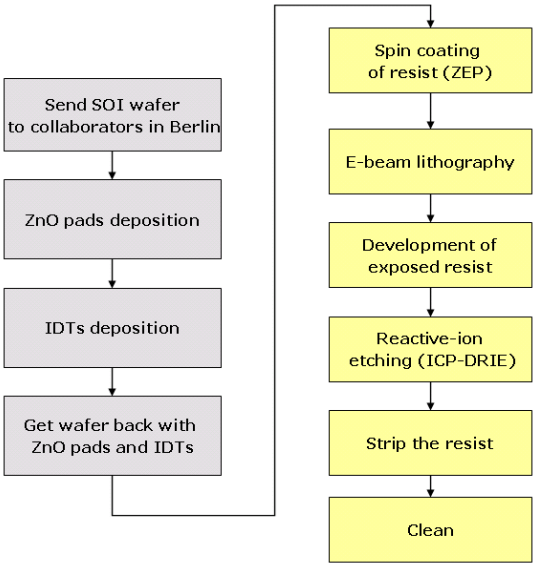

Figure 5.17: Steps of the fabrication process for the SOI samples with ZnO pads.

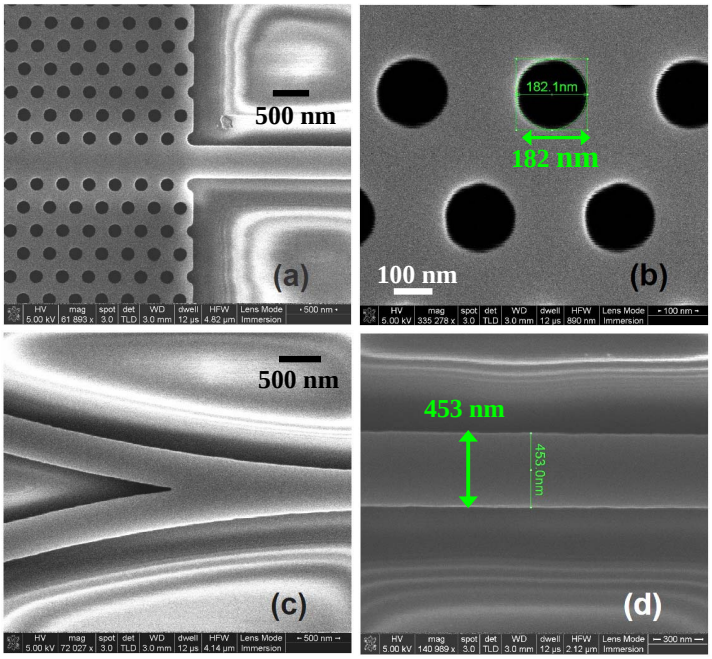

Figure 5.18: SEM images of the photonic components of the SOI samples: (a) PhC waveguide and coupling ridge waveguide, (b) close-up of the PhC holes, the designed diameter was 180 nm, (c) y-splitter of a MZI, (d) ridge waveguide, the designed width was 450 nm.

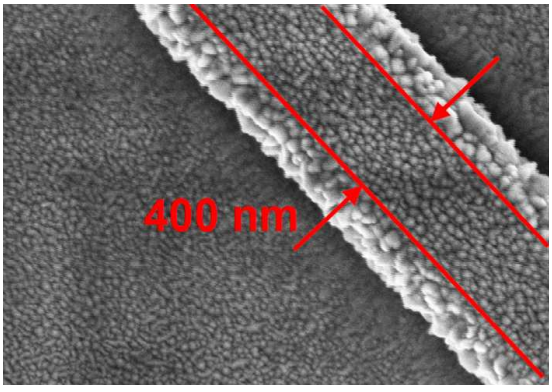

Figure 5.19: SEM picture of ZnO deposition on top of a ridge waveguide fabricated on a SOI wafer.

Since no facilities for glass planarization were readily available, the ZnO pads configuration described in Chapter 3 was used. The pads were placed for acoustic excitation only in the IDTs regions, as can be seen as the light grey areas in Fig. 5.20.

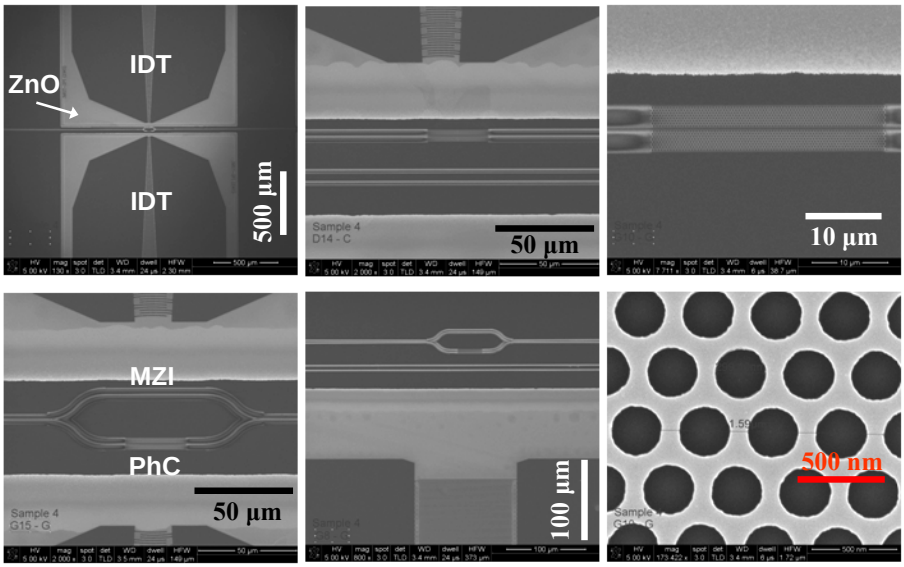

Figure 5.20: SEM picture of fabricated SOI samples with the ZnO pads and IDTs, together with the photonic components.

The samples were characterized optically and, as expected from the SEM images, the responses were very good. Fig. 5.21 shows (a) numerical simulation (FDTD) and (b) the experimental result of the optical transmission of a PhC waveguide. The PhC waveguide was designed to have a transmission band edge near 1550 nm. The fabricated sample shows a transmission curve very similar to the simulated one, with the band edge shifted to 1530 nm, due to small deviations in the diameter of the holes, which can be calibrated. The optical coupling efficiency can be improved by optimizing the design, for instance with the use of tapers [131]. Fig. 5.22 (a) shows the transmission curve obtained for an asymmetric MZI with 2 arms. The dips in transmission caused by interference are about 20 dB deep, what is within the standard values obtained for good fabrication processes [132]. Fig. 5.22 (b) shows the transmission curve

obtained for an asymmetric MZI with 2 arms, now with a PhC waveguide fabricated in one of the arms. The combination of the interferometer and PhC effects can be observed, with a reduction in transmission around 1550 nm.

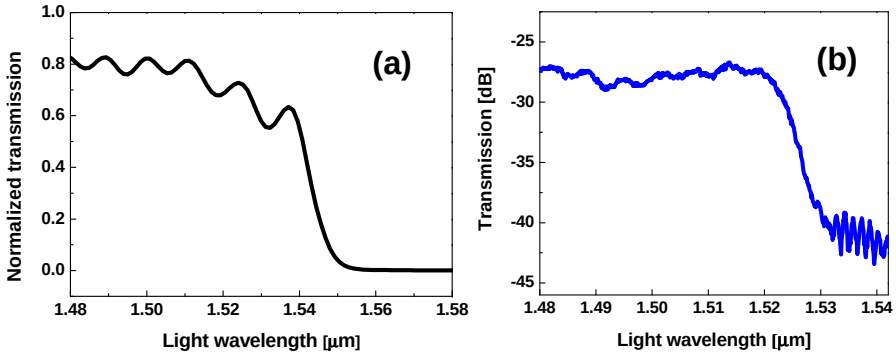

Figure 5.21: W1 photonic crystal waveguide in SOI: (a) FDTD calculation, (b) transmission measurement.

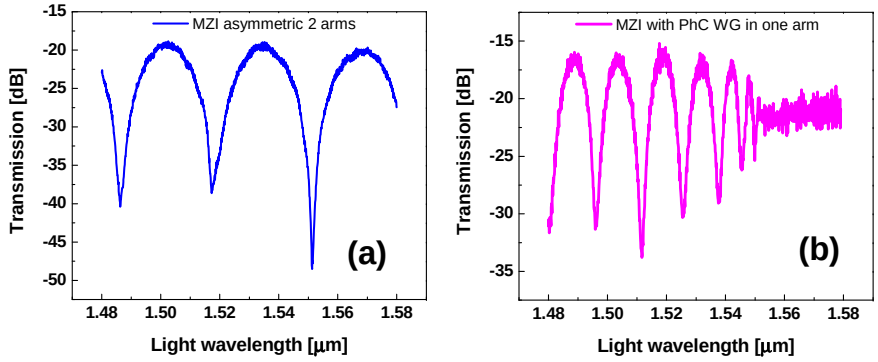

Figure 5.22: Transmission measurements of (a) SOI asymmetric MZI with 2 arms and (b) SOI MZI with a section of PhC waveguide in one of the arms.

The IDTs deposited on ZnO were also characterized, and in this case presented strong resonance for two cases: for the fundamental component of the Rayleigh mode and for a leaky-SAW mode. The numerical results for the Rayleigh and Leaky-SAW modes are shown in Figs. 5.23 (a) and (b), respec-

tively, while the experimental results for the corresponding modes are presented in (c) and (d). A fairly good agreement between the modeled and fabricated IDTs can be observed.

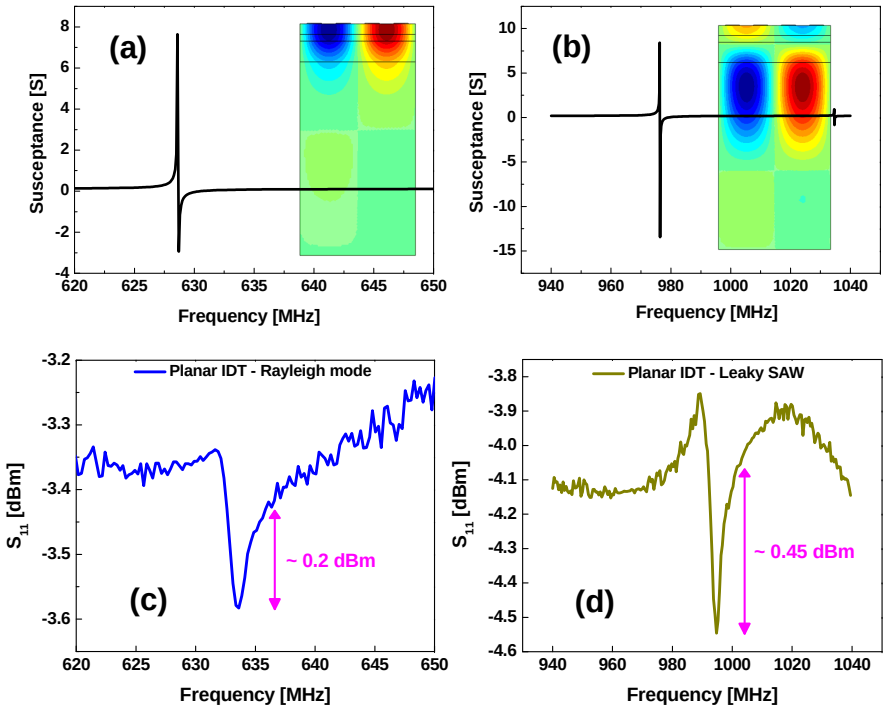

Figure 5.23: IDTs fabricated in SOI wafer with ZnO thin film: (a) and (b) are FEM calculations of the susceptance of the Rayleigh and Leaky-SAW modes, respectively. The inset shows the u_x distribution of the modes; (c) and (d) are the experimental S_{11} response of the respective modes. A fairly good agreement between the calculated and measured resonance frequencies can be observed.

The ZnO pads configuration leads to very weak acousto-optic modulation, as demonstrated in [133] and as validated by the numerical results presented in Chapter 3. A more efficient alternative would be to use a planarization layer, which is, according to the modeling results presented here, the most promising approach for integrating ultrasonic-photonic devices on silicon platform. As mentioned before, unfortunately no facilities to fabricate this kind of device were available.

5.5 GaN Devices

On search for an inherently piezoelectric platform material with higher refractive index contrast than GaAs, GaN/sapphire was chosen as material platform. Some initial fabrication steps were pursued. For the fabrication of the GaN devices, a ICP-RIE machine was available. The gases used for the GaN etching were Cl_2 and Ar. The wafers were composed of 2 μm of GaN on sapphire substrate. A few tests on the etching process were realized, and the preliminary results on mesas etching and waveguides etching can be seen in Figs. 5.24 and 5.25, respectively. Si_3N_4 was used as the etch-mask, and it was previously etched using the same RIE machine used on the GaAs process. It was possible to obtain very deep etches ($\sim$1 μm), with good verticality of the sidewalls. The smoothness of the sidewalls can be improved by using a different material as etch-mask.

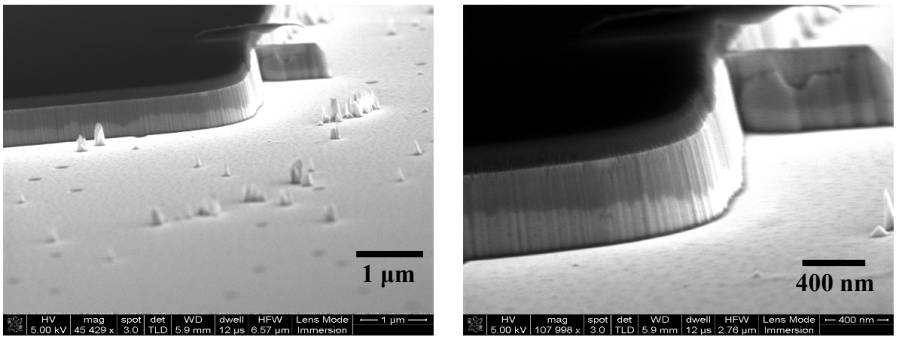

Figure 5.24: SEM pictures of deep ICP etching of mesas in GaN. The darker layer on top is the Si_3N_4 mask used for the etching.

IDTs with the same geometry used in the GaAs process were deposited on the GaN wafers to test the acoustic excitation. Three strong acoustic resonances were found. Fig. 5.26 (a) shows the numerical calculations for the fundamental Rayleigh mode, while (b) and (c) show the experimental results for the planar and focused IDTs, respectively, for the same mode. A response with about the same intensity as for the GaAs wafers was obtained at the fundamental resonance frequency. It was also possible to detect the responses of two other higher order modes of the SAW, shown in Figs. 5.27 (b) and (c). The

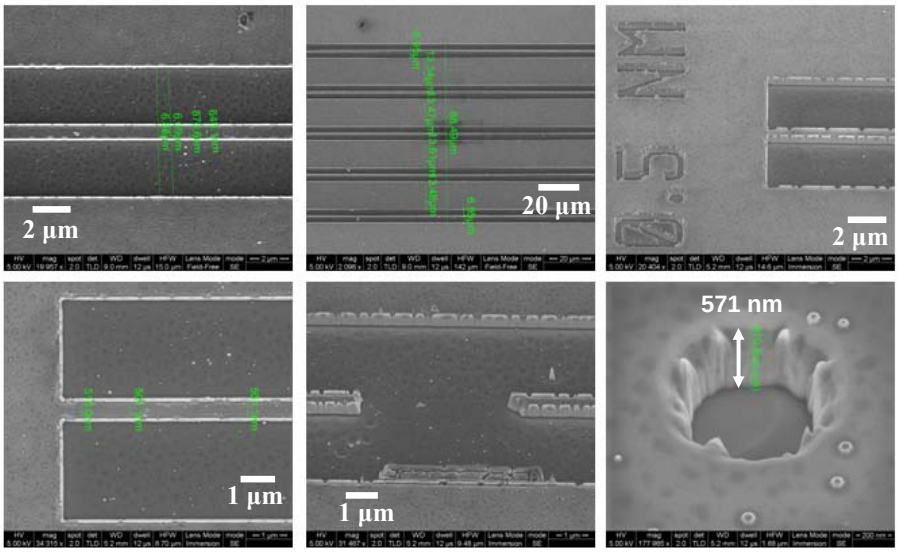

Figure 5.25: SEM pictures of etching test of GaN straight waveguides.The glass etching mask had not been removed.

numerical calculations for the higher order modes is presented in Fig. 5.27 (a), where the strongest resonances in the frequency range between 1700 and 2100 MHz are shown, as an attempt to identify the modes measured experimentally. Variations in the thickness of the GaN layer can shift the resonance frequency, making it more challenging to identify the correspondent modes. The acoustic mode experimentally observed at around 1757 MHz can be probably a Leaky-SAW or a Sezawa mode [134], while the mode at 2112 MHz is probably the third harmonic of the Rayleigh mode. In any case, it has been demonstrated that an excitation up to 2 GHz can be reached by using easily manufacturable 700 nm-wide IDT fingers. These preliminary results indicate that GaN is a very promising material for the fabrication of integrated ultrasonic-photonic devices, possessing a good refractive index contrast and also allowing for the excitation of very high frequency SAWs.

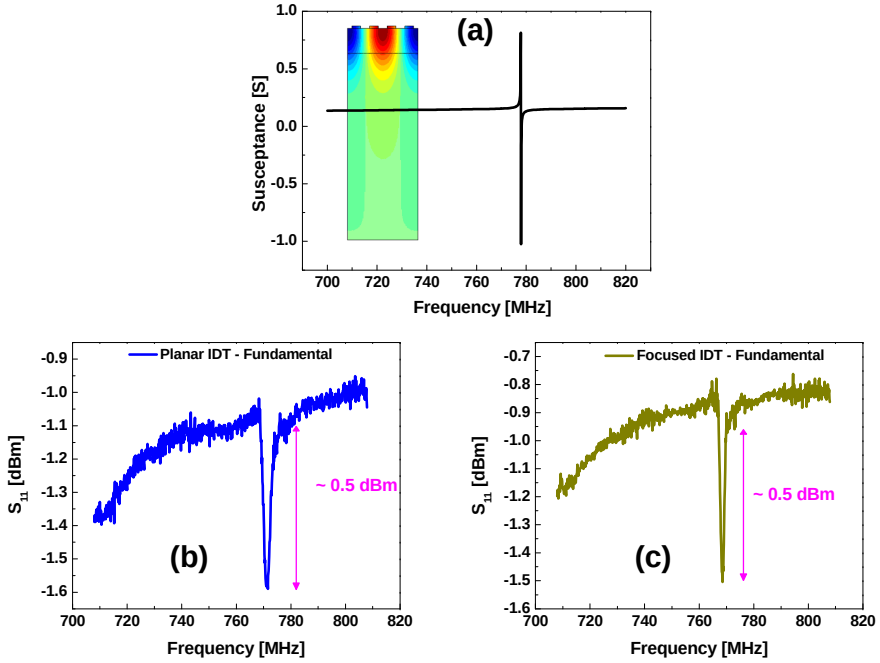

Figure 5.26: Characterization of IDTs fabricated in GaN deposited on sapphire substrate: (a) FEM calculation of the susceptance of the fundamental Rayleigh mode (inset shows the vertical displacement distribution of the mode); (b) and (c) show the experimental S_{11} response of the planar and focused IDTs, respectively. A good agreement between the calculated and measured resonance frequencies can be observed.

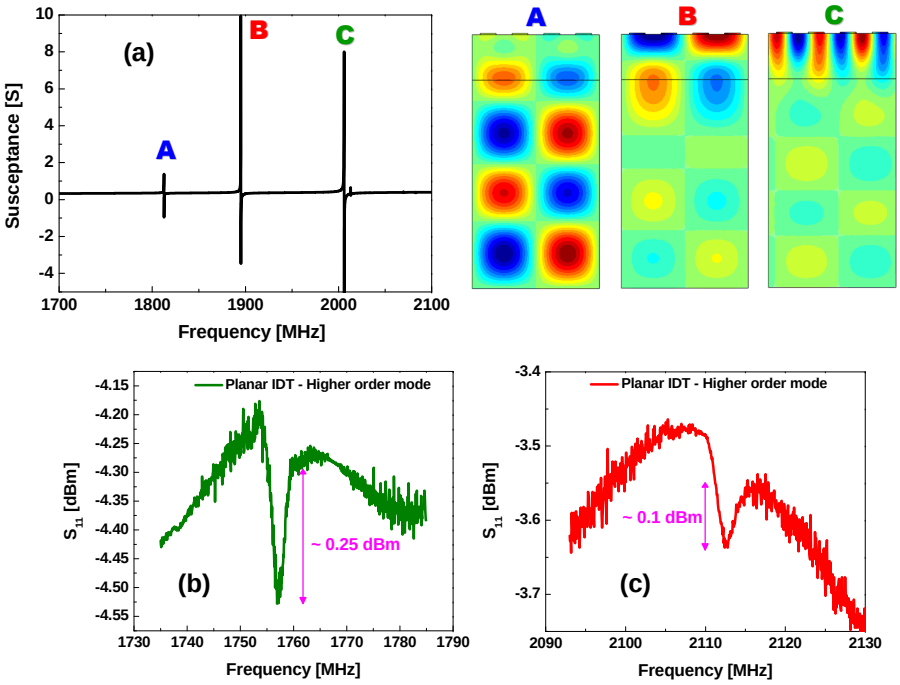

Figure 5.27: Higher order acoustic modes of IDTs fabricated in GaN deposited on sapphire substrate: (a) FEM calculation of the susceptance of for a range of frequencies higher than the fundamental; (b) and (c) show the experimental S_{11} response of two higher order acoustic excitations.

Chapter 6

Application: Frequency Shifter / Single-sideband modulator

The ability to change the color of light, or optical frequency shifting, is key to a number of photonics technologies that are used industrially in fields such as telecommunications, spectroscopy and biomedical. Frequency shifting devices can be designed relying on different physical mechanisms, the most common being electro/acousto/thermo-optical effects. Depending on the optical frequency and amount of shifting needed for a given application, the actual construction of the frequency shifter may vary. Generally speaking though, frequency shifters are bulky with sizes in the centimeter range, they often need exotic optical materials and complicated optical alignment. For these reasons, frequency shifters are usually expensive components. A new design of an optical frequency shifting device based on SAWs is proposed here, posing several advantages over existing devices [135]. In a number of applications this design is expected to have advantages in size and cost in comparison to existing state-of-the-art solutions.

Single sideband (SSB) modulation is an amplitude modulation scheme that efficiently utilizes transmission power and bandwidth by using only one sideband of the frequency spectrum. A comparison between the frequency spectra

of different amplitude modulation schemes is shown in Fig. 6.1. Additionally, in SSB modulators, the carrier is reduced or removed entirely (suppressed), yielding what is then referred to as SSB/SC modulation. This kind of modulator can also be called a frequency shifter, because its functionality corresponds to an actual frequency shifting of the carrier.

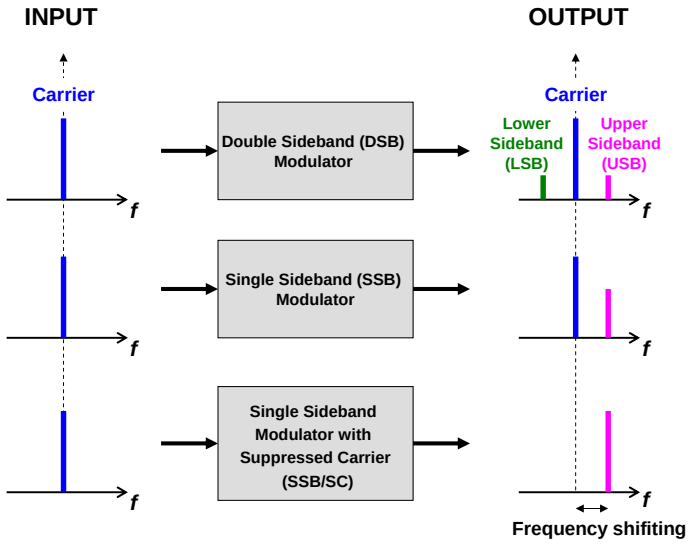

Figure 6.1: Amplitude modulation schemes.

6.1 State-of-the-art

Currently, most available frequency shifters exploit Bragg-type acousto-optical modulation, usually by means of bulk acoustic waves, making use of the shift inherent in the acousto-optic interaction to shift the laser frequency. They rely on the expansion and compression of piezoelectric crystals, including quartz, fused silica, tellurium dioxide, chalcogenide glass, and gallium phosphate. Large crystals are normally required for practical applications, resulting in large and unwieldy device sizes. They usually only achieve shifts of hundreds of MHz, and although a few have allowed shifting in the low gigahertz frequency range, none have as yet been demonstrated which provide larger frequency shifts.

Another type of modulator available today is based on the electro-optic effect - change of the refractive index of a material under an applied electric field. The most common material used for these devices is lithium niobate ($LiNbO_3$). Since their modulation is proportional to the RF applied, they have a very broad band of operation. These devices are however also very bulky; commercially available units are often for applications requiring control of the power of a laser beam. But in conjunction with Mach-Zehnder interferometers (MZIs), they can be used for amplitude modulation. One of the first integrated proposals was the one from Izutsu *et al* [136]. Another more promising approach was proposed by Murata et al, using the polarization reversal technologies of ferroelectric optical materials, first with a two branches MZI [137] and later with a more sophisticated design with 3 branches [138], which would also have the advantage to suppress the carrier - but this device can only be fabricated with ferroelectric materials, what would limit it in terms of photonic integration. Recently, a SSB electro-optic modulator based on lithium niobate MZI waveguides has been proposed [139] and later made available commercially [140]. It has a modulation speed of 10 Gbits/s, and has an optical bandwidth of around 10 GHz, but the configuration required for its operation is quite complex. There are many small-bandwidth applications where this advanced modulator could be overkill. Kakio *et al* [141] proposed the use of SAWs to build such a device, using tandem $LiNbO_3$ waveguides.

The main disadvantages of these proposals in terms of photonic integration are use of exotic materials, dimensions in the order of millimeters, and/or complex operation setups. This proposal [135] tries to alleviate these problems by introducing a compact device (with dimensions of the order of micrometers) with a very simple operation setup (requiring only one RF source), and that can be implemented in standard semiconductor platforms such as Si, GaAs and InP and therefore facilitating integration with other functionalities in a photonic chip.

6.2 Applications

Optical frequency shifters are important system components, and have been used in diverse applications. In sensors and detection systems such as laser Doppler velocimetry (LDV) and Doppler Lidar systems for determining the

direction of motion and enabling simpler processing [142]. Bulk acousto-optic modulators are usually used for this purpose, increasing the cost and the complexity of the system. The device proposed here would enable the construction of a fully integrated compact Doppler sensor system, which is highly relevant in metrology or for biological applications, including blood flow evaluation, as well as other non-contact small-scale measurements. They are used also in optical heterodyne detection systems to provide a frequency shifted local oscillator. In telecommunications for frequency downshifting in radio-over-fiber systems [143] and for photonic down-conversion with optical frequency shift for DWDM systems [144]. Additional applications in photonics are in frequency-shifted feedback (FSF) lasers [145] and for measurements of ultra-high-Q photonic crystal nanocavities [146]. A few of these applications are now discussed in some more depth.

6.2.1 Radio-over-Fiber communication systems

Recent increases in the demand for the broadband data network connectivity has encouraged the development of wireless radio telecommunication systems which utilize millimeter and microwave band frequency spectra. High transmission losses encountered at these operating frequencies are mainly due to air attenuation, however high waveguide losses are also encountered at the link lengths required between source and destination nodes in typical access network scenarios. Due to the low-loss, broadband properties of optical fiber, lightwave transmission systems provide an excellent solution to transport mm-waves; applications which transport such RF signals via an optical infrastructure are called radio-over-fber (RoF). Before it can be transmitted in the fiber, the mm-wave signal has to be modulated onto the lightwave, creating the so called optical mm-wave signal. There are many different kinds of modulation techniques; the one that has shown to give better results is single sideband modulation, since it allows reduced chromatic dispersion penalty after fiber transmission [147], eliminates dispersion-related RF power fading [148, 149], while also providing increased transmission spectral efficiency [150]. Therefore SSB modulators are very important in RoF systems. Several approaches have been proposed to implement SSB modulation for RoF systems, for example by filtering one of the optical sidebands using fiber Bragg gratings [151]. The drawback of this approach is that fiber Bragg gratings have relatively broad

bandwidth, and therefore the filtering may also affect the carrier and the other sideband. A compact and cost-efficient component that would intrinsically provide SSB is certainly desirable for RoF systems.

6.2.2 DWDM in RoF systems

Millimeter-wave fiber-radio access systems promise to meet the demands for services which can support broadband mobile telecommunications service delivery, while simultaneously resolve issues relating to scarcity of available microwave-band RF transmission spectrum. RoF technology is therefore expected to become an important access technology, which will also leverage the ongoing deployment of fiber-to-the-home (FTTH) systems. It is anticipated that future FTTH systems will incorporate support for multiple-wavelength transmission channels through the use of wavelength division multiplexed (WDM) technology [152]. Recently, there has been rapid progress in WDM transmission technologies. Dense WDM (DWDM) shows promise to significantly increase transmission bandwidth implemented within a given optical network, without requiring modification of the electronics used, and also presents further advantages in terms of network reconfigurability and routing flexibility. DWDM-ROF systems and networks therefore represent a viable next step in the evolution of broadband access networking technology. However, in such systems, the subcarriers which carry mm-wave-band RF signals may be separated by tens of gigahertz from its optical carrier, what makes it impossible to apply conventional DWDM optical multiplexers and demultiplexers for RoF systems. It is therefore preferable to generate a low intermediate frequency directly from the optical signal, avoiding the use of high frequency RF signal processing. For this purpose, a frequency down-shifting may also be performed, making the frequency shifter a very important device for DWDM-RoF systems. Complex alternative techniques have been proposed [153, 143, 154], as a response to the high complexity / cost of the frequency shifters/SSMs for GHz range (required for DWDM) proposed so far. The device proposed here would be a very attractive option for this kind of application.

6.2.3 Laser Doppler Anemometry

Laser Doppler velocimetry - also known as Laser Doppler anemometry - is an optical technique for non-intrusive 1D, 2D and 3D point measurement of direction and speed of fluids. It involves two laser beams of slightly different frequencies that interfere and generate a set of moving fringes. A stationary particle in the fringe pattern will scatter light with a frequency equal to the frequency shift of the two interfering beams. When light is scattered from a moving particle, the frequency of the scattered light is shifted by an amount proportional to the speed of the particle, phenomenon that is called Doppler shift. By shifting the frequency of one of the light beams, it is possible to determine the direction of the particles movement, making the frequency shifter again a very important component of the system, and also simplifying the processing of the Doppler systems. Once more, SSB modulation is claimed to be one of the best solutions for these systems [142]. This kind of technique is very important because it allows the measuring of the flow velocities without disturbing the region of the measurement. It has applications in various fields, such as automotive and aeronautic industries (fuel flow, aerodynamics, etc.), environmental research, among many others. Another very interesting application for Laser Doppler systems is in bioinstrumentation, where the blood flow monitors [155] are one of the most known nowadays and also commercially available. If the laser Doppler anemometry systems could be made very compact, they could become very important in biomedical research [156], allowing the investigation of biological objects in living organisms, for example.

6.3 Layout of the device

The device, sketched in Fig. 6.2 , is essentially formed by an input waveguide, where CW quasi-monochromatic light is coupled in, and this waveguide is then divided into N arms (with $N \geq 3$), which will be combined again into a single output waveguide, thus forming a multi-branch or multi-arm Mach-Zehnder interferometer. The optical power is to be distributed equally among the arms. The arms of the interferometer are not identical; they have different lengths or thicknesses and as such a specific static phase delay is created in each one of them.

The modulation is provided by a SAW beam incident perpendicularly to

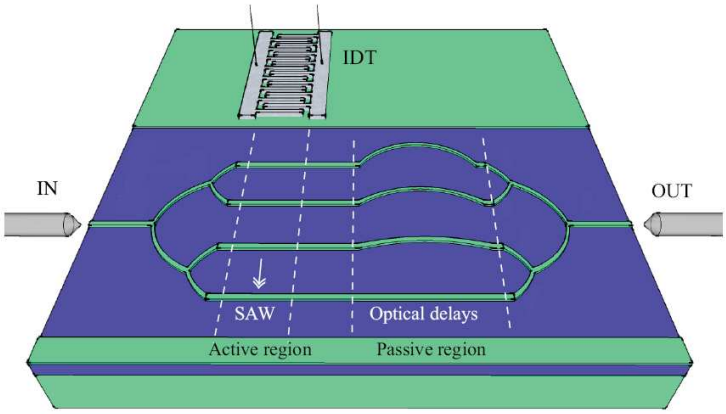

Figure 6.2: Schematic representation of the optical SSB modulator / frequency shifter based on surface acoustic waves (from [90]).

the waveguides that form the arms of the interferometer. The first arm of the interferometer has a distance from the acoustic source such that a specific phase shift is induced by the SAW. The distance between the center of the arms is then equal to λ_{SAW}/N (noting that multiples of λ_{SAW} can be added to this when larger spacing is needed), such that the difference in the modulation phase between two adjacent arms is $2\pi/N$, and therefore the relative phase shift will become independent of the time propagation of the SAW.

The overall layout of the interferometer is such that the combination of static phase shifts and the ones produced by the SAW modulation will generate an output spectrum that contains one frequency component that is shifted with respect to the input by an amount equal to the frequency of the SAW, while the other frequency components are suppressed. Therefore the device operates as an optical frequency shifter.

6.4 Mathematical description

Based on the acousto-optic interaction equations described in Chapter 2 and on the Mach-Zehnder interferometer theory, a general equation was derived for the output electric field of a device with N arms, with each arm having modulation phase of $p2\pi/N$ and static phase delay of $p2\pi/N$:

$$E_{out}(t) = \frac{1}{N}\sum_{p}^{p+N}\left\{E_{in}\sum_{a=-\infty}^{+\infty}J_a(\xi)e^{ia(2\pi f_{SAW}t)}e^{i\left(ap\frac{2\pi}{N}\pm p\frac{2\pi}{N}\right)}\right\} \tag{6.1}$$

where $E_{in} = \exp(i\omega_0 t)$ is the input field, p is any positive or negative integer, N is the number of branches in the MZI, J_a are Bessel functions of first kind of order a, ξ is the Raman-Nath parameter described by Eq. (2.53), and f_{SAW} is the frequency of the surface acoustic wave. The $\pm$ sign determines if the output light will be downshifted (+) or upshifted (-) with respect to the carrier. The modulation amplitude, in the case of a SAW modulation, corresponds to the amount of phase shift that is caused in the light due to the interaction with the SAW.

The active part of the device (SAW modulation) is responsible for generating the sidebands, while the passive part (static phase delays) is responsible for the suppression of the undesired frequency components of the spectrum, by means of destructive interference. That means that, for this configuration, when the SAW is not activated, there will be complete destructive interference of the input light and the device will present an output very close to zero.

To provide a better understanding on how the equation parameters can affect the output light, and also to analyze the robustness of the device regarding fabrication and design imperfections, a detailed analysis of each of these parameters will follow. All the cases have been calculated for a downshifting, and to keep them general the actual frequency scale is not presented in the figures. Instead, it is substituted by the indication of the carrier frequency and the upper and lower sidebands (USB and LSB). The spectra were obtained by performing a Fast Fourier transform (FFT) on Eq. (6.1) for different sets of parameters. All the intensity spectra are normalized, in such a way that the intensity of the input light is equal to 1.

A figure of merit for the calculations can be defined as:

$$FoM = \frac{I_{\text{shifted frequency}}}{\sum I_{\text{all freq. components}}}. \tag{6.2}$$

where I represents intensity. To understand how the combination of the phases provides the suppression of certain sidebands and enhancement of others, it is important to look at the amplitude and phase of the light in each of the arms

of the MZI in the frequency domain. Let us look at the simplest case, for an interferometer with 3 arms.

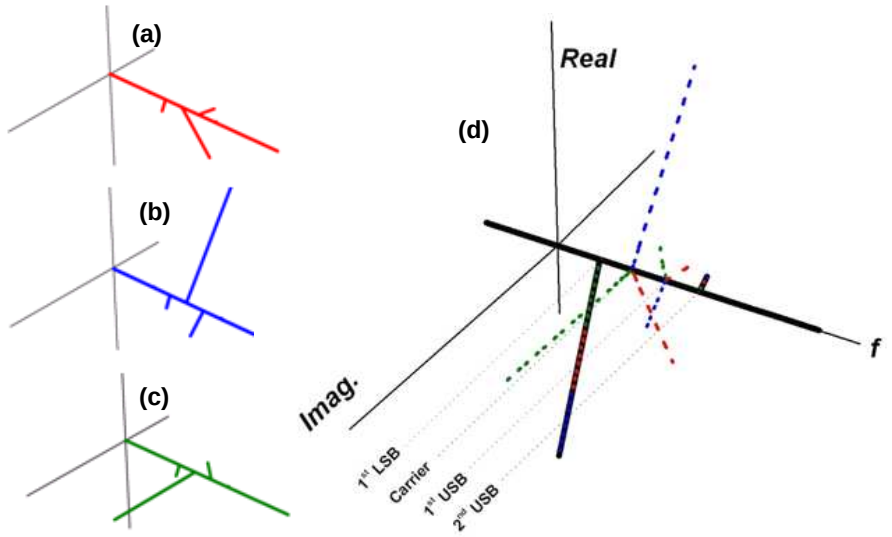

Figure 6.3: Intensity spectrum of the frequency shifter with 3 arms with arbitrary units, where (a), (b) and (c) show the frequency components for each arm of the interferometer, and (d) shows the output light spectrum in black full line, corresponding to the components created by constructive interference. The dashed lines repeat the components of each arm, showing the destructive interference.

Figures 6.3 (a), (b) and (c) show the real and the imaginary part of the electric field of each of the arms, in the frequency domain, after having propagated through the static and dynamic phase changes, while (d) shows the spectrum of the output light, calculated by the summation of the electric field vectors in all the 3 arms, according to Eq. (6.1). If one observes the spectrum of each of the arms independently, the mechanism of the device can be clearly seen. The left sideband, corresponding to the first lower sideband, in this case the desired output frequency component, has the same phase in the 3 arms, and therefore undergoes constructive interference in the output, leading to the maximum possible value of this component in the output. At the same time, the central and right components, corresponding to the carrier and the first upper side-

band, respectively, have different phases in each of the arms, such that when added lead to destructive interference suppressing both frequency components. The resultant output spectrum is then composed of the first lower sideband and a small second upper sideband, which does not undergo full destructive interference in the case of 3 arms. It will be shown in the next subsections that by increasing the number of arms in the interferometer, further undesired sidebands can be suppressed.

6.5 Influence of the number of arms

Most of the frequency shifters based on Mach-Zehnder interferometers previously proposed in the literature are based on interferometers with 3 or 4 arms. But fabricating a Mach-Zehnder interferometer with many arms does not impose severe technological challenges, as previously discussed. An equation for any number of arms has been derived, and now it can be used to study the influence of the number of arms on the performance of the device.

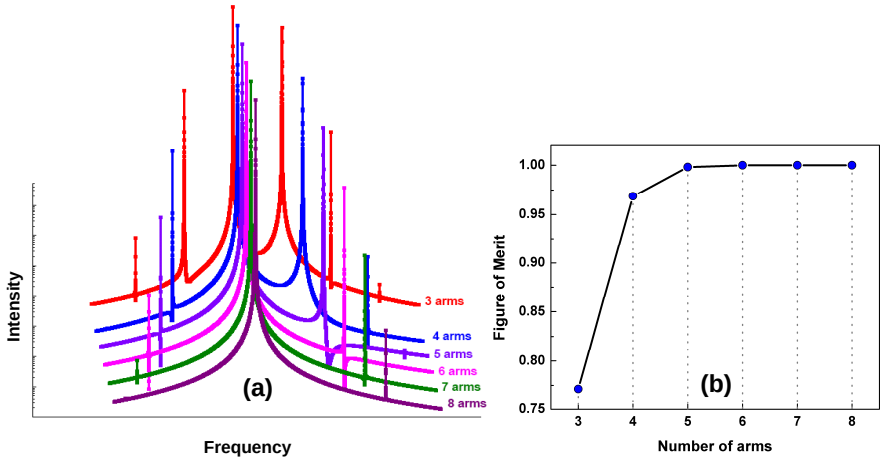

Figure 6.4: (a) Spectra of the light intensity for different number of arms (intensity in logarithmic scale) and (b) FoM for different number of arms.

Fig. 6.4 (a) shows the intensity spectra of the light coming out of the frequency shifter for devices with 3 up to 8 arms, calculated for $\xi = 1.84$, which is the modulation amplitude that gives the maximum possible intensity of the

shifted frequency component, since according to the Bessel functions, J_1 has its maximum at this point. In Fig. 6.4 (b), it is possible to see that the best performance will be obtained for a device with 5 arms or more. By increasing the number of arms, more of the higher-order sidebands are suppressed, leading to a clearer spectrum, and removing the need for filters. It has been demonstrated experimentally that modulated MZIs show better performance for larger number of arms [85].

6.6 Influence of the modulation amplitude

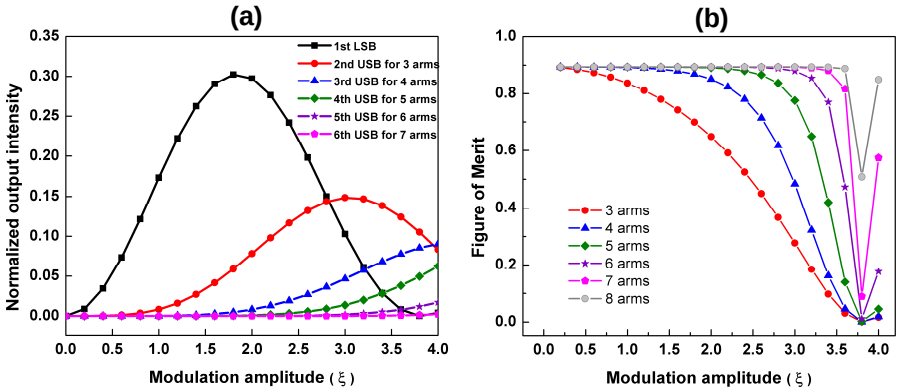

Figure 6.5: (a) Intensity of different frequency components for devices with different number of arms and (b) Figure of merit for different values of modulation amplitude.

The sensitivity of the device to the modulation amplitude determines its power efficiency. The higher the modulation required, the higher the acoustic power that needs to be applied. The calculation of the modulation amplitude for different materials, waveguide structures and SAW parameters has been presented in Chapter 3, and several mechanisms to enhance the modulation were introduced. To provide a more convincing insight of the calculations presented here, it is useful to look at numbers in the literature, previously calculated or measured experimentally. As an example, for the case of Si, using ZnO as the piezoelectric material for the SAW excitation, a refractive index change obtained was approximately $\Delta n = 0.5 \times 10^{-4}$ [157], which corresponds

to an experimental phase shift of 1.3 radians. For GaAs, a phase shift of 0.927 radians was obtained [21]. As discussed in Chapter 2, these phase shifts are dependent on the properties of the material, of the SAW, of the light, and on the overlap between the SAW and the optical mode. Hence, all these parameters should be taken into account when designing the device. Using Eq. (6.1), the output intensity and the FoM for several different modulation amplitudes have been calculated, and they are presented in Fig. 6.5 (a) and (b). Notice that for devices with larger number of arms, the FoM is mostly insensitive to the modulation amplitude. That can be explained by the fact that, for a certain modulation amplitude, the intensity of the shifted frequency is the same for devices with any number of arms, but the intensity of the unwanted frequencies is almost null for larger number of arms.

6.7 Influence of the static delays

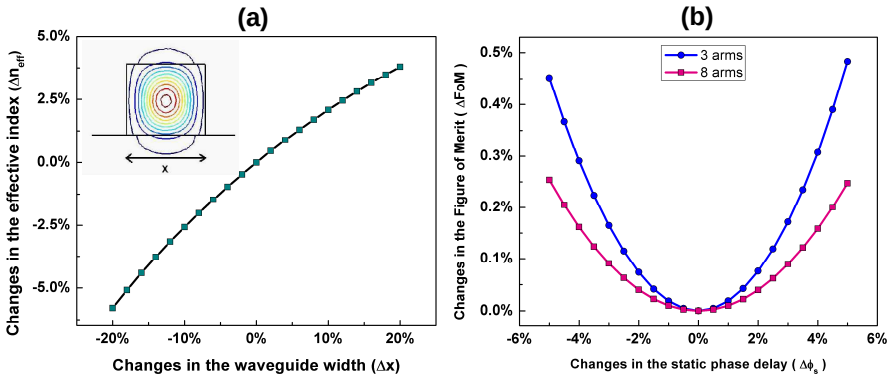

Figure 6.6: (a) Relation between changes in the width of the waveguide and in the effective index of the TE mode and (b) Influence of changes in the static phase delay in the FoM of devices with 3 and 8 arms.

Tolerances in the fabrication must be taken into account when designing the device, since the dimensions of the waveguides can be altered during the fabrication process. Changes in the width of the waveguides are the most common imperfection. These changes Δx in the width of the waveguides lead to changes in the effective refractive index of the guided mode, therefore affecting

the phase delay.

To evaluate how changes in the width of a waveguide affects its guided mode, FEM calculations of the effective index of the TE mode of a SOI waveguide were performed, with fixed height of 340 nm, and initial width of 450 nm, which was varied by up to ±20%. The results of these calculations are shown in Fig. 6.6 (a), and it can be observed that changes in width of ±20% result in changes in the effective index of around ±5%. The parameters Δn_{eff} and $\Delta\phi_s$ are directly proportional, and therefore it is calculated how changes of ±5% in the static phase delay would affect the FoM, and the results are shown in Fig. 6.6 (b). It is observed that the FoM is very robust towards these changes, and that devices with more arms are even more robust to these changes in the geometry of the waveguides.

6.8 Influence of power splitting

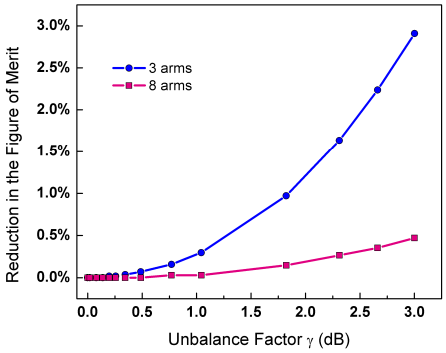

Figure 6.7: FoM of the device versus the unbalance factor for 3 and 8 arms.

The power distribution from the input waveguide to the arms of the interferometer can be implemented in many different ways, like for example by using cascaded y-splitters [158], or by using MMIs [159] with $1 \times N$ outputs or in cascade [160]. Power splitters can have very good performance, but nevertheless differences in the power splitting ratio might occur due to fabrication imperfections, and thus it is important to investigate the performance of the device towards this unbalance. Disregarding the losses of the power splitters, a power splitting balance coefficient γ can be defined as the ratio between the

maximum and minimum intensity in the arms in dB. When $\gamma = 0$ dB, there is no unbalance and the power is equally distributed between the arms. Usual values of γ are between 0.1 and 0.3 dB [158],[160]. Fig. 6.7 shows the results of the calculations for different values of γ. Within the usual values of unbalance, the performance of the device would be very little affected. It is observed though that the more unbalanced the system is, the worse the performance of the device, therefore showing the importance of designing well balanced power splitters. It is also noticed that the device with 8 arms is again much more tolerant to splitting unbalance than the device with 3 arms.

6.9 Bandwidth of operation

Devices are usually designed for optimal operation at a certain input wavelength, and it is important to analyze the performance of the same device for different input wavelengths. By looking at Eq. (6.1), it is possible to identify the parameters that are influenced by the optical wavelength: i) The static phase shifts, represented by $p\pi/N$, are usually designed by creating a path difference between the arms. Ignoring the losses that might be introduced by tapers or bends, one can calculate this phase shift using Eq. (4.15), where both ω_0 and n_{eff} vary with the wavelength. It is clear that by using the path difference originally designed for a different wavelength, the phase shift will change; therefore disturbing the destructive interference of the interferometer. ii) The modulation amplitude, described by the factor ξ from Eq. (2.53), depends on the wavelength through both k_0 and Δn, since usually the refractive index of the material is also wavelength dependent.

Taking the parameters described above into consideration, calculations were performed for a device with 8 arms that was optimally designed for operation at 1.55 μm, and built with SOI waveguides with a width of 450 nm and a height of 340 nm. The dispersion curve for such a waveguide was calculated using finite element method, and is shown in Fig. 6.8 (a). The FoM of this device was calculated, for different input wavelengths, and varying the static phase and the modulation amplitude according to the changes in the optical wavelength and in the effective index. Defining the bandwidth of operation as the range of wavelengths with a FoM above half of its maximum, the bandwidth obtained for this specific device is around 0.9 μm, as shown in Fig. 6.8 (b).

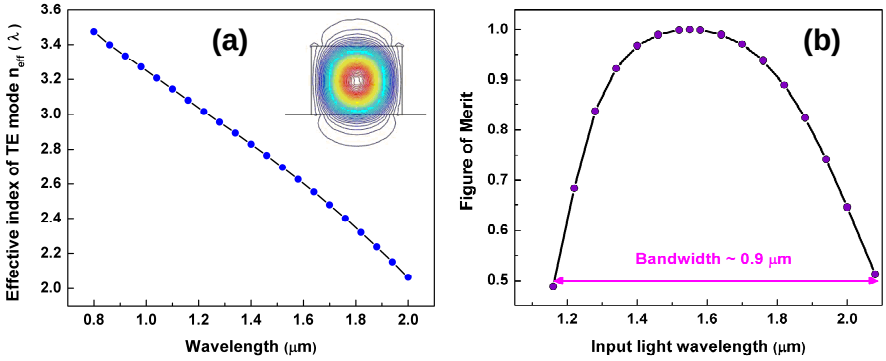

Figure 6.8: (a) Dispersion curve for an SOI ridge waveguide with width of 450 nm and height of 340 nm, where the inset shows the TE mode distribution; (b) FoM for different wavelengths of input light of an SOI device designed for optimal operation at 1.55 μm. The operation bandwidth is indicated in the figure.

6.10 Multiple frequency shifting

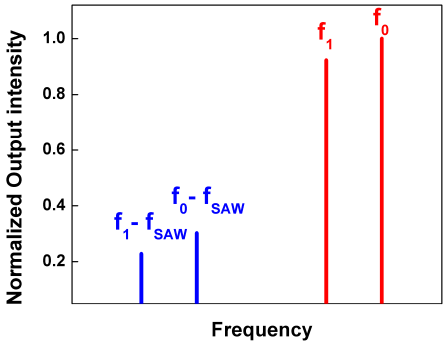

Figure 6.9: Spectrum of the input frequencies f_0 and f_1 and the resultant shifted frequencies $f_0 - f_{SAW}$ and $f_1 - f_{SAW}$.

It was shown in the previous section that the device can present a quite broad bandwidth of operation. Therefore, one can incouple more than one input frequency, within a certain frequency range, and all the frequencies will be shifted by the same amount. When applying two input frequencies, f_0 being

the frequency of operation for which the device was designed, and f_1 being another frequency within the bandwidth of operation, the spectrum shown in Fig. 6.9 is obtained.

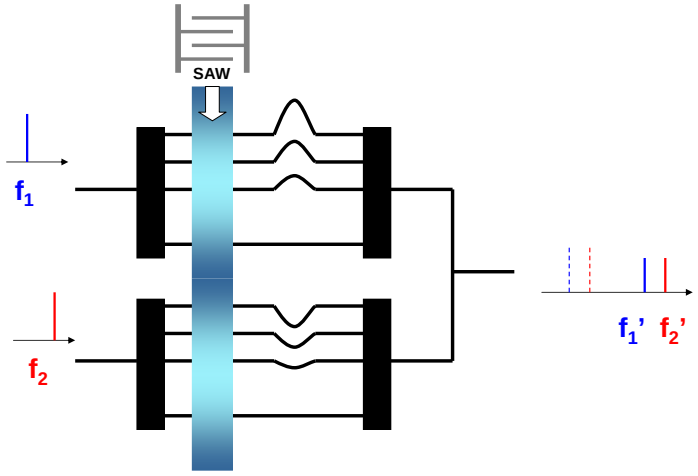

Figure 6.10: Scheme for simultaneous modulation of frequency shifters in parallel.

For applications where the input frequencies lay outside the operation bandwidth, a scheme with interferometers in parallel can be used, with each of them designed with different static delays for the different input frequencies, while the modulation can be provided by the same acoustic source, such as in the scheme shown in Fig. 6.10.

Chapter 7

Conclusion

This work has thoroughly investigated many aspects related to the modeling, design and fabrication of integrated ultrasonic-photonic devices.

The modeling of different systems brought many insights regarding the choices of photonic components and materials to be used. First, the geometry of the channel waveguides has proven to play an important role in many aspects of the performance of the device. By choosing an appropriate etching depth, the fabrication tolerances can be alleviated, the optical confinement can be improved, and finally the acousto-optical modulation can be increased more than 4 times for the case of the GaAs/AlGaAs waveguides. In the case of non-piezoelectric materials, such as silicon, the configuration used for the thin-film deposition has also shown to have a strong influence on the acousto-optical performance of the device. The use of planarization layers has proven to be the best configuration, and its thickness must also be chosen carefully. By doing so, an increase of almost 7 times in the modulation can be obtained, compared to the non-planarized alternative. The use of slow light to enhance the phase modulation in waveguides, by means of photonic crystal structures, has also been investigated, proving to be a promising approach on the construction of compact and power-saving photonic devices. The photonic crystals also have many advantages in terms of integration, since many other functionalities have already been demonstrated using this kind of photonic structure, and a complete circuit constructed only with photonic crystal components, including the acoustic modulation as one of the active parts, could be envisioned. Finally, it

was demonstrated that the concept of using Lamb waves in membranized channel waveguides for acousto-optic modulation, shown here for the first time, is expected to be an efficient alternative to improve performance and increase frequency of operation of ultrasonic-photonic devices. Furthermore, this concept can also be extended to membranized photonic crystals, combining the two forms of enhancement and leading to even more efficient components.

The design aspects of the main components of ultrasonic-photonic devices based on channel waveguides and Mach-Zehnder interferometers were also discussed in detail. First, the challenge of finding the appropriate numerical method for the calculations, due to the rather large typical dimensions of the devices, has been presented. The best strategy is to use, whenever possible, different tools for different parameter calculations, trying to take advantage of each tool in terms of accuracy and speed. To be able to make efficient devices, many parameters have to be taken into account in the design. A few of them were shown here, such as: single-mode guidance, optical coupling to the fiber, bending losses, power splitting, phase delays and coupling between adjacent waveguides. A careful design of all these characteristics can make the device more robust towards fabrication tolerances, reduce costs, improve performance and reduce dimensions, making the device more industrially competitive.

Fabrication processes were developed in this work for producing integrated ultrasonic-photonic devices, and their steps were described for three different material platforms. The individual parts of the device could be fabricated and characterized, showing the expected behavior and proving the validity of the modeling, the design and the fabrication methods here developed. The low yield of good acoustic and optical components simultaneously on a chip was unfortunately too low to allow the measurement of a complete final device. But a lot of progress has been made from the initial fabrication process, and many of the problems have already been solved. The work done will hopefully serve as a solid basis for further development on the fabrication, and the new fabrication facilities recently made available, such as the III-V ICP-RIE etching machine, will help on increasing the yield of the components.

A new design for an optical single sideband modulator/frequency shifter based on SAWs has been introduced. It shows a lot of advantages in terms of integration and size when compared to the existing technology. The design has proven to be robust towards fabrication imperfections, and opens up a

whole new group of applications for this class of integrated ultrasonic-photonic devices.

In resume, a new exciting class of photonic devices has been analyzed in all the aspects that involve its conception, from modeling the physical effects involved, to the design of the components, up to the fabrication processes that could be applied. Photonic components based on acoustic modulation have only very recently started to be implemented in standard semiconductors, and not much work in this area has been done up to this moment. We believe that this work sheds some light on the main challenges related to this technology and offers many solutions and some new tracks to be pursued for the development of this technology up to industrial scale.

List of publications

Barretto, E. C. S. and Hvam, J. M., *Membranized Semiconductor Rib Waveguides for Acousto-optic Modulation Enhancement.* In Latin America Optics and Photonics Conference, OSA Technical Digest (CD) (Optical Society of America, 2010), paper MD3.

Barretto, E. C. S. and Hvam, J. M., *Photonic integrated single-sideband modulator/frequency shifter based on surface acoustic waves.* In: Proceedings of SPIE - The International Society for Optical Engineering, 7719 (1), p. 771920-12, 2010.

de Heyn, P. *A compact optical frequency shifter using a multi-branch waveguide interferometer*, Master thesis, DTU Fotonik, 2009. Supervised by: E. C. S. Barretto, J. M. Hvam, and R. Bats.

Barretto, E. C. S. and Poel, M. van der, *Photonic Crystal waveguides for enhancement of Surface Acoustic Wave modulation - a numerical study*, PECS VIII - The 8th International Photonic and Electromagnetic Crystal Structures Meeting, Abstract Book, 2009.

Barretto, E. C. S. and Poel, M. van der, *Photonic Single Sideband Modulator / Frequency shifter based on Surface Acoustic Waves*, DTU PhD Challenge - Venture Cup, 2008.

Patent applications

Barretto, E. C. S. and Poel, M. van der, "Light modulation device", patent filed on the 15th of June of 2009 as EP application under number 09162705.9 and as US application under number 61/187,084.

List of Abbreviations

AC: alternating current
BAW: bulk acoustic wave
BPM: beam propagation method
CW: continuous wave
DC: direct current
DSB: double sideband
DTU: Technical University of Denmark
DWDM: dense wavelength-division multiplexing
EIM: effective index method
EME: eigenmode expansion
FDTD: finite-difference time-domain
FEM: finite element method
FMM: film mode matching
FoM: figure of merit
FTTH: fiber-to-the-home
HSQ: hydrogen silsesquioxane
ICP: inductively coupled plasma
IDT: interdigital transducer
LSB: lower sideband
MBE: molecular beam epitaxy
MEMS: micro-electromechanical system
MMI: multi-mode interference
MOVPE: metalorganic vapour phase epitaxy
MZI: Mach-Zehnder interferometer
OSA: optical spectrum analyzer
PDE: partial differential equation

PECVD: plasma enhanced chemical vapor deposition
PhC: photonic crystal
PML: perfectly matched layer
PMMA: Polymethyl methacrylate
PWE: plane wave expansion
RF: radio-frequency
RIE: reactive ion etching
RoF: radio over fiber
SAW: surface acoustic wave
SEM: scanning electron microscope
SC: suppressed carrier
SOI: silicon-on-insulator
SSB: single sideband
SSB/SC: single sideband with suppressed carrier
SSM: single sideband modulator
TE: transverse electric
TLS: tunable laser source
TM: transverse magnetic
USB: upper sideband
WDM: wavelength-division multiplexing
WG: waveguide

Bibliography

[1] M. M. D. Lima & P. V. Santos, Modulation of photonic structures by surface acoustic waves, *Reports on Progress in Physics* **68**, 1639–1701 (2005).

[2] O. D. D. Couto, *et al.*, Photon anti-bunching in acoustically pumped quantum dots, *Nature Photonics* **3**, 645–648 (2009).

[3] M. Eichenfield, J. Chan, R. M. Camacho, K. J. Vahala, & O. Painter, Optomechanical Crystals, *Nature* **462**, 16 (2009).

[4] D. Bria, *et al.*, Opening of simultaneous photonic and phononic band gap in two-dimensional square lattice periodic structure, *Journal of Applied Physics* **109**, 014507 (2011).

[5] B. E. A. Saleh & M. C. Teich, *Fundamentals of Photonics*, volume 45 of *Wiley Series in Pure and Applied Optics* (Wiley, 1991).

[6] J. Goell, Rib waveguide for integrated optical circuits, *Applied Optics* **12**, 2797–2798 (1973).

[7] R. G. Hunsperger, *Integrated Optics: Theory and Technology* (Springer, 1985).

[8] I. Chang, Acoustooptic devices and applications, *IEEE Transactions on Sonics Ultrasonics* **23**, 2–22 (1976).

[9] E. I. Gordon, A review of acoustooptical deflection and modulation devices., *Applied Optics* **5**, 1629–1639 (1966).

[10] A. Korpel, R. Adler, P. Desmares, & W. Watson, A television display using acoustic deflection and modulation of coherent light., *Applied Optics* **5**, 1667–1675 (1966).

[11] R. Dixon, Acoustic diffraction of light in anisotropic media, *IEEE Journal of Quantum Electronics* **3**, 85–93 (1967).

[12] J. W. S. Rayleigh, *The Theory of Sound*, volume 2 (Dover, 1945).

[13] H. Ollendorf, D. Schneider, T. Schwarz, & A. Mucha, Nondestructuve evaluation of thin films with interface defects by surface acoustic-waves, *Surface and Coatings Technology* **74-5**, 246–252 (1995).

[14] M. Lewis, SAW and optical signal processing, in *Ultrasonics Symposium, 2005 IEEE*, volume 2, 800 – 809 (2005).

[15] L. Kuhn, M. Dakss, & P. Heidrich, Deflection of an optical guided wave by a surface acoustic wave, *Applied Physics Letters* **17**, 265–267 (1970).

[16] L. Kuhn, P. F. Heidrich, & E. G. Lean, Optical Guided Wave Mode Conversion by an Acoustic Surface Wave, *Applied Physics Letters* **19**, 428 (1971).

[17] M. Dakss, L. Kuhn, P. F. Heidrich, & B. A. Scott, Grating coupler for efficient excitation of optical guided waves in thin films, *Applied Physics Letters* **16**, 523 (1970).

[18] W. S. C. Chang, Acoustooptical deflections in thin films, *IEEE J. Quantum Electron.* **7**, 167 (1971).

[19] C. Tsai, C. Chang, C. Lee, & K. Liao, Acoustooptic Bragg Deflection in Channel Optical Waveguides, *1980 Topical Meeting on Integrated and Guidtd-Wave Optics,Technical Digest of Post-Deadline Papers* PD7–1 (1980).

[20] C. Gorecki, F. Chollet, E. Bonnotte, & H. Kawakatsu, Silicon-based integrated interferometer with phase modulation driven by surface acoustic waves., *Optics Letters* **22**, 1784–1786 (1997).

[21] M. M. de Lima, M. Beck, R. Hey, & P. V. Santos, Compact Mach-Zehnder acousto-optic modulator, *Applied Physics Letters* **89**, 121104 (2006).

[22] M. Beck, *et al.*, Acousto-optical multiple interference switches, *Applied Physics Letters* **91**, 061118 (2007).

[23] B. A. Auld, *Acoustic Fields and Waves in Solids*, volume 1 (John Wiley and Sons, 1973).

[24] D. Morgan, *Surface Acoustic Wave Filters: With Applications to Electronic Communications and Signal Processing* (Academic Press, 2007).

[25] F. I. Fedorov, *Theory of Elastic Waves in Crystals* (Plenum Press, 1968).

[26] S. Adachi, *Properties of Group-IV, III-V and II-VI Semiconductors* (Wiley, 2005).

[27] V. M. Ristic, *Principles of acoustic devices* (John Wiley & sons, Inc, 1983).

[28] L. Rayleigh, On Waves Propagating along the Plane Surface of an Elastic Solid, *Proceedings of the London Mathematical Society* (1885).

[29] H. Lamb, On Waves in an Elastic Plate, *Society* **93**, 114–128 (1917).

[30] A. E. H. Love, *Some Problems of Geodynamics* (Cambridge University Press, 1911).

[31] R. Stoneley, Elastic waves at the surface of separation of two solids, *Proceedings of the Royal Society of London Series A Containing Papers of a Mathematical and Physical Character* **106**, 416–428 (1924).

[32] I. A. Viktorov, *Rayleigh and lamb waves* (Plenum Press, 1967).

[33] J. L. Rose, *Ultrasonic Waves in Solid Media*, volume 107 (Cambridge University Press, 2004).

[34] R. White & F. Voltmer, Direct Piezoelectric Coupling to Substrate Elastic Waves, *Applied Physics Letters* (1965).

[35] T. Bristol, W. Jones, P. Snow, & W. Smith, Applications of double electrodes in acoustic surface wave device design, in *1972 Ultrasonics Symposium*, 343–345 (1972).

[36] K.-y. Hashimoto, *Surface Acoustic Wave Devices in Telecommunications* (Springer, 2000).

[37] Y. Takagaki, *et al.*, Guided propagation of surface acoustic waves in AlN and GaN films grown on 4H-SiC(0001) substrates, *Physical Review B* **66**, 1–7 (2002).

[38] H. Nishihara, M. Haruna, & T. Suhara, *Optical Integrated Circuits* (McGraw-Hill, 1985).

[39] M. Huang, Stress effects on the performance of optical waveguides, *International Journal of Solids and Structures* **40**, 1615–1632 (2003).

[40] M. Ettenberg & R. J. Paff, Thermal expansion of AlAs, *Journal of Applied Physics* **41**, 3926 – 3927 (1970).

[41] E. M. Conwell & R. D. Burnham, Materials fo integrated optics: GaAs, *Ann. Rev. Mater. Sci.* **8**, 135–179 (1978).

[42] R. N. Hall, G. E. Fenner, J. D. Kingsley, T. J. Soltys, & R. O. Carlson, Coherent light emission from GaAs junctions, *Physical Review Letters* **9**, 366–368 (1962).

[43] S. Adachi, GaAs, AlAs, and Al(x)Ga(1-x)As: Material parameters for use in research and device applications, *Journal of Applied Physics* **58**, R1–R29 (1985).

[44] O. Bisi, Porous silicon: a quantum sponge structure for silicon based optoelectronics, *Surface Science Reports* **38**, 1–126 (2000).

[45] P. Mutti, *et al.*, Room-temperature visible luminescence from silicon nanocrystals in silicon implanted SiO2 layers, *Applied Physics Letters* **66**, 851 (1995).

[46] G. Franz, F. Priolo, S. Coffa, A. Polman, & A. Carnera, Room-temperature electroluminescence fro Er-doped crystalline Si, *Applied Physics Letters* **64**, 17 (1994).

[47] H. Park, A. Fang, S. Kodama, & J. Bowers, Hybrid silicon evanescent laser fabricated with a silicon waveguide and III-V offset quantum wells., *Optics Express* **13**, 9460–9464 (2005).

[48] A. W. Fang, *et al.*, A continuous-wave hybrid AlGaInAs-silicon evanescent laser, *IEEE Photonics Technology Letters* **18**, 1143–1145 (2006).

[49] X. Y. Du, *et al.*, ZnO film for application in surface acoustic wave device, *Journal of Physics Conference Series* **76**, 012035 (2007).

[50] L. L. Brizoual, *et al.*, GHz Frequency ZnO / Si SAW Device, *Ultrasonics Symposium, 2005 IEEE* **4**, 2174–2177 (2005).

[51] E. Feltin, *et al.*, Broadband blue superluminescent light-emitting diodes based on GaN, *Applied Physics Letters* **95**, 081107 (2009).

[52] O. Ambacher, Growth and applications of Group III-nitrides, *Journal of Physics D: Applied Physics* **31**, 2653–2710 (1998).

[53] C. Deger, *et al.*, Sound velocity of $Al_xGa_{1-x}N$ thin films obtained by surface acoustic-wave measurements, *Applied Physics Letters* **72**, 2400 (1998).

[54] K. H. Choi, *et al.*, Experimental and theoretical characterization of the surface acoustic wave propagation properties of GaN epitaxial layers on c-plane sapphire, *Journal of Materials Research* **18**, 1157–1161 (2011).

[55] Comsol Multiphysics, www.comsol.com.

[56] Matlab, Mathworks, www.matlab.com.

[57] M. Arakawa, J.-i. Kushibiki, & Y. Madani, Ultrasonic Micro-Spectroscopy of Synthetic Sapphire Crystals, *Japanese Journal of Applied Physics* **47**, 2285–2287 (2008).

[58] J. Jin, *The Finite Element Method in Electromagnetics*, Springer {L}ehrbuch (Wiley-IEEE Press, 2002).

[59] C. Pollock & M. Lipson, *Integrated Photonics* (Springer, 2003), 1st edition.

[60] K. Okamoto, *Fundamentals of optical waveguides* (Academic Press, 2006).

[61] W. Chew & Q. Liu, Perfectly Matched Layers for Elastodynamics: A New Absorbing Boundary Condition, *J. Comp. Acoustics* **4**, 341–359 (1996).

[62] S. H. Simon, Coupling of Surface Acoustic Waves to a Two Dimensional Electron Gas, *Physical Review B* (1996).

[63] R. Stoneley, The Propagation of Surface Elastic Waves in a Cubic Crystal, *Proc. R. Soc. Lond. A* **232**, 447–458 (1955).

[64] G. S. May & S. M. Sze, *Fundamentals of Semiconductor Fabrication* (John Wiley & sons, Inc, 2004).

[65] A. D. Ferguson, *et al.*, Low-loss, single-mode GaAs/AlGaAs WGs with large core thickness, *IEE Proc. Optoelectronics* **153**, 51–56 (2006).

[66] P. Dong, *et al.*, Low loss shallow-ridge silicon waveguides., *Optics Express* **18**, 14474–14479 (2010).

[67] E. Yablonovitch, Inhibited Spontaneous Emission in Solid-State Physics and Electronics, *Physical Review Letters* **58**, 2059–2062 (1987).

[68] S. John, Strong localization of photons in certain disordered dielectric superlattices, *Physical Review Letters* **58**, 2486–2489 (1987).

[69] M. Loncar, *et al.*, Waveguiding in planar photonic crystals, *Applied Physics Letters* **77**, 1937 (2000).

[70] J. M. Lourtioz, H. Benisty, V. Berger, A. Tchelnokov, & D. Maystre, *Photonic Crystals Towards Nanoscale Photonic Devices* (Springer-Verlag, 2005).

[71] M. Notomi, *et al.*, Extremely large group-velocity dispersion of line-defect waveguides in photonic crystal slabs., *Physical Review Letters* **87**, 253902 (2001).

[72] T. F. Krauss, Slow light in photonic crystal waveguides, *Journal of Physics D: Applied Physics* **40**, 2666–2670 (2007).

[73] A. Lavrinenko, *et al.*, Comprehensive FDTD modelling of photonic crystal waveguide components., *Optics Express* **12**, 234–248 (2004).

[74] J. D. Joannopoulos, S. G. Johnson, J. N. Winn, & R. D. Meade, *Photonic Crystals: Molding the Flow of Light* (Princeton University Press, 2008).

[75] L. H. Frandsen, A. V. Lavrinenko, J. Fage-Pedersen, & P. I. Borel, Photonic crystal waveguides with semi-slow light and tailored dispersion properties., *Optics express* **14**, 9444–50 (2006).

[76] M. Soljačić, *et al.*, Photonic-crystal slow-light enhancement of nonlinear phase sensitivity, *JOSA B* **19**, 2052–2059 (2002).

[77] N. Courjal, *et al.*, Acousto-optically tunable lithium niobate photonic crystal, *Applied Physics Letters* **96**, 131103 (2010).

[78] D. a. Fuhrmann, *et al.*, High-frequency tuning of photonic crystal defect cavity modes using surface acoustic waves, *Proceedings of SPIE* **7609**, 760908–760908–9 (2010).

[79] T. G. Giallorenzi, Acousto-optical deflection in thin-film waveguides, *Journal of Applied Physics* **44**, 242 (1973).

[80] S. Hascik, Z. Mozolova, T. Lalinsky, M. Tomaska, & I. Kostic, Patterning of a micromechanical coplanar waveguide using a dry etching technique, *Vacuum* **69**, 283–287 (2002).

[81] M. Kadota, T. Ogami, K. Yamamoto, H. Tochishita, & Y. Negoro, High-frequency Lamb wave device composed of MEMS structure using LiNbO3 thin film and air gap., *IEEE transactions on ultrasonics, ferroelectrics, and frequency control* **57**, 2564–71 (2010).

[82] E. C. S. Barretto & J. M. Hvam, Membranized Semiconductor Rib Waveguides for Acousto-optic Modulation Enhancement, in *Latin America Optics and Photonics Conference*, 6–8 (Optical Society of America, 2010).

[83] K. Uozumi, K. Ohsone, & R. White, Generation and detection of ultrasonic Lamb waves in a thin deposited film by using interdigital transducers, *Applied Physics Letters* **43**, 917–919 (2009).

[84] D. Bardzokas & N. Senik, The excitation of symmetric and antisymmetric lamb waves in a piezoelectric strip by surface electrodes, *Journal of Applied Mathematics and Mechanics* **57**, 1047–1055 (1993).

[85] M. Beck, M. M. de Lima, & P. V. Santos, Acousto-optical multiple interference devices, *Journal of Applied Physics* **103**, 014505 (2008).

[86] R. M. Knox & P. P. Toulios, Integrated Circuits for the Millimeter through Optical Frequency Range, *Proceedings Symposium on Submillimeter Waves* 497 (1970).

[87] V. Ramaswamy, Strip-loaded film waveguide, *Bell Syst. Tech. J* **53**, 697–704 (1974).

[88] S. Pogossian, L. Vescan, & a. Vonsovici, The single-mode condition for semiconductor rib waveguides with large cross section, *Journal of Lightwave Technology* **16**, 1851–1853 (1998).

[89] OlympIOs, C2V, www.c2v.nl/products/software/olympios-software.shtml.

[90] P. D. Heyn, *A compact optical frequency shifter using a multi-branch waveguide interferometer*, Ph.D. thesis, DTU - Technical University of Denmark (2009).

[91] Fimmwave, Photon Design, www.photond.com/products/fimmwave.htm.

[92] A. Sudbo, Film mode matching: a versatile numerical method for vector mode field calculations in dielectric waveguides, *Pure and Applied Optics: Journal of the European Optical Society Part A* **2**, 211 (1993).

[93] A. Sudbo, Improved formulation of the film mode matching method for mode field calculations in dielectric waveguides, *Pure and Applied Optics: Journal of the European Optical Society Part A* **3**, 381 (1994).

[94] Fimmprop, Photon Design, www.photond.com/products/fimmprop.htm.

[95] D. F. G. Gallagher & T. P. Felici, Eigenmode Expansion Methods for Photonics - Pros and Cons, *Photonics West, San Jose, 2003* 1–14.

[96] E. Marcatili, Slab-coupled waveguides, *Bell Syst. Tech. J* **53**, 645–674 (1974).

[97] R. A. Soref, J. Schmidtchen, & K. Petermann, Large Single-Mode Rib Waveguides in GeSi-Si and Si-on-SO2, *Quantum* **27**, 1971–1974 (1991).

[98] M. de Laurentis, A. Irace, & G. Breglio, Determination of single mode condition in dielectric rib waveguide with large cross section by finite element analysis, *Journal of Computational Electronics* **6**, 285–287 (2007).

[99] G. Wenke & Y. Zhu, Comparison of efficiency and feedback characteristics of techniques for coupling semiconductor lasers to single-mode fiber, *Applied optics* **22**, 3837–3844 (1983).

[100] I. Moerman, P. Van Daele, & P. Demeester, A review on fabrication technologies for the monolithic integration of tapers with III-V semiconductor devices, *IEEE Journal of Selected Topics in Quantum Electronics* **3**, 1308–1320 (1997).

[101] R. N. Thurston, E. Kapon, & a. Shahar, Two-dimensional control of mode size in optical channel waveguides by lateral channel tapering., *Optics letters* **16**, 306–8 (1991).

[102] R. E. Smith, *et al.*, Reduced Coupling Loss Using a Tapered-Rib Adiabatic-Following Fiber Coupler - IEEE Photonics Technology Letters, *Technology* **8**, 2–4 (1996).

[103] M. Heiblum & J. Harris, Analysis of Curved Optical Waveguides by Conformal Transformation, *IEEE Journal of Quantum Electronics* **11**, 75–83 (1975).

[104] J. Yamauchi, O. Saito, & M. Ikegaya, Comparison of insertion losses of s-shaped optical waveguide bends, *and Optical* **7**, 399–401 (1994).

[105] A. Bhatnagar, K. R. S. Nair, R. Kumar, K. Chalapati, & Y. G. K. Patro, Study of cross coupling in transition bends using cascaded coupler segment method, *Journal of Molecular Evolution* **43**, 1004–1007 (1996).

[106] F. J. Mustieles, E. Ballesteros, & P. Baquero, Theoretical S-bend profile for optimization of optical waveguide radiation losses **5**, 551–553 (1993).

[107] E. Neumann, Curved dielectric optical waveguides with reduced transition losses, *Optics and Antennas, IEE Proceedings H* **129**, 278 (2008).

[108] R. Baets & P. E. Lagasse, Calculation of radiation loss in integrated-optic tapers and Y-junctions., *Applied Optics* **21**, 1972–1978 (1982).

[109] T. Yabu, M. Geshiro, & S. Sawa, New design method for low-loss Y-branch waveguides, *Journal of Lightwave Technology* **19**, 1376–1384 (2001).

[110] L. Cascio, T. Rozzi, & L. Zappelli, Radiation loss of Y-junctions in rib waveguide, *IEEE Transactions on Microwave Theory and Techniques* **43**, 1788–1797 (1995).

[111] C.-w. Hsu, S. Member, H.-l. Chen, & W.-s. Wang, Compact Y -Branch Power Splitter Based on, *Technology* **15**, 1103–1105 (2003).

[112] C. Chaudhari, D. S. Patil, & D. Gautam, A new technique for the reduction of the power loss in the Y-branch optical power splitter, *Optics Communications* **193**, 121–125 (2001).

[113] M. Hu, J. Huang, R. Scarmozzino, M. Levy, & R. Osgood, A low-loss and compact waveguide Y-branch using refractive-index tapering, *IEEE Photonics Technology Letters* **9**, 203–205 (1997).

[114] O. Bryngdahl, Image formation using self-imaging techniques, *Journal of the Optical Society of America* **63**, 416 (1973).

[115] P. Besse, M. Bachmann, H. Melchior, L. Soldano, & M. Smit, Optical bandwidth and fabrication tolerances of multimode interference couplers, *Journal of Lightwave Technology* **12**, 1004–1009 (1994).

[116] J. M. Heaton, *et al.*, Novel I-to-N way integrated optical beam splitters mixing in GaAs / AIGaAs multimode waveguides using symmetric mode, *Applied Physics Letters* **61**, 1754–1756 (1992).

[117] R. M. Lorenzo, C. Llorente, E. J. Abril, J. C. Aguado, & M. López, Method of achieving phase delay with wide optical bandwidth in multimode interference devices., *Optics letters* **23**, 1748–50 (1998).

[118] R. P. Ratowsky, J. a. Fleck, Jr., & M. D. Feit, Helmholtz beam propagation in rib waveguides and couplers by iterative Lanczos reduction, *Journal of the Optical Society of America A* **9**, 265 (1992).

[119] A. Yariv, *Quantum Electronics*, volume 0 of *Proceedings of the third international congress* (Wiley, 1989).

[120] W. S. C. Chang, *Fundamentals of Guided-Wave Optoelectronic Devices* (Cambridge University Press, 2009).

[121] H. M. Masoudi & S. J. Al-Bader, Three-dimensional modeling of etched groove separation of adjacent optical waveguides, *Microwave and Optical Technology Letters* **23**, 289–291 (1999).

[122] M. Duhring & O. Sigmund, Improving the acousto-optical interaction in a Mach-Zehnder interferometer, *Journal of Applied Physics* **105**, 083529 (2009).

[123] B. Bhushan, Springer Handbook of Nanotechnology xxxvi, 1222 p. (2004).

[124] T. H. P. Chang, *Combined microminiature processing and microscopy using a scanning electron probe system*, Ph.D. thesis, Cambridge University (1967).

[125] C. Vieu, Electron beam lithography: resolution limits and applications, *Applied Surface Science* **164**, 111–117 (2000).

[126] M. Schubert, *et al.*, Lambda shifted photonic crystal cavity laser, *Applied Physics Letters* **97**, 191109 (2010).

[127] G. Owen, Methods for proximity effect correction in electron lithography, *Journal of Vacuum Science & Technology B: Microelectronics and Nanometer Structures* **8**, 1889 (1990).

[128] K. D. Mackenzie, B. Reelfs, M. W. Devre, R. Westerman, & D. J. Johnson, Characterization & Optimization of Low Stress PECVD Silicon Nitride for Production GaAs Manufacturing (2004).

[129] M. Volatier, D. Duchesne, R. Morandotti, R. Arès, & V. Aimez, Extremely high aspect ratio GaAs and GaAs/AlGaAs nanowaveguides fabricated using chlorine ICP etching with N2-promoted passivation., *Nanotechnology* **21**, 134014 (2010).

[130] Soitec, www.soitec.com.

[131] C.-Y. Lin, *et al.*, Wideband group velocity independent coupling into slow light silicon photonic crystal waveguide, *Applied Physics Letters* **97**, 155–157 (2010).

[132] W. Bogaerts, P. Dumon, S. K. Selvaraja, D. Van Thourhout, & R. Baets, Silicon nanophotonic waveguide circuits and devices, *LEOS 2008 21st Annual Meeting of the IEEE Lasers and ElectroOptics Society* **1**, 304–305 (2008).

[133] M. van der Poel, *et al.*, Surface acoustic wave driven light modulation., *Proc. ECIO 07* 3–6 (2007).

[134] S. Petroni, *et al.*, GaN-based surface acoustic wave filters for wireless communications, *Superlattices and Microstructures* **36**, 825–831 (2004).

[135] E. C. S. Barretto & J. M. Hvam, Photonic integrated single-sideband modulator/frequency shifter based on surface acoustic waves, *SPIE Library* **7719**, 771920–771920–12 (2010).

[136] M. Izutsu, S. Shikama, & T. Sueta, Integrated optical SSB modulator/frequency shifter, *IEEE Journal of Quantum Electronics* **17**, 2225–2227 (1981).

[137] H. Murata, S. Yamamoto, & H. Sasai, Novel guided-wave electrooptic single-sideband modulator by using periodically domain-inverted structure in a long wavelength operation, *, 2003. OFC 2003* **1**, 9–10 (2004).

[138] H. Murata, M. Anjiki, & Y. Okamura, Optical Suppressed-Carrier Single Side-Band Modulator/Optical Frequency Shifter Utilizing Three-Branch Waveguide Interferometer and Polarization-Reversed Structure, *2006 European Microwave Conference* **0**, 609–611 (2006).

[139] K. Higuma, Y. Hashimoto, H. Nagata, & S. Oikawa, X-cut LiNbO3 optical SSB modulators, *Proc. CLEO/Pacific Rim* (2001).

[140] Sumitomo Osaka Cement Co., Ltd., www.socnb.com/product/hproduct_e/ln10.html.

[141] S. Kakio, *et al.*, Monolithically Integrated Tandem Waveguide-Type Acoustooptic Modulator Driven by Surface Acoustic Waves, *Japanese Journal of Applied Physics* **46**, 4608–4612 (2007).

[142] A. Dorrington & R. Kunnemeyer, Single sideband techniques for laser Doppler velocimeter frequency offset, *Optical Engineering* **42**, 3239 (2003).

[143] R. Zhou, Gang; Zhang, Xiupu; Yao, Jianping; Wu, Ke; Kashyap, A novel photonic frequency down-shifting technique for millimeter-wave-band radio-over-fiber systems, *IEEE Photonics Technology Letters* **17**, 1728–1730 (2005).

[144] T. Kuri, H. Toda, & K. Kitayama, Photonic downconversion with optical frequency shift for dense WDM radio-on-fiber signals, in *Lasers and Electro-Optics Society, 2002. LEOS 2002. The 15th Annual Meeting of the IEEE*, volume 2, 473–474 (IEEE, 2003).

[145] F. V. Kowalski, P. D. Hale, & S. J. Shattil, Broadband continuous-wave laser., *Optics letters* **13**, 622 (1988).

[146] T. Tanabe, M. Notomi, & E. Kuramochi, Measurement of ultra-high-Q photonic crystal nanocavity using single-sideband frequency modulator, *Electronics Letters* **43** (2007).

[147] U. Gliese, S. Norskov, & T. Nielsen, Chromatic dispersion in fiber-optic microwave and millimeter-wave links, *IEEE Trans. Microw. Theory. Tech.* **44**, 1716–1724 (1996).

[148] R. Hofstetter, H. Schmuck, & R. Heidemann, Dispersion effects in optical millimeter-wave systems using self-heterodyne method for transport and generation, *IEEE Trans. Microw. Theory Tech.* **43**, 2263–2269 (1995).

[149] E. Vourch, B. Della, D. L. Berre, & D. Herve, Millimeterwave power-fading compensation for wdm fiber-radio transmission using a wavelength-self-tunable single-sideband filter, *IEEE Trans. Microw. Theory Tech.* **50**, 3009–3015 (2002).

[150] G. Smith & D. Novak, Technique for optical SSB generation to overcome dispersion penalties in fibre-radio systems, *Electronics letters* **33**, 74–75 (2002).

[151] S. Zheng & X. Zhang, Simultaneous realization of optical carrier-suppression and SSB modulation in wireless fiber links using fiber Bragg grating, *Microwave and Optical Technology Letters* **46**, 336–339 (2005).

[152] K. Kitayama, T. Kuri, K. Onohara, T. Kamisaka, & K. Murashima, Dispersion effects of FBG filter and optical SSB filtering in DWDM

millimeter-wave fiber-radio systems, *Journal of Lightwave Technology* **20**, 1397–1407 (2002).

[153] J. Capmany, *et al.*, Multiwavelength Single Sideband Modulation for WDM Radio-Over-Fiber Systems Using a Fiber Grating Array Tandem Device, *Technology* **17**, 471–473 (2005).

[154] T. Kuri, K.-i. Kitayama, & Y. Ogawa, Fiber-Optic Millimeter-Wave Uplink System Incorporating Remotely Fed 60-GHz-Band, *October* **47**, 1332–1337 (1999).

[155] T. Eiju, Microscopic laser Doppler velocimeter for blood velocity measurement, *Optical Engineering* **32**, 15 (1993).

[156] A. Priezzhev & Y. M. Romanovskii, Laser Doppler spectroscopy and its applications in biology, *Soviet Journal of Quantum Electronics* **8**, 1260–1263 (1978).

[157] E. Bonnotte, *et al.*, Guided-wave acoustooptic interaction with phase modulation in a ZnO thin-film transducer on an Si-based integrated Mach-Zehnder interferometer, *Journal of Lightwave Technology* **17**, 35–42 (1999).

[158] S. Tao, *et al.*, Cascade wide-angle Y-junction 1 x 16 optical power splitter based on silicon wire waveguides on silicon-on-insulator, *Optics Express* **16**, 21456–21461 (2008).

[159] L. Soldano & E. Pennings, Optical multi-mode interference devices based on self-imaging: principles and applications, *Journal of Lightwave Technology* **13**, 615–627 (1995).

[160] Z. Wang, Z. Fan, J. Xia, S. Chen, & J. Yu, 1 x 8 Cascaded Multimode Interference Splitter in Silicon-On-Insulator, *Japanese Journal of Applied Physics* **43**, 5085–5087 (2004).